Electromechanical Polysilicon Structures and Micromachining Processes for Sensor and Actuator Applications

Dissertation submitted to the
Faculty of Sciences of the University of Neuchâtel
to obtain the degree of Doctor of Science

by
Christian Linder
Dipl. Phys. ETH

Institute of Microtechnology
University of Neuchâtel
Breguet 2, 2000 Neuchâtel
Switzerland

1993

Printed by Baillod SA
2017 Boudry
Switzerland

für meine Eltern

IMPRIMATUR POUR LA THÈSE

Electromechanical Polysilicon Structures and Micromachining Processes for Sensor and Actuator Applications

de Monsieur Christian Linder

UNIVERSITÉ DE NEUCHÂTEL

FACULTÉ DES SCIENCES

La Faculté des sciences de l'Université de Neuchâtel
sur le rapport des membres du jury,
MM. les professeurs N. de Rooij, A. Shah,
H. Baltès (EPF-Zurich) et W. Trimmer
(Princeton).
autorise l'impression de la présente thèse.

Neuchâtel, le 25 mai 1993

Le doyen:

A. Robert

Contents

Summary IV

1 Introduction 1

1.1 Silicon Technology for Microelectronics and Microtransducers 1

1.1.1 IC Technology 1
1.1.2 Polysilicon Compared with Monocrystalline Silicon in View of Transducer Applications 3
1.1.3 Bulk and Surface Micromachining Illustrated by Transducer Devices 6

1.2 Background of the Work and Outline of the Thesis 12

2 Surface Micromachining Techniques 15

2.1 Introduction 15

2.2 Sacrificial Layer Technology 15

2.2.1 Free-standing Polysilicon Structures – Basic Processing Description 15
2.2.2 Polysilicon Deposition and Doping Parameters 21
2.2.3 Sticking Problem 25
2.2.4 Surface Encapsulation 28

2.3 Silicon Dry Etching by Plasma for Use in Micromachining 30

2.3.1 (Poly-)Silicon Etching Parameters 30
2.3.2 Further Device Examples Based on Dry Etching 37

2.4 Combination of Bulk and Surface Processing 40

2.5 Conclusion 44

3 Electromechanical Polysilicon Actuators 45

3.1 Introduction 45

3.2 Fabrication and Operational Principles 47

3.3 Theoretical and Experimental Device Performance 52

3.3.1 Bridge Actuator 52
3.3.2 Comb Actuator 57

3.4 Applications 64

3.4.1 Electromechanical Microswitch 64
3.4.2 XY Microstage 65
3.4.3 Optical Microshutter 66

3.5 Conclusion 68

4 Polysilicon Resonators with Integrated Excitation and Detection 69

4.1 Introduction 69

4.2 Short Theory on Vibrations of Beams 70

4.2.1 Resonance Frequency 70
4.2.2 Effect of Axial Force on Frequency 71

4.3 Performance of Electrostatically Excited and Detected Beam Resonators 72

4.3.1 Resonator Structure and Detection Circuit 72
4.3.2 Experimental Frequency Response 76

4.4 Other Resonator Types 80

4.5 Resonant Flow Velocity Sensor – Design Considerations 80

4.6 Conclusion 84

5 Conclusion 85

References 87

Acknowledgements 100

Biography 103

Publications 104

Summary

Silicon micromachining has become a fundamental tool for the realization of micromechanical devices and, in particular, miniature sensors and actuators. While bulk micromachining, which means the construction of micromechanical structures out of the monocrystalline silicon wafer, is a well-established technology nowadays, recently a lot of interest has focused on surface-micromachined devices, i.e. three-dimensional microstructures which are located on the wafer surface and consist most often of thin films. This work reports the development of novel (surface) micromachining techniques and demonstrates prototypes of sensors and actuators whose fabrication is based on these techniques. It is shown that, in particular, free-standing polysilicon structures exhibit promising features for application as IC compatible transducers.

The sacrificial layer technology for the fabrication of free-standing thin-film structures (e.g. polysilicon) by lateral etching of an underlying sacrificial layer (e.g. silicon dioxide) is discussed. In particular, LPCVD (610 °C, 200 mTorr), doping (diffusion) and annealing (1050 °C, 30 min) parameters have been adjusted for optimum (electro)mechanical properties of the polysilicon. Typical beams measure: 200 – 600 µm in length, 0.5 – 50 µm in width and 1 – 2 µm in thickness. Methods such as capacitive a.c. activation during operation for avoiding sticking of the free-standing structures on the substrate are described. Furthermore, by applying two sacrificial-layer processing steps, free-standing polysilicon beams have been micro-encapsulated on the substrate surface by using polysilicon caps.

Novel highly reproducible dry etching techniques are reported as promising micromachining tools. For instance, employing a SF_6/O_2 plasma, thin-film structures like aluminum beams have been released by undercutting the silicon substrate. Dry etching by plasma in C_2ClF_5/SF_6 gases has been successfully applied for defining submicron-wide high-aspect ratio polysilicon beams.

For a growing number of applications, the combination of surface and bulk micromachining turns out to be an essential processing step; device examples such as polysilicon microbridges on silicon membranes or overhanging silicon cantilevers with square cross section and integrated tips are presented.

Using sacrificial layer technology, two types of electrostatic polysilicon microactuators have been fabricated: a bridge structure using the deflection perpendicular to the substrate and a suspended comb structure allowing displacements parallel to the substrate surface. A key feature of these surface-micromachined actuators is the low driving voltage which enables the combination with IC components in microsystems. For instance, a 300 µm long microbridge can be downward deflected to the substrate by applying 11 V, and a 5.9 µm displacement is observed for applying 20 V to a comb actuator. Optimum design parameters for such low-drive structures are obtained by analytical modeling. In particular, the potential energy curve provides valuable information on the stability conditions of the electromechanical structures and on the onset of sticking of the movable to the fixed electrode of the actuator. Measurements on prototype devices agree well with the simple modeling and, moreover, yield experimental design rules. Several applications are described: an IC-compatible electromechanical microbridge-relay; an *xy* microstage driven by four comb actuators for micro- and nano-positioning; a comb-driven microshutter for simple control of a 6 µm wide laser beam.

In the field of sensors, polysilicon microbeams are investigated for use as resonators. Resonant devices are an attractive class of sensors which enable accurate measurements; for instance, the resonance frequency is highly sensitive to a large variety of parameters. A simple model for the estimation of the resonance frequency is given; especially, the effect of axial forces on the vibrations of beams is described. Axial forces are produced in polysilicon resonant beams which are placed on top of silicon membranes for deflection detection. In this way, highly sensitive differential pressure sensors for appliaction in flow measurement can be realized.

Two types of polysilicon resonators with integrated components for excitation and detection have been fabricated by sacrificial layer technology: one oscillator is electro-thermally activated and detected by means of piezoresistors, the other one is electrostatically (capacitively) excited and sensed. The latter resonator device is investigated in detail. Since the capacitance changes for the vibrating microbeam are extremly small (in the fF range), the oscillating polysilicon structure is integrated with a fixed polysilicon capacitor in a capacitive voltage divider whose output signal drives a NMOS inverter. Thus, frequency response measurements yield a.c. output signals in the range of mV. From gain/phase measurements a resonance peak at about 120 kHz results for a 300 µm long, 25 µm wide and 1 µm thick polysilicon microbridge – using the simple theory, the first resonance frequency is calculated to be about 100 kHz.

1 Introduction

1.1 Silicon Technology for Microelectronics and Microtransducers

Over the past three decades, rapid and substantial development in microelectronics has had a significant influence on the world. For instance, microprocessors, memories and advanced integrated circuits (ICs) are main components of instrumentation systems which find applications in various domains such as automotive systems, industrial manufacturing, medicine, environmental monitoring and control, telecommunications and consumer products.

In addition to the signal-processing unit, these instrumentation systems require two further key components, namely input and output transducers, also called sensors and actuators [e.g. 1,2]. Sensors provide the microprocessor with information on the variables of the surrounding world (such as pressure, temperature or humidity), by converting the variables into electrical signals. Actuators enable the microprocessor to communicate with the non-electronic environment and to control the variables of the latter; examples are an electrically actuated overpressure valve or a relay for turning on and off a heater.

1.1.1 IC Technology

The microelectronic revolution has been largely based on the enormous progress of silicon microtechnology (also called IC technology) whose main features are briefly summarized in this paragraph [e.g. 3,4]. First, the electrical resistivity of the semiconductor silicon can be varied many orders of magnitude by controlled incorporation of dopants using diffusion or ion implantation. Thus, conductors and resistors can be created in the form of doped regions at the wafer surface.

By simply introducing oxygen in a high temperature furnace, thermal oxide can be grown on exposed silicon surfaces. Such thermal silicon dioxide layers exhibit excellent insulation and passivation properties which are difficult to achieve by dielectric films on other semiconductor substrates.

This chapter includes parts of the publications: [70] and [57].

Using thin film technology, different other films can be deposited, e.g. polycrystalline silicon (polysilicon) and dielectric layers (silicon dioxide or silicon nitride) by low-pressure chemical vapor deposition (LPCVD), or metal films (e.g. aluminum) by sputtering. Metal and polysilicon films serve as conductive materials for interconnections, and as gate electrode or electrical contact materials. Dielectric films are used for insulation between conducting layers, for passivation and protection of devices from impurities or moisture, and as masks for doping.

The lithographic process transfers the patterns from a (chrome) mask to a resist layer that covers the wafer. Subsequent dry or wet etching is used to remove the unwanted film or substrate parts which are not protected by the resist pattern. Lithography and etching allows microscale features to be defined and, in addition, with the same accuracy to align patterns of different films to each other.

Nowadays, IC technology has become a well-established and powerful tool for the fabrication of microelectronic components such as the polysilicon-gate field-effect transistor (FET) shown in Fig. 1.1. The major advantages of microelectronics can be summarized as follows:

- batch processing, i.e. mass production at low cost
- excellent reproducibility
- high reliability
- high performance
- microscale geometries
- low power consumption

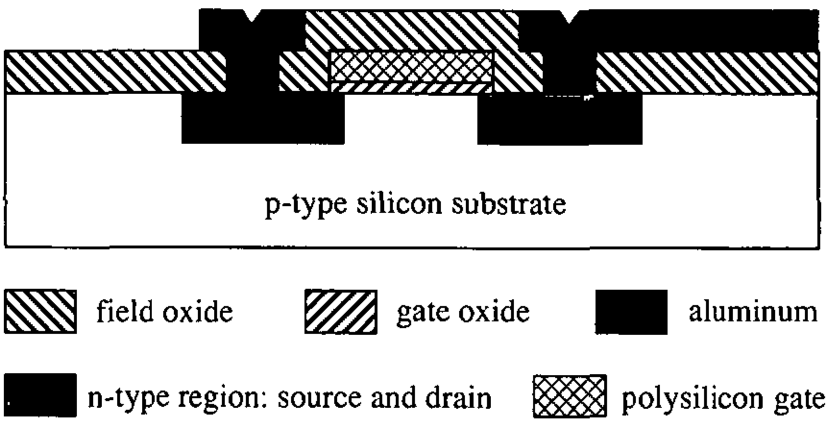

Fig. 1.1 Cross section of a n-channel enhancement polysilicon-gate FET.

1.1.2 Polysilicon Compared with Monocrystalline Silicon in View of Transducer Applications

Highly expensive research efforts have been invested by the electronics industry over the past thirty years to understand, control and commercialize the electronic performance of silicon. These enormous research activities have also simultaneously revealed the excellent mechanical performance of silicon. For instance, the modulus of elasticity of silicon is as high as that of steel, the tensile yield strength is stronger then that of steel, the hardness is the same as for quartz, and the density is low, near that of aluminum. A particular attribute of the semiconductor silicon is the piezoresistive effect, i.e. its high sensitivity to stress [5]: when silicon is strained, a large change in its electrical resistivity results, larger by about two orders of magnitude than the corresponding change in metals used previously for strain gauge applications. Furthermore, silicon is also sensitive to many other physical variables such as light, magnetic fields and temperature. Considering all these outstanding properties, silicon is a very promising material for sensors and actuators [e.g. 6]. Especially the combination of electrical and mechanical characteristics of silicon is widely exploited in microelectromechanical devices [e.g. 7].

The above listed attributes are valid for monocrystalline as well as for polycrystalline silicon. The crystal grains of which polysilicon is composed have different shape and crystallographic orientation, and are separated by the grain boundaries. The latter comprise the major difference between monocrystalline and polycrystalline silicon and influence the physical properties in different degrees as described in the following.

The mechanical properties of monocrystalline silicon depend strongly on the crystal-orientation; as an example, the moduli of elasticity of silicon are 130, 169 and 187 GPa for the [100], [110] and [111] direction, respectively [8]. For polysilicon, these mechanical properties can be estimated by averaging over the grain orientations present. For instance, values of the **modulus of elasticity** between 150 and 170 GPa have been calculated for polysilicon [9,10,11]; measurements yielded values of 90 GPa [12,13], 140 GPa [14], 175 GPa [10,15] and 190 GPa [16]. A problem in the experimental determination of the modulus of elasticity is the indirect way for its estimation, e.g. by measuring the deflection or the resonance frequency of test structures. First, errors due to the approximation in the analytical model are introduced; in addition, such measurements depend strongly on the geometrical dimensions, i.e even small errors in the dimensions can significantly change the results.

In view of deformation, flexure and fracture, the grain boundaries of polysilicon can block the propagation of dislocations between adjacent crystal grains and thus make polysilicon behave as an almost ideal brittle material

[17]. Consequently, polysilicon tends to be linearly elastic until it fractures. Moreover, experiments have shown that the maximum flexure of polysilicon structures is larger than that of identical monocrystalline silicon structures [18]. A further special feature of polysilicon is that no material fatigue has been observed so far; endurance tests of continued flexure (10^9 cycles at resonance frequency) or large displacements of polysilicon beams did not result in any noticeable change of the operational characteristics [18].

The grain structure of polysilicon considerably impedes the heat flow and thus the thermal conductivity in polysilicon. While monocrystalline silicon has a good thermal conductivity of about 1.5 $Wcm^{-1}K^{-1}$ [19], values of about 0.3 $Wcm^{-1}K^{-1}$ have been measured for polysilicon [20].

The electrical properties of polysilicon are also affected by the grain boundaries. They can be described by the carrier-trapping model originally proposed by Kamins [21] and quantitatively described by Seto [22]. The model assumes that the grain boundaries (whose thickness is negligible compared to the grain size) contain a large number of trapping states resulting from incomplete atomic bonding due to the disorderded atoms at the grain boundaries. The model further assumes that the doping atoms are totally ionized and uniformly distributed in the polysilicon. The trapping states will then trap free charge carriers and immobilize them, reducing thereby the number of free carriers available for electrical conduction. After trapping of carriers, the initially neutral traps become electrically charged. As a consequence, for neutrality reasons, depletion regions are created in the adjacent crystal grains. This results in the formation of potential energy barriers at the grain boundaries which impede the motion of carriers from one crystallite to another, thereby reducing their mobility. Thus, for the same amount of doping, mobility and carrier concentration of polysilicon are smaller than those of monocrystalline silicon. However, at high dopant concentrations, the grain boundaries no longer limit the conduction. Figure 1.2 shows an illustration of the carrier-trapping model as described by Seto [22]. As indicated in Fig. 1.3 (a) and (b), the measured resistivity of polysilicon as well as its temperature coefficient agree well with the predictions of the carrier-trapping model [e.g. 23].

In monocrystalline silicon, the piezoresistive effect depends on the orientations of the stress and of the current flow relative to the principal crystallographic axes. The piezoresistance matrix (π) relates the relative change of resistivity ($\Delta\rho/\rho$) linearly to the stress matrix (σ). For most applications, it is advantageous to divide the stress in a longitudinal stress component σ_l which acts in the same direction as the current and a transverse stress component σ_t which is transverse to the current flow. Thus, the resistivity change due to a given stress can be written as:

$$\Delta\rho/\rho = \pi_l \cdot \sigma_l + \pi_t \cdot \sigma_t = \pi_l \cdot E_l \cdot \varepsilon_l + \pi_t \cdot E_t \cdot \varepsilon_t = K_l \cdot \varepsilon_l + K_t \cdot \varepsilon_t .$$

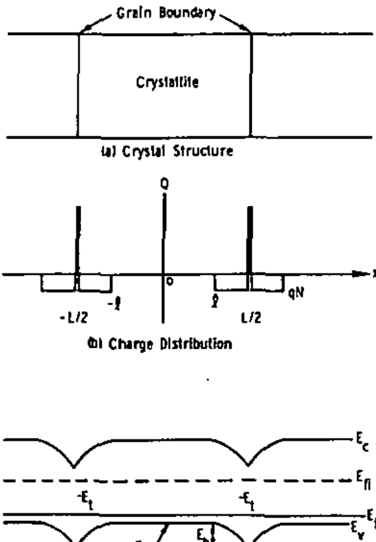

Fig. 1.2 (a) Model for the crystal structrure of polysilicon films; (b) the charge distribution within the crystallite and at the grain boundary; (c) the energy band structure tor polysilicon crystallites [22].

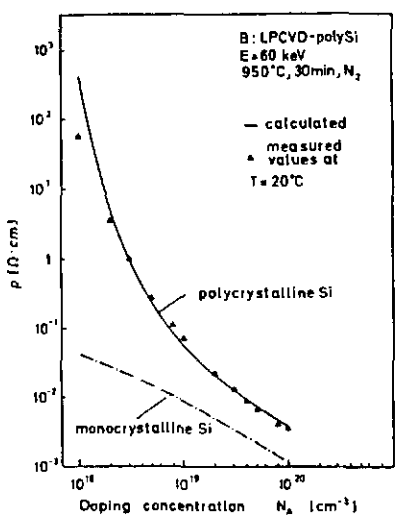

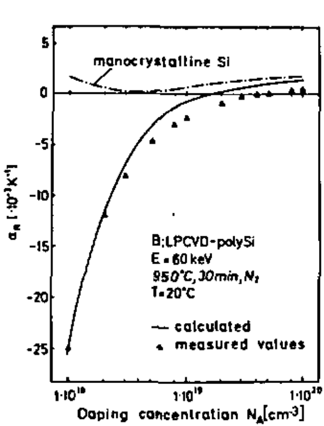

Fig. 1.3 Resistivity (a) and temperature coefficient of resistance (b) for boron-doped polysilicon as a function of doping concentration [23].

The relationship between the second and the third expression in the above equation is given by the Hooke's law where $\varepsilon_{l,t}$ denote the corresponding strain components and $E_{l,t}$ are the moduli of elasticity. The fourth expression of the equation defines the longitudinal and the transverse gauge factor, K_l and K_t, respectively. As an example, the piezoresistors in monocrystalline silicon are usually oriented in the <110> direction; in this case, K_l and K_t for lightly doped p-type silicon are 121.3 and -112.1, respectively; K_l and K_t for lightly doped n-type silicon are -52.7 and 29.7, respectively [24,25].

The piezoresistive properties of polysilicon are determined by the crystal grains as well as by the grain boundaries; it is a rather difficult task to estimate values for polysilicon by means of the known data of monocrystalline silicon. Several models have been developed which have mainly two features in common [e.g. 23, 26-29]. First, some averaging of the piezoresistance matrix of monocrystalline silicon is performed to relate the orientation-dependent bulk silicon data to the polysilicon stucture with its (dominant) grain orientations. Second, in order to take the effect of the grain boundaries into account, a factor ρ_{mono}/ρ_{poly} is introduced for lowering the magnitude of the gauge factors. Measured and calculated data of longitudinal and transverse gauge factors of doped polysilicon are plotted as a function of the dopant concentration in Figs. 1.4 [29] and 1.5 [28]. The graph of Fig. 1.4 shows maximum values of about 40 for K_l, whereas the K_t-values of about -10 are relatively small. The graph also indicates that the processing parameters inluence the gauge factors. Figure 1.5 indicates that boron-doped polysilicon has higher gauge factors than phosphorus-doped polysilicon as it is the case for monocrystalline silicon; hence p-type resistors are preferred when using piezoresistivity for signal detection.

1.1.3 Bulk and Surface Micromachining Illustrated by Transducer Devices

Since highly sophisticated IC components for microprocessors and microcomputers are available today, a major issue for further improvement of instrumentation systems is to lower the cost and to maintain or increase the perfomance of the (traditional) input and output tranducers. For this reason, in addition to the investigation of silicon as a basic material for transducers as described in 1.1.2, thin-film and IC technology has been applied and extended for the (batch) fabrication of microscale sensors and actuators. In particular, silicon micromachining has been developed as a powerful tool for the fabrication of micromechanical devices and, in general, miniature transducers. Micromachining techniques include firstly the basic processing steps of IC technology, namely film formation, doping, lithography and etching. In addition, they incorporate special etching and

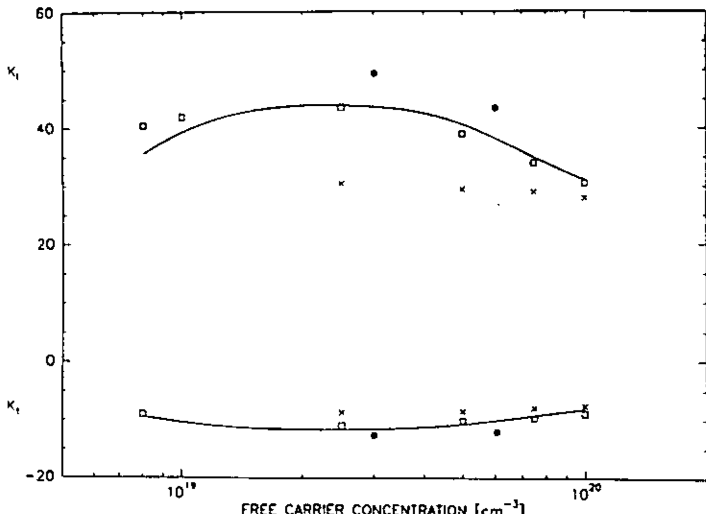

Fig. 1.4 The longitudinal (K_l) and transverse (K_t) gauge factors as a function of the doping concentration; experimental results after: □, classic thermal annealing; x, RTA; •, c.w. argon laser annealing; solid lines correspond to the theory [29].

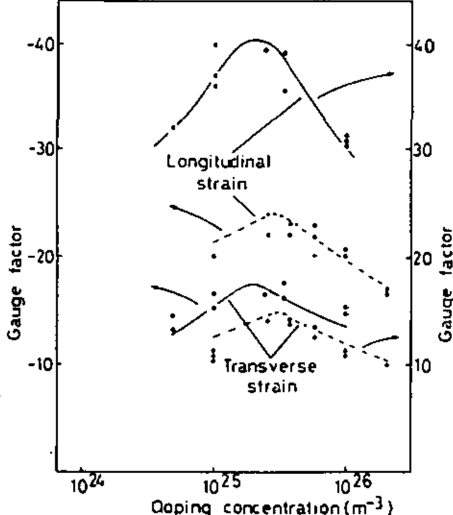

Fig. 1.5 Longitudinal and transverse gauge factors versus doping concentration for boron and phosphorus doped material; theoretical predictions (boron —— and phosphorus – – –) are compared to experimental points (boron • and phosphorus +) [28].

bonding processes which allow for the sculpturing and the packaging of three-dimensional microstructures. In the following, the use of micromachining tools is illustrated on typical sensor devices. Historically, most actuator applications of micromachined structures such as electromechanical switches,valves or *xy* translators were developed after the first sensor devices. For this reason, micromachining techniques are often introduced with the help of sensor examples.

The measurement of temperature can be performed by applying the variation in the electrical resistance with temperature. This principle has been for employed for almost a hundred years. Temperature sensors using different types of Platimum Resistance Thermometers (PRTs) are the most accurate devices available and can be employed over the large range between 15 and 1500 K [30,31]. However, the traditional PRT containing a high purity thin platimum wire having a diameter of a about 50 μm is rather expensive. With the adoption of microtechnology, high quality and low cost temperature sensors based on platinum thin films can be realized [e.g. 32]. Polysilicon resistors have also been applied as thermometers measuring from -40 to 140 °C [e.g. 33]. A particular advantage of such polysilicon resistors is their full compatibility with IC components, although their temperature range is much smaller than that of PRTs, i.e. it is limited the extrinsic region of the doped polysilicon. Finally, the well-defined temperature dependence of the forward characteristics of silicon diodes can also be used for accurate temperature measurement. Similar as for the polysilicon resistors, the temperature range is limited to the extrinsic region of the *pn* junction. A favorable configuration consists of two bipolar transistors with a constant ratio of the emitter current densities [34,35]. In this configuration, the difference in the base-emitter voltages is proportional to the absolute temperature. Thus, it is possible to directly employ IC components as temperature sensors.

As second example, a pressure sensor is considered which utilizes the pressure-induced deflection of a membrane. The stress due to the membrane deflection and hence the pressure can be detected by means of piezoresistors. Because of the excellent electrical and mechanical properties of silicon, a silicon membrane with implanted piezoresistors forms the foundation of a promising pressure sensor [e.g. 36-39]. The membranes are realized by so-called **bulk micromachining**, i.e. by fabrication out of the monocrystalline silicon wafer. They can be formed, for instance, by backside etching of the silicon substrate using crystal-orientation-dependent etchants such as KOH or EDP [e.g. 40] together with etch-stop techniques for exact control fo the membrane thickness [e.g. 41]. Bonding the silicon membrane structures on a Pyrex glass plate [e.g. 42] produces reference microcavities which can be applied for the measurement of absolute pressure. On the other hand, by adding a metal film on the pyrex glass substrate, the membrane

deflection due to the pressure can also be monitored capacitively, i.e. by measuring the capacitance change between the membrane as movable electrode and the metal film on the glass substrate which serves as a fixed counter electrode [43-46].

Combining several simple fabrication and detection methods allows more complex parameters like gas or liquid flow to be measured [e.g. 47]. For instance, the hot-wire or heat-transfer principle can be applied to the measurement of flow by detection of the power dissipation of a heater when a constant temperature difference between the heated element and a passing flow is maintained. A large variety of flow sensors based on the hot-wire priniple has been realized in silicon technology [48-56]. A schematic cross section of a recently published device is shown in Fig. 1.6 [57]. Boron-doped regions which are placed on a silicon membrane serve as heating resistors; the membrane provides thermal isolation to the rim of the chip. The difference between the heater and the ambient temperature is measured by bipolar transistors which are located on the membrane and on the rim of the chip. When the sensor chip is placed in a fluid, the power dissipation, which is proportional to the temperature difference, is given by the conductive heat flow into the membrane and the fluid as well as by the convective heat flow into the fluid. The latter depends on the square root of the fluid velocity, i.e. the flow is proportional to the square of the convective heat loss. The liquid velocity sensor sketched in Fig. 1.6 has been fabricated by using a fully bipolar-compatible industrial process including bulk micromachining; its special features are a high sensitivity and a large flow range.

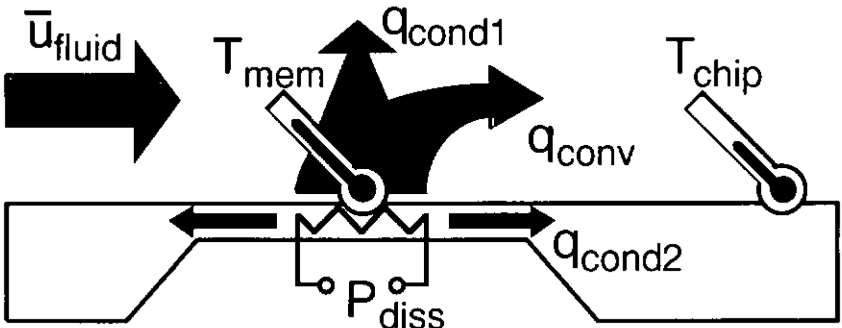

Fig. 1.6 Cross section of a liquid flow sensing chip based on the hot-wire principle [57].

A further method for the measurement of flow is based on the differential pressure principle. In the field of traditional flow sensors, the differential pressure method has been widely used because of its high reliability and repeatability [58]. The flow velocity is proportional to the square root of the pressure drop (differential pressure) across an orifice in the flow channel. This square root relationship has limited the accuracy and the operating range of traditional differential-pressure flow sensors. Recently, examples of pressure-drop-based flowmeters fabricated in silicon technology have been reported [59,60]. Using a very thin capacitive membrane and a long piezoresistive cantilever, they overcome the drawback of moderate accuarcy and show a high resolution thus allowing extremely small flows to be measured. Furthermore, these devices do not require heating of the fluid which is necessary for hot-wire type flow sensors, and which may be problematic in several applications such as the medical domain.

Resonator devices are highly sensitive to various parameters such as temperature, force or viscosity [61,62]. For instance, resonant beams depend strongly on axial forces. Thus, by using resonant microbeams on membranes, high-resolution pressure-based flowmeters can be achieved [63-65] which, in addition, cover a large flow range. Figure 1.7 shows a schematic view of such a device. A particular component of this transducer is the micromechanical polysilicon beam. Such free-standing thin-film structures located on the wafer surface are fabricated by means of so-called **surface micromachining** [66-70]. A further special feature of the transducer sketched in Fig. 1.7 is the combination of bulk (for the membrane) and surface (for the beam) micromachining in its fabrication.

The dimensions of devices fabricated by surface micromachining are generally one or two orders of magnitude smaller than those fabricated by bulk processing. Thus, on the one hand, miniaturization can be considerably increased using surface microstructures. A probable drawback are the small masses which may be insufficient for mechanical transfer. One special advantage of surface-micromachined devices is their easy integration with IC components, since the wafer surface is also the working area of IC elements.

Bulk micromachining is under development for more than twenty years and has become a well-established technology [e.g. 71]. Nowadays, a number of firms successfully manufacture and market silicon transducers based on bulk processing. Over the last ten years, surface micromachining has been intensively investigated by a great number of R&D laboratories. Most devices are still on a prototype level, however, mainly due to the IC compatibility, powerful industries such as Honeywell [64], Analog Devices [72] and Motorola [73], focus efforts on the development of surface micromachining and, in particular, on electromechanical polysilicon devices for sensor and actuator applications as shown in Fig. 1.8.

f(F(p))

F F

p

CVD Si-dioxide & LPCVD Si-nitride

n-type region

p-type region

P-doped LPCVD poly-Si

aluminum

Fig. 1.7 Schematic cross section of a polysilicon beam resonator with electrostatic (capacitive) excitation and detection on a silicon membrane for (differential) pressure measurement.

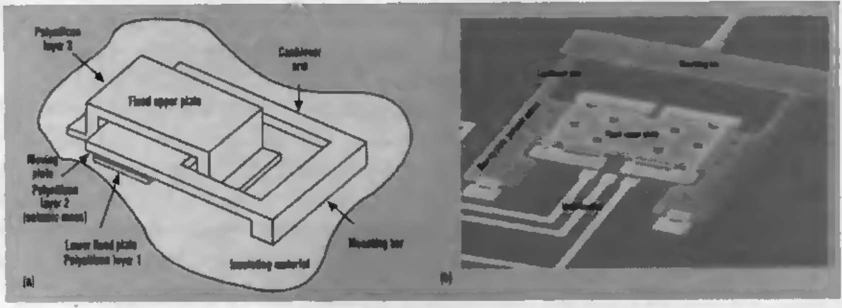

Fig. 1.8 Schematic view (a) and fabricated prototype (b) of a surface-micromachined polysilicon accelerometer made by Motorola Semiconductor, Phoenix, Ariz. [74].

1.2 Background of the Work and Outline of the Thesis

In 1986, the author started work at the IMT with a small industrial project: an evaluation of silicon-based microsensors, with special attention to the measurement of flow. At that time, silicon bulk micromachining was a well-known tool at the IMT, and several projects dealt with that technology [25,39,75]. However, as mentioned in 1.1.3, surface micromachining was receiving attention from many research laboratories at that time. The IMT was also interested in developing a fabrication process for three-dimensional polysilicon structures, and to compare as well as to combine bulk and surface micromachining techniques. The author started the polysilicon technology at the IMT as a one-man project which was an extension of the evaluation project with a polysilicon resonator-based flow sensor as an intended novel application. In the first phase, a large number of technological problems had to be solved: the development and the optimization of the parameters for the LPCVD, the annealing and the doping of good-quality polysilicon films (1987/88), system installation and process development of dry etching techniques for polysilicon and related materials (1989/90). Simultaneously, a great deal of information on other surface micromachining techniques was elaborated. Thus, the fabrication tools of the IMT laboratory were extended by powerful novel processing techniques which are described in Chapter 2 of this thesis: the basic polysilicon technology, other methods of micromachining such as dry etching, and combinations of surface and bulk processing.

Once the feasibility for the fabrication of free-standing polysilicon structures was shown, and first prototype devices exhibited promising characteristics, new projects were defined for various applications of micromechanical polysilicon structures. For efficient progress of these new applications, the author has been involved in leading the projects and introducing new coworkers to the field of surface micromachining. One new project has dealt with the realization and characterization of horizontal-motion actuators. The latter as well as vertical-motion actuators (based on the polysilicon prototype microbeam of Fig. 1.7) are described in Chapter 3 of the thesis. In particular, modeling of these electromechanical polysilicon structures has been performed in order to understand the behavior of the devices and to find an optimum design for actuators having high reliability and low driving voltages. Chapter 3 ends with novel prototype devices which illustrate the oncoming importance of microactuators in various domains.

The investigation of actuators is also of importance for resonators since the latter need actuator elements for excitation. Resonant polysilicon sensors, which offer the possibility for integration of excitation and detection

components, are discussed in Chapter 4. A short introduction to the theory of mechanical resonators is followed by a detailed experimental analysis of a capacitively (electrostatically) excited and detected polysilicon beam resonator (as shown in Fig. 1.7). Furthermore, resonators with other methods of excitation (e.g. thermal) and detection (e.g. piezoresistive), and design improvements (e.g. shielding) are presented. Finally, a novel resonant polysilicon flow sensor is proposed whose key features are: fluid velocity measurement based on the well-established differential pressure principle, and a high sensitivity by applying resonators for the detection of the membrane deflection. As for the actuators, new projects have been started to extend the activities of the IMT in the area of resonant sensors.

In the conclusion Chapter 5, the results of design, fabrication and characterization of the polysilicon prototype sensors and actuators are summarized and discussed in view of possible industrial applications. Furthermore, future trends of R&D in (surface-)micromachined devices and the importance of the latter in microsystems are outlined.

2 Surface Micromachining Techniques

2.1 Introduction

The primary issue for the successful construction of microstructures having useful characteristics for transducer applications is a reliable and reproducible technology. Therefore, extensive work has been invested in the development of novel surface micromachining tools. The results, basic processing steps as well as special technological details are described in this chapter. First, the sacrificial layer technology for the fabrication of free-standing polysilicon microstructures is discussed; in particular, the process parameters for polysilicon are optimized in order to avoid buckling and sticking phenomena, and to obtain suitable electromechanical properties. Surface encapsulation of free-standing microstructures as special extension of the sacrificial layer technology is presented. A further section deals with silicon dry etching by plasma for use in micromchining. Finally, the combination of surface and bulk processes is illustrated on typical examples.

2.2 Sacrificial Layer Technology

2.2.1 Free-standing Polysilicon Structures – Basic Processing Description

As mentioned in the previous chapter, polysilicon is advantageous for the realization of micromechanical structures in an IC-compatible fabrication process. Thus, surface micromachining for the construction of three-dimensional microstructures using polysilicon films has become an important alternative to the well-established bulk micromachining of single crystal silicon wafers. In particular, free-standing polysilicon beams can be realized by the sacrificial layer technology whose key processing steps are (Fig. 2.1): deposition and patterning of a sacrificial silicon dioxide layer on the substrate; deposition and definition of a polysilicon film; removal of the sacrificial oxide by lateral etching in hydrofluoric acid, i.e. completely

Parts of this chapter are published in: [70], [85], [86], [104], [105], [121] and [122].

underetching the polysilicon pattern where it covers the oxide.

Since both polysilicon and silicon dioxide are standard materials for IC devices, a great variety of micromechanical structures based on the sacrificial layer technology uses this material combination: Muller and Howe have realized several types of sensors and actuators using polysilicon microstructures [76,77,69,14]; Guckel et al. have fabricated vacuum-sealed microcavities at the substrate surface for application as pressure transducers [67,78,79]; the micromechanical structures of Mehregany, Gabriel and Trimmer use relatively thick polysilicon films [68]; Parameswaran and Baltes et al. combine a CMOS process with a post-processing sacrificial layer etching step [80.1]; Mokwa et al. construct CMOS-compatible polysilicon membranes for pressure measurement [80.2].

Different material combinations for free-standing/sacrificial layers have also been adopted: an all-metal combination by Nathanson et al. [81]; a silicon dioxide/polysilicon combination by Hälg [82]; a silicon nitride/ polysilicon combination by Sugiyama et al. [83]; a silicon nitride/aluminum combination by Scheeper et al. [84].

Two different methods have been applied at the IMT for the fabrication of micromechanical polysilicon beams. One approach uses a CVD silicon dioxide as sacrificial layer [76,85,86]. The polysilicon covers then the patterned oxide so that the finally underetched beams are raised by steps above the substrate (Fig. 2.1 a)). The process starts with LPCVD of a silicon nitride layer (typical thickness between 0.15 and 0.3 μm) for protection of the substrate. Next, undoped or phosphorus-doped (about 4 wt.%) silicon dioxide is deposited by low-temperature (400 °C) atmospheric pressure CVD (Vapox). Photolithography and wet etching in buffered hydrofluoric acid (BHF) defines the sacrificial oxide regions for the free-standing structures. Subsequently undoped polysilicon is deposited by LPCVD at 610 °C and 200 mTorr. For the doped beams, an additional phosphorus-doped (P-doped) Vapox layer is deposited on the polysilicon film. Then the polysilicon is annealed at 1050 °C in order to improve its material properties, e.g. to lower the intrinsic mechanical stress. At the same time, for the doped oxides, the phosphorus atoms diffuse from the upper as well as from the lower (sacrificial) P-doped Vapox into the polysilicon. In the next step, the polysilicon beam patterns are defined by photolithography and wet or dry etching. The final lateral etching of the sacrificial silicon dioxide is done in freshly prepared hydrofluoric acid (HF). SEMs of free-standing polysilicon test structures are shown in Figs. 2.2 – 2.5.

The second procedure for beam fabrication is based on the localized oxidation of silicon (LOCOS) process where windows are opened in a silicon nitride on the silicon substrate and subsequently, a thermal silicon dioxide is grown in the openings [79,70]. Taking this patterned thermal oxide as sacrificial layer, allows for the construction of planar polysilicon beams, i.e.

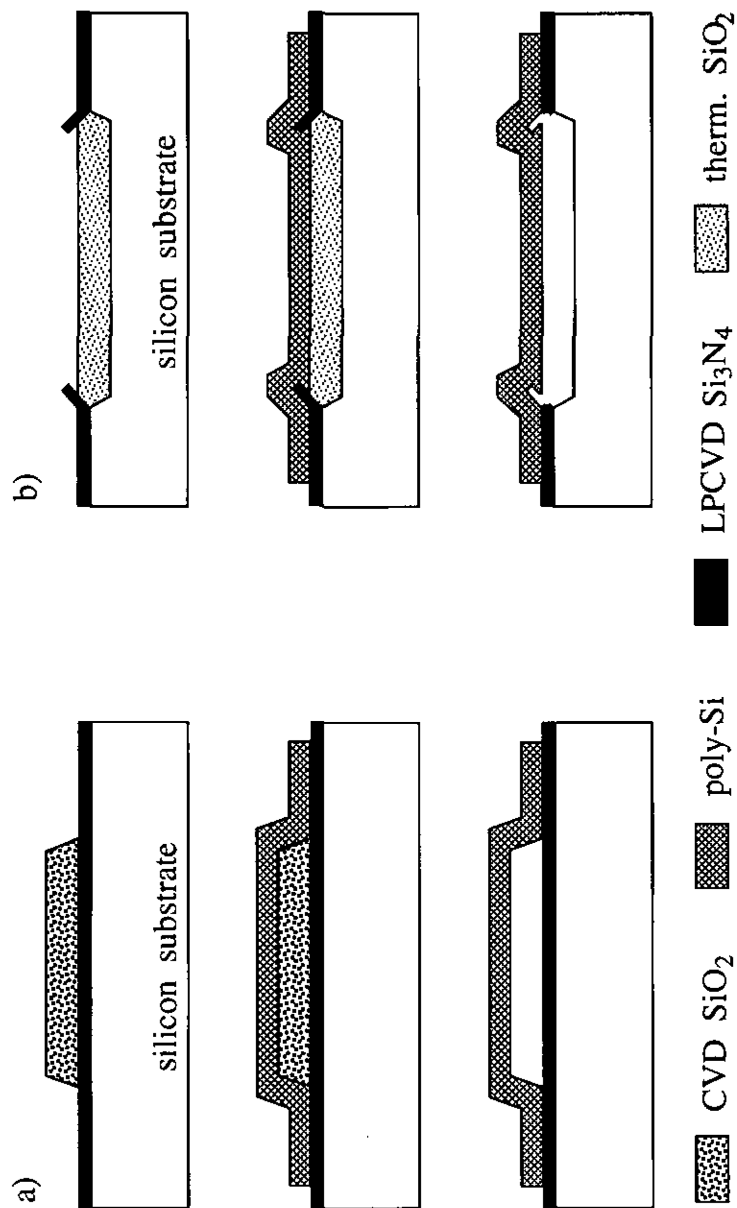

Fig. 2.1 Key processing steps for the fabrication of free-standing polysilicon beams: a) using CVD silicon dioxide; b) using local thermal silicon dioxide as sacrificial layer.

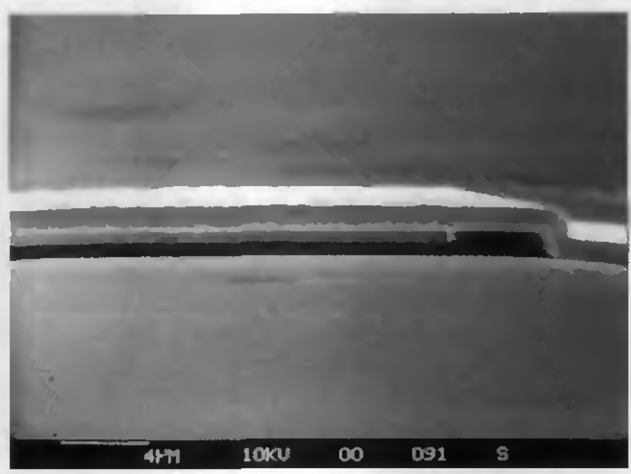

Fig. 2.2 Side view (SEM) of one end of a 1 μm thick free-standing phosphorus-doped polysilicon beam with CVD silicon dioxide as sacrificial layer.

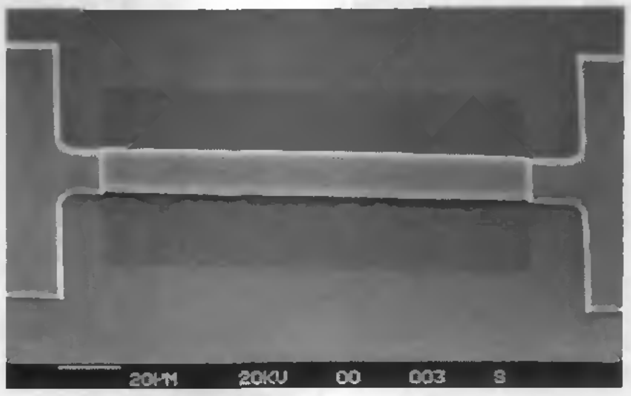

Fig. 2.3 Top view (SEM) of a 20 μm wide and 1.5 μm thick free-standing undoped polysilicon beam.

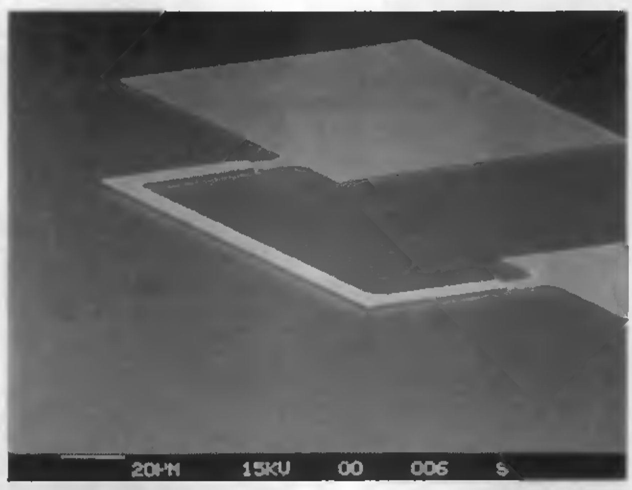

Fig. 2.4 SEM of an U-shaped free-standing P-doped polysilicon test structure for stress indication: large compressive stress would enlarge the bottom line of the "U" whereas tensile stress would diminish it. None ol these effects has been observed.

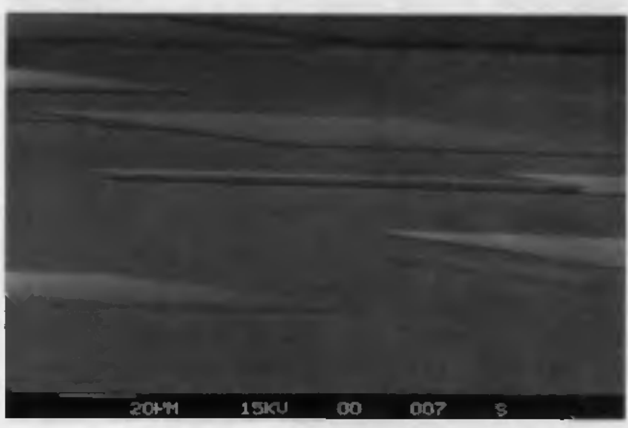

Fig. 2.5 SEM showing side view of a free-standing P-doped polysilicon cantilever beam (170 µm long, 25 µm wide and 1 µm thick).

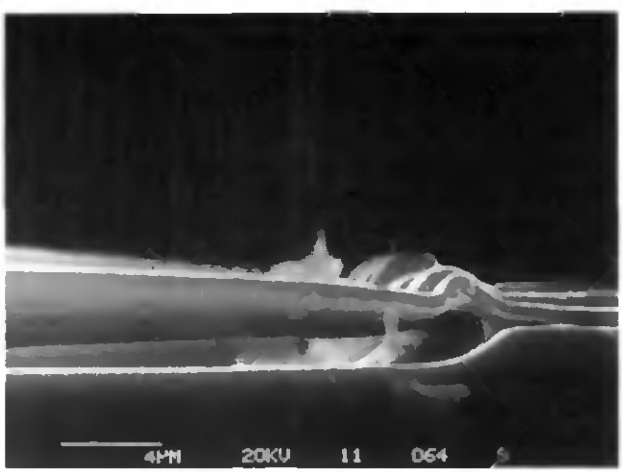

Fig. 2.6 Side view (SEM) of one end of a free-standing phosphorus-doped polysilicon/silicon nitride/patterned boron-doped polysilicon multilayer beam using a LOCOS process for the sacrificial layer.

Fig. 2.7 Cross section (SEM) of a partly underetched phosphorus-doped polysilicon beam with CVD oxide as sacrificial layer.

the beams are on the same level as the surrounding substrate (Fig. 2.1 b)). Two possibilities exist for achieving planar localized sacrificial oxides which do not step out of the substrate surface: one process uses a double thermal oxidation with BHF etching of the first oxide in between; the other technique consists of a silicon etch step (e.g. by reactive ion etching in SF_6/O_2 gases) followed by a thermal oxidation of the etched channels in the silicon substrate.

The SEM of Fig 2.6 shows one end of a completely underetched "LOCOS polysilicon beam" (using the double oxidation process mentioned above) . As indicated in the SEM and as shown schematically in Fig. 2.1 b), oxide growth occurs also underneath the silicon nitride at the ends of the windows and thereby pushes up the nitride mask (bird's beak effect). As a consequence, steps in the form of spikes are created at the ends of LOCOS polysilicon beams. Processes like side wall masked isolation (SWAMI) [e.g. 87] have been applied in IC technology to avoid or to reduce bird's beak effects. In these processes, channels are first etched in the silicon substrate (as in the second technique, mentioned above), and subsequently the sidewalls of the channels are covered with a nitride. Thus, the following oxidation of the substrate channels can be controlled in such a way that the edges of the nitride will not be pushed up beyond the substrate level. Recently, such an improved LOCOS process has also been reported for micromechanical polysilicon structures [88].

The lateral etch rate of the sacrificial silicon dioxide can be determined from SEMs as shown in Fig. 2.7. The following values have been obtained for the different oxides in HF etchants:

- 1 µm/min for thermal silicon dioxide in 49 wt.% HF,
- 1.5 µm/min for undoped Vapox in 49 wt.% HF,
- 0.33 µm/min for P-doped Vapox silicon dioxide in BHF 7:1.

2.2.2 Polysilicon Deposition and Doping Parameters

The undoped LPCVD polysilicon films are formed by pyrolysis (thermal decomposition) of silane (SiH_4) in a reduced-pressure hot-wall reactor. The reactor consists of a quartz tube heated by a three-zone furnace, with the gases introduced at one end and pumped at the other. The wafers stand vertically, i.e. perpendicular to the gas flow, in a quartz boat; the distance between the wafers is varied between 4 and 8 mm. Advantages of LPCVD systems are excellent film thickness uniformities of less than 5 % and large charge sizes between 20 and 200 wafers. The latter advantage compensates the major drawback of the LPCVD technique: the relatively low deposition rate that leads to long processing times, especially in the case of micromechanical structures which require film thicknesses of 1 µm or more.

The LPCVD parameters for polysilicon at the IMT are: 610 °C, 200 mTorr and 20 sccm SiH_4 100 %. The low deposition pressure and the small silane flow favour the diffusion of the arriving atoms on the wafer surface, leading thus to a more ordered and stable structure. The deposition temperature lies little above the transition point between amorphous and polycrystalline silicon which is reported to be about 580 °C at 200 mTorr [89]. Thus, relatively fine-grained polysilicon films (for higher deposition temperatures the grain size increases) are obtained which are advantageous for application as micromechanical structures [90,91].

As for the transition between amorphous and polycrystalline structure, the preferred orientation or "texture" of the polysilicon is greatly influenced by the above mentioned surface diffusion during deposition [92]. For instance, the {110} orientation is the dominant texture for LPCVD polysilicon deposited between 600 and 650 °C. At higher deposition temperatures the {100} orientation predominates, but the structure contains also non-negligible contributions from other orientations, such as {110}, {111}, {311} and {331}. If, due to these investigations [92] and according to the LPCVD parameters at the IMT, the {110} orientation is assumed to be the dominant texture for the polysilicon, the mechanical properties can be estimated by taking the corresponding data from monocrystalline silicon. For instance, the modulus of elasticity of polysilicon can thus be approximated to be 170 GPa (see section 1.1.2).

In many applications, micromechanical polysilicon structures are directly used as movable electrodes; therefore, doping is necessary. As described in section 2.2.1, doping at the IMT is performed by diffusion from doped Vapox layers [85]. While, at an early stage, most R&D laboratories performed doping of the micromechanical polysilicon structures by ion implantation [77], many of them have changed meanwhile also to doping by diffusion [14]. The latter method may less modify the mechanical properties of the free-standing microstructures; in addition, it is possible to dope the polysilicon symmetrically from the top and the bottom when using a doped sacrificial oxide (see section 2.2.1). For a 1 μm thick P-doped polysilicon film as used in the beam structure of Fig. 2.2, a sheet resistance of 850 ohms per square has been measured at room temperature, resulting in an average resisitivity of $8.5 \cdot 10^{-2}$ Ωcm. This corresponds to a phosphorus concentration of about $3 \cdot 10^{19}$ cm^{-3} according to the data from [28].

Figure 2.8 shows polysilicon steps where the beams are anchored to the substrate: a) for undoped and b) for P-doped polysilicon. The two SEMs indicate clearly that the surfaces are rather smooth for both the P-doped and the undoped polysilicon where they lie on the substrate (silicon nitride). Furthermore, Fig. 2.8 b) shows that the surface roughness of the free-standing part of the P-doped structure has been produced by the underlying P-doped sacrificial Vapox layer, and does not represent the grain

size of the (low) P-doped polysilicon which is expected to be in the range 0.05 - 0.5 μm [93]. Note the excellent step coverage of the undoped as well as the P-doped LPCVD polysilicon over the sacrificial oxide pattern where the slope of the oxide steps is given by the isotropic etching in BHF.

a)

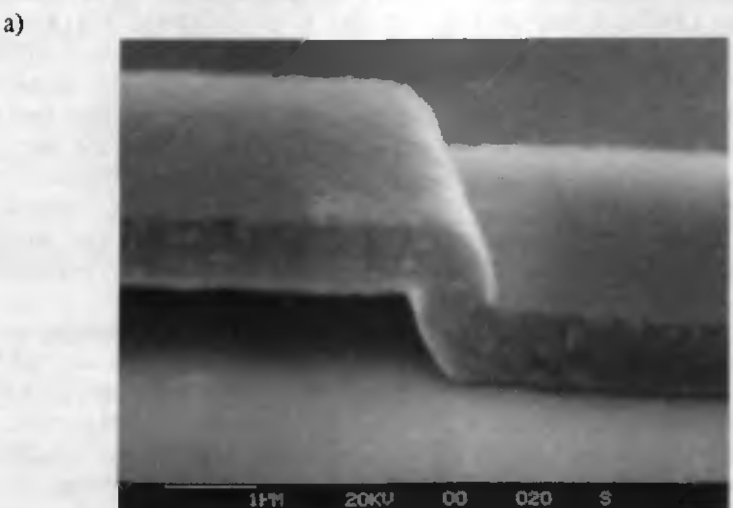

b)

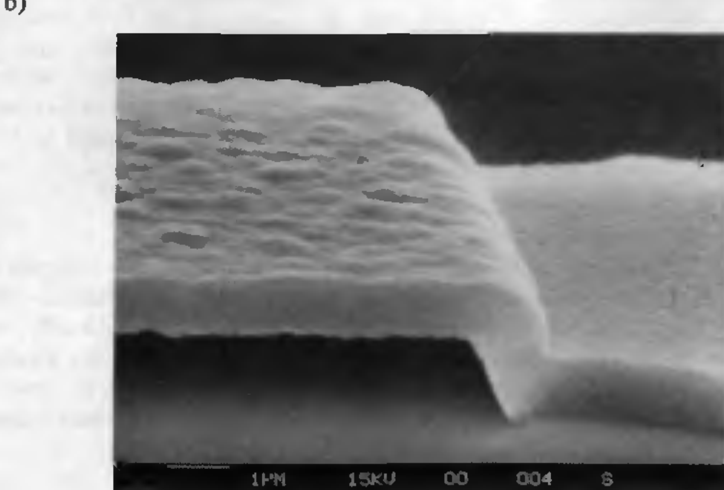

Fig. 2.8 SEM of polysilicon steps by which the beams are anchored to the substrate (with silicon nitride layer on top): a) undoped and b) phosphorus-doped polysilicon.

Buckling Problem

A major requirement to obtain released polysilicon microstructures without any mechanical failure, is the deposition of films with low residual strain. In particular, doubly supported free-standing polysilicon structures tend to buckle because of their residual compressive strain. By choosing appropriate LPCVD conditions (e.g. 580-590 °C [91], 600-610 °C [14,85], 630 °C [77]) and, in particular, by optimizing the annealing step (e.g. 1150 °C [91], 1050 °C [14,85], 1100 °C [77]), near stress-free or even slightly tensile micromechanical polysilicon structures have been achieved (see Table 2.1 for IMT process results). An adaequate explanation for the stress reduction in LPCVD polysilicon via high temperature treatment is given by Kamins [94]: any annealing step which allows the silicon atoms to move so that the defective regions (e.g. at the grain boundaries) become more ordered will increase the density; the resulting volume reduction is expected to reduce the compressive stress or to increase the tensile stress.

As described in 2.2.1, diffusion-doping and stress-annealing are performed in the same processing step at the IMT; the parameters are: 1050 °C, 30 min, N_2 flow. Furthermore, as mentioned above, the phosphorus concentration is less than 10^{20} cm^{-3}. According to Kamins [94], such a (relatively low) concentration does not lead to large changes in the structure of the polysilicon (e.g. no substantial grain growth) during annealing, nor create additional stress (for heavily P-doped polysilicon films, the phosphorus dopants preferably accumulate at the grain boundaries, and thus can affect the mechanical properties, e.g. by increasing the compressive stress). Finally, heat treatment below 1100 °C does not produce major changes in the dominant grain orientations of LPCVD polysilicon films deposited above 600 °C [89]. Hence the mechanical material constants like the modulus of elasticity of the 610 °C-polysilicon are not expected to be significantly modified during annealing at 1050 °C.

2.2.3 Sticking Problem

Table 2.1 summarizes some characteristics of different types of doubly clamped polysilicon beams [86,70]. The maximum length is defined as the maximum length of free-standing beams that are not bent upwards or downwards. It has to be added that a small increase of the maximum length is found on increasing the beam width. The most significant result, however, is that the P-doped polysilicon beams exhibit a considerably larger maximum length than the undoped beams.

SEM investigations on the mechanical strain of the different polysilicon films revealed that only the 1 μm thick P-doped beams longer than 500 μm showed slight buckling. Apart from those, no upward bending of other beams due to compressive stress was observed. However, the

Table 2.1 Maximum free-standing length and stress behavior of different types of doubly clamped polysilicon beams.

Film thickness	[μm]	Max. length [μm]	Stress
undoped poly-Si	undoped oxide		
0.2	0.3	<10	
0.8	0.9	65	no visible strain
1.5	1.6	135	
P-doped poly-Si	P-doped oxide		
1.0	1.2	>500	slight buckling
2.0	2.2	>700	no visible strain

maximum length of the different beams listed in Table 2.1 was in most cases limited by sagging and contacting the substrate as illustrated in Fig. 2.9.

Lober et al. [95] and Guckel et al. [96] mentioned surface tension effects from the liquid lateral etch and rinse baths, and bonding phenomena between the polysilicon beam and the substrate surface (Guckel) as possible reasons for this downward deflection and the attachment of the beams to the substrate. Scheeper et al. [97] found that water molecules, adsorbed on two silicon dioxide surfaces (substrate and free-standing beam), attract each other when, due to surface tension effects during drying, the surfaces come into contact: chemisorbed water molecules are chemically bonded as hydroxyl groups to the surfaces, and physisorbed water molecules are hydrogen bonded to the hydroxyl groups; thus, the hydrogen bonds keep the surfaces together.

According to our investigations [86], sticking is mainly due to forces having electrostatic nature. These forces might be produced by opposite electric charges at the polysilicon and the substrate surface (silicon nitride), respectively, and/or by hydrogen bonds (as pointed out by [97]) between the two negatively charged surfaces. However, in addition to the hydroxyl groups which might be created on the polysilicon surface as a consequence of the native oxide formation (the latter is stated by Mehregany et al. [98]), it is likewise possible that etch residues (e.g. fluorine compounds) on the surfaces [96] and/or other fixed negative charges (surface charges on silicon nitride are well-known phenomena) are hydrogen-bonded [99].

Electrostatic sticking also gives a possible explanation for the large difference in the maximum beam length between the undoped and the doped polysilicon. In the doped polysilicon much more mobile charge carriers than in the undoped are present. These mobile charges can partly compensate the fixed surface charges and thus reduce the electrostatic forces.

If electric potentials induced by surface charges and/or by hydrogen bonds are responsible for the attachment of the beams to the substrate, it

should be possible to release them and to shift them up again by applying external opposite electrostatic forces. Experiments seemed to confirm this assumption [86]. For instance, if the electron beam of the SEM was focused on polysilicon beams with rather short lengths (i.e. high restoring stiffness force) that were sagging and contacting the substrate, these beams could be switched up (the focused electron beam might have broken any hydrogen bonds). Furthermore, if a stuck polysilicon beam and an underlying substrate electrode were set to the same positive electric potential (typically 30 V for 300 μm long beams) with respect to the surrounding substrate as sketched in the upper part of Fig. 2.10, it was likewise possible to switch the beam up. Details on the fabrication, the modeling and the operation of electrostatic beams as shown in Fig. 2.10 are given in the chapter 3.

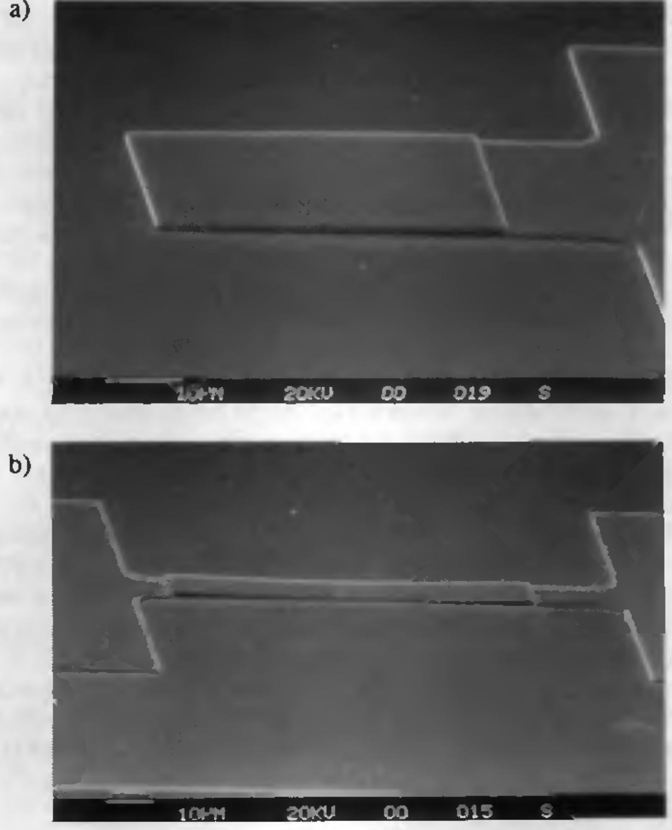

Fig. 2.9 SEMs of undoped polysilicon beams which bend downwards and stick to the substrate: a) cantilever and b) doubly clamped structure.

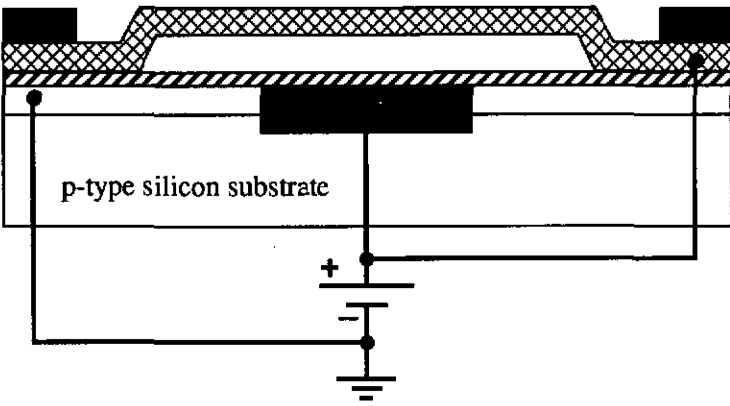

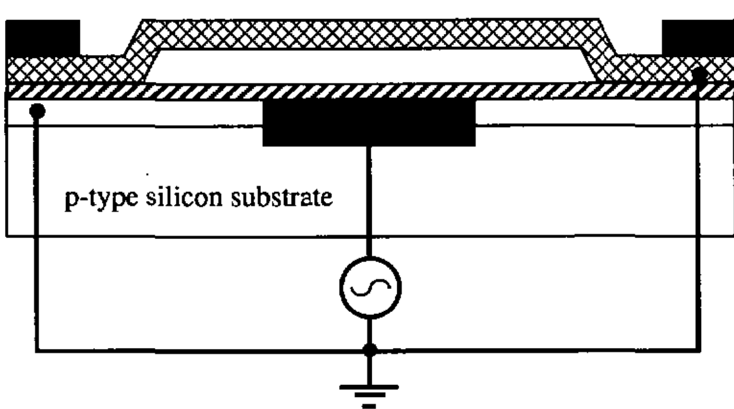

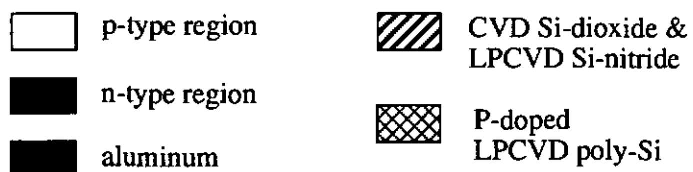

Fig. 2.10 Electrostatic activation for releasing polysilicon beams which are stuck to the substrate, by setting the beam to the same electric potential as a substrate electrode (top scheme), by applying an a.c. voltage (in the range of the mechanical resonance frequency) to the beam (bottom scheme).

Several techniques have been applied for reducing and avoiding the attachment of the beams to the substrate during rinsing and drying. A promising method is the removal of the rinsing liquid by freeze drying, first proposed by Guckel [96]. Another simple freeze-drying procedure using t-butyl alcohol has been reported by Takeshima et al. [100]: After HF etching and dehydration with isopropanol, the wafer is immersed in liquid t-butyl alcohol (i.e. at a temperature above the melting point which is at about 26 °C). Next, the wafer in t-butyl alcohol is placed in a refrigerator where the t-butyl alcohol is frozen. Subsequently, the wafer is transferred into a vacuum system. By evacuation, the frozen t-butyl alcohol is sublimated and the dried free-standing structures are obtained.

A further method to avoid sticking of the polysilicon beams after removal of the sacrificial oxide has been proposed by Kovacs et al. [101]: After HF etching and different rinsing and cleaning procedures, the wafer is immersed in a photoresist-acetone mixture, soft-baked and subsequently stripped in an O_2 plasma, leaving thus the polysilicon structures free-standing.

To prevent any later re-sticking e.g. during operation in (humid) air, the structures are finally passivated, for instance by a thin LPCVD nitride layer. If direct contact with the environment is not necessary, the optimum solution is to place the beam structures in a microcavity that contains an inert atmosphere. During testing and operation on prototype level, beams attached to the substrate can most often be freed with a probe tip. A further efficacious method consists in electrostatic excitation of the stuck beams by applying an a.c. signal (in the order of the mechanical resonance frequency) as indicated in the lower scheme of Fig. 2.10. The latter method could also be applied as self test when using the polysilicon beams on industrial level.

2.2.4 Surface Encapsulation

By extending the sacrificial layer technology, it is possible to encapsulate the above-described micromechanical devices on surface level [91]. For instance, a second silicon dioxide/polysilicon layer combination can be deposited after the definition of a polysilicon beam on a first sacrificial oxide. The beam structure has to be completely covered by the second oxide and similarly the whole pattern of the second oxide must be coated by the second polysilicon structure. Thin oxide lanes underneath the second polysilicon serve as entrance channels for the hydrofluoric acid. Both sacrificial oxides are then etched in one processing step. After the sacrificial oxide removal the etch channels are closed, e.g. by LPCVD of nitride or polysilicon. Thus, a low-pressure surface microcavity is formed whose cap consists of the second polysilicon. Inside the microcavity the free-standing

beam is located and hence protected against pollution (e.g. humidity which could cause sticking of the beam as described in section 2.2.3).

Special attention has to be paid to the adhesion of the second polysilicon layer. The latter is generally anchored on a silicon nitride on the substrate. If due to high temperature treatment, the nitride surface has been oxidized, the lateral sacrificial layer etching may also "lift-off" the second polysilicon.

The SEMs of Fig. 2.11 show an encapsulated microbeam structure [70]. In contrast to chip by chip packaging, surface encapsulation can be batch-fabricated, thereby reducing costs and increasing reproducibility. However, the thin-film caps are very fragile and will not guarantee mechanical protection. Their main application will be to create a well-controlled low-pressure atmosphere for the encapsulated microstructure.

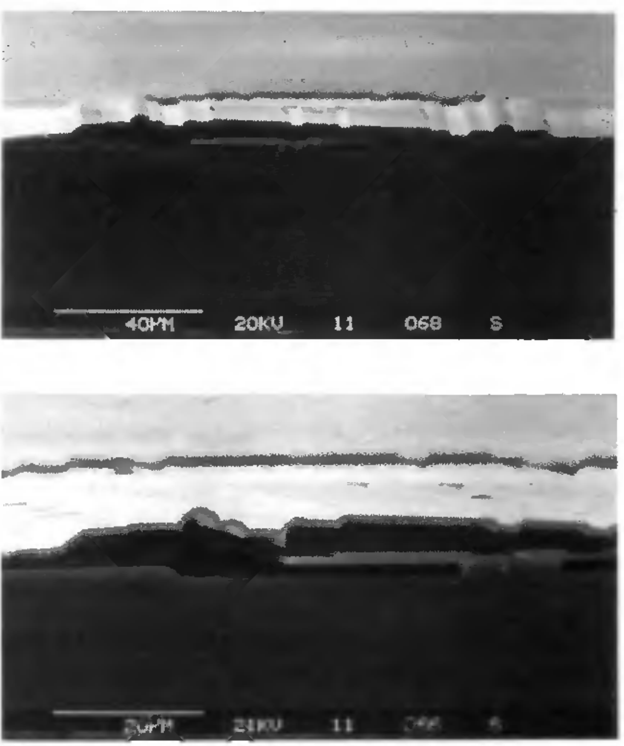

Fig. 2.11 SEMs (cross sections: overview and close-up) of a polysilicon beam (the lower sacrificial oxide is not completely removed yet) encapsulated by a second polysilicon cover; the distances between cover, beam and substrate are 2.2 μm and 1.8 μm, respectively.

2.3 Silicon Dry Etching by Plasma for Use in Micromachining

2.3.1 (Poly-)Silicon Etching Parameters

One possibility to reduce device failure such as sticking or buckling of micromechanical polysilicon structures consists in increasing the film thickness to more than one micron. The etching of such "thick thin films" becomes a delicate processing step, especially for high-aspect ratio structures, i.e. for structures with thicknesses greater than their lateral dimensions. A similar situation is found in silicon bulk micromachining where the fabrication of three-dimensional structures involves the etching of the silicon substrate with depths ranging from a few microns to more than several hundred microns. Experiments have shown that the same etchants (may be with different parameter adjustment such as volume ratio of the components) can be used for both monocrystalline and polycrystalline silicon. Since these (poly-)silicon etching steps for micromachining applications are usually only part of a complex fabrication sequence, several requirements have to be met. For instance, process-compatible masking materials should be applied, e.g. photoresist or an already existing layer. Furthermore, the (poly-)silicon needs to be etched much faster than the masking material. Finally, for exact definition of the geometrical dimensions of the microstructures, it is necessary that etch depth and profile are well controllable and reproducible.

In traditional thin-film technology, wet etchants have been employed for many years for the structuring of silicon [102]. Mixtures of HNO_3, HF, CH_3COOH and/or water attack the silicon isotropically and exhibit relatively high etch rates (10-300 μm/min); however, the etching process is difficult to control. When the polysilicon technology was started at the IMT, wet etching was the only tool available for patterning. Using an etchant with a 50:3:20 volume ratio of HNO_3(70%):HF(50%):H_2O, the etch rate of polysilicon is about 1 μm/min. Photoresist withstands about 2 min before losing adhesion; in addition, the adhesion problem in combination with the isotropic etching character produce a large undercut. Silicon dioxide or aluminum are strongly attacked and can not be used as masking materials. Thus, wet etching of polysilicon is a rather problematic affair, especially when the lateral dimensions of the patterns should be well controlled and for film thicknesses of 1-2 μm.

A promising possibility in sculpturing three-dimensional structures out of silicon is the use of dry etching, a well-established process in IC technology [103]. In the following, plasma etching techniques for silicon micromachining with large etch depths as well as for polysilicon are described [104,105].

Experimental Setup and Procedures

Two parallel plate reactors with 13.56 MHz RF generators are used. For both systems loadlocks guarantee low contamination. The active gases are fed through the showerhead like upper electrodes and thus lead to an excellent etching uniformity. The wafers are placed on the lower electrode. For optimum uniformity, single wafer processing is chosen. In the first system, which uses SF_6/O_2 gases for the etching of silicon, the RF power can be capacitively coupled either to the upper electrode (plasma etching mode: PE) or to the lower one (reactive ion etching mode: RIE). In the second system, where the etching is performed by C_2ClF_5/SF_6 gas mixtures, only RIE can be applied.

Table 2.2 summarizes the main process conditions on the left-hand side and the results of the deep dry etching trials of silicon on the right. Positive photoresists (AZ 1518 and AZ 4562) with different thicknesses, thermal silicon dioxide and electron-beam-evaporated aluminum as IC-compatible masking materials are compared. The selectivity is defined as the ratio of the etch rates between silicon and the masking material. The undercut is calculated by dividing the lateral underetch distance (determined by SEM observation) by the vertical etch depth.

Fluorine/Oxygen Gas Mixtures

In the first phase, SF_6/O_2 gases were tested because they offer high selectivity and thereby deep silicon steps [e.g. 106]. These gas combinations are also well known for dry etching of (poly-)silicon in IC technology [e.g. 107]. For optimum etch results the PE mode instead of RIE has been chosen for the deep etching of monocrystalline silicon. Since the silicon substrate is grounded for PE, it is subjected only to low-energy ion bombardment. Hence, higher power can be applied than in the RIE mode. The greater power leads to the production of more active etching ions. Thus, the decrease of the etch rate due to the low-energy impact can be compensated by an increase of reactive species. Furthermore, the photoresist is less damaged in the PE mode because of the low ion bombardment. We finally found, for similar silicon etch rates, a selectivity that is at least three times better than that for RIE.

Using a standard IC photoresist (AZ 1518) an etch depth of 46 µm has been obtained. As indicated in Table 2.2, with a thicker photoresist (AZ 4562) the depth could be increased to more than 100 µm at a selectivity of about 20. The SEM of Fig. 2.12 shows the profile of an etched silicon step where the AZ 4562 has not been stripped yet. It is clearly indicated that the fluorine gases lead to a large undercut. This is due to the isotropic fluorine atom etching of silicon which is known to be considerably high compared with the vertical etch induced by ion bombardment. Furthermore, the

addition of O_2 increases the generation of reactive F-radicals and simultaneously impedes the formation of organic redeposition by reaction with carbonic compounds resulting in volatile products.

The SEM of Fig. 2.13 shows the cross section of a 1 μm high polysilicon step with the hardly attacked AZ 1518 still on top. Since RIE has been used for polysilicon, the selectivity is found to be somewhat lower; however, this is not problematic for film thicknesses of up to a couple of microns. As further indicated in Fig. 2.13, the polysilicon exhibits a slightly larger undercut than the profile of the silicon step in Fig. 2.12. For the latter, the long etching has removed a big part of the photoresist which probably has produced redeposition on the silicon sidewalls thus lowering the lateral etching.

Increasing the exposed silicon surface results in a rise in the etch rate. Furthermore, we observed that the photoresist mask deteriorates faster. The damage of the photoresist is mainly caused by the increasing temperature of the substrate, since more etch reactions take place due to the increased exposed silicon area. At higher temperature the etching species are also more reactive and thus, the chemical part becomes more dominant than the physical bombardment. This results in a higher etch rate with greater undercut. However, the effect of rising etch rate with increasing exposed silicon surface can only be sustained if the consumption of reactive ions is smaller than the generation rate. Otherwise a loading effect can occur and thereby decrease the etch rate.

Etch experiments were also carried out using silicon dioxide as masking material. In contrast to photoresist, it was possible to increase the RF power and to lower the working pressure without taking the risk of burning or damaging the oxide mask. The oxide etch rate turned out to be even smaller than that of the photoresist. A selectivity of 85 and etch depths up to 150 μm have been achieved.

As a third IC-compatible masking material, aluminum was applied. First tests revealed that at relatively high silicon etch rates, the aluminum mask is barely etched at all in SF_6/O_2 gases; the oxygen seems to form alumina out of the aluminum, and the alumina is resistant in fluorine plasmas. Thus, it was possible to realize silicon steps of more than 500 μm.

Since silicon nitride is also attacked by SF_6/O_2 gases, an aluminum mask can be used for the patterning of polysilicon/nitride multilayers. Thus, burning of photoresist during multilayer-RIE is avoided, and in addition, redeposition effects which occur when etching nitride down to (poly-)silicon, are lowered.

For fixed RF power the working pressure of the plasma-etching reactor at the IMT was optimized in view of small undercut and high etch rate. Maximum etch rates of 1.5 ± 0.5 μm were found between 0.08 mbar and 0.12 mbar for a power range of 250 ± 50 W. At pressures lower than

0.03 mbar the power had to be reduced in order to avoid high energy ion impact that would have damaged the masking material. Because of the low power, however, the etch rate decreased considerably. Finally, we observed no significant change in the undercut and etch profile between 0.03 mbar and 0.07 mbar. As pressure was increased from 0.08 mbar to 0.12 mbar, the sidewalls became more and more rounded [108].

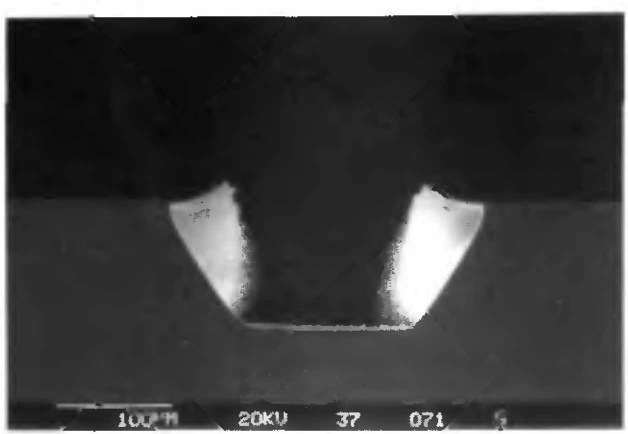

Fig. 2.12 Silicon etch profile etched with SF_6/O_2-plasma and a photoresist mask (not yet stripped).

Fig. 2.13 Cross section of a polysilicon pattern which has been etched in a SF_6/O_2 plasma (the photoresist is still on top).

Chlorine/Fluorine Gas Mixtures

In order to reduce the undercut produced by SF_6/O_2 gases, chlorine/fluorine gas mixtures were examined which are reported to exhibit good anisotropy [109,110]. RIE of silicon using C_2ClF_5/SF_6 gas combinations was performed at relatively high RF power. Thereby, the silicon etch rate, which is normally small for chlorine gases, could be increased to about half a micron per minute. Since, however, photoresist is strongly attacked in chlorine gases, a rather high working pressure was chosen to weaken the etching by ion bombardment.

As shown in Table 2.2, silicon etching up to 30 μm has been achieved with a selectivity of more than five, by using thick photoresist (AZ 4562). Fig. 2.14 shows the profile of an etched step in the silicon substrate. An almost perfect anisotropy is observed, i.e. practically no undercut and vertical sidewalls. One reason may be that chlorine atoms cover the silicon surface and thereby slow down further etching reaction. Especially on the sidewalls, where the energetic ion bombardment is low, only a few volatile $SiCl_x$ compounds are produced and almost no etching occurs [111].

The advantages of RIE in C_2ClF_5/SF_6 gases, a reproducible small undercut and almost vertical profiles, have been exploited for the realization of high-aspect ratio polysilicon beams. A standard photoresist was used as mask for the definition of the structures of Fig. 2.15.

Applying silicon dioxide as masking material resulted in a similar maximum etch depth as for the 6.2-μm-thick AZ 4562; i.e., 34-μm-deep silicon steps have been achieved using 1.8-μm-thick thermal oxide. However, in contrast to the photoresist mask, the oxide mask exhibits an undercut. (A similar effect has also been noticed for SF_6/O_2 gases: using silicon dioxide instead of photoresist as mask leads to an enhanced undercut.) A possible explanation is that more radicals containing carbon are generated during etching with photoresist than with an oxide mask. Such radicals can react on the surfaces and produce polymer films. These polymer depositions preferably stay on the sidewalls which are only subjected to low energy impact and thus, impede lateral etching. An additional reason for an increased undercut may be that silicon dioxide as masking material prevents polymer film formation because the oxygen released during etching reacts with the unsaturated species to form volatile products [103].

When only a small part of the wafer is covered with photoresist, the same effect has been observed as for SF_6/O_2 gases: the photoresist is damaged faster. Thus, maximum etch depths are smaller and, in addition, the high anisotropy is lost. For example, when less than 50 % of the wafer was covered by AZ 4562, an etch depth of 20 μm and an undercut of 0.2 were measured.

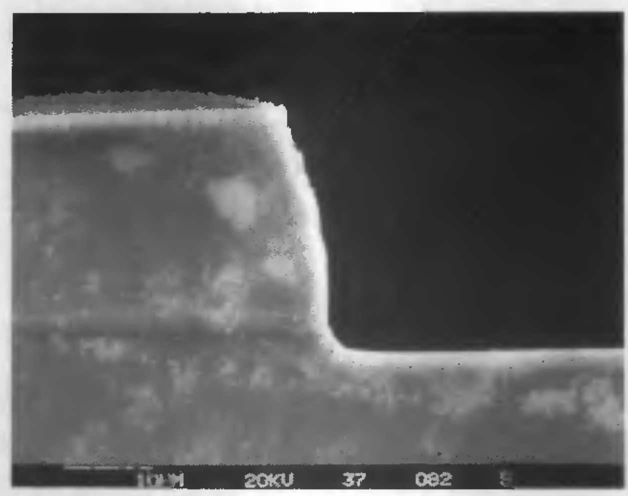

Fig. 2.14 Silicon profile etched with C_2ClF_5/SF_6-plasma and a photoresist mask (not yet stripped).

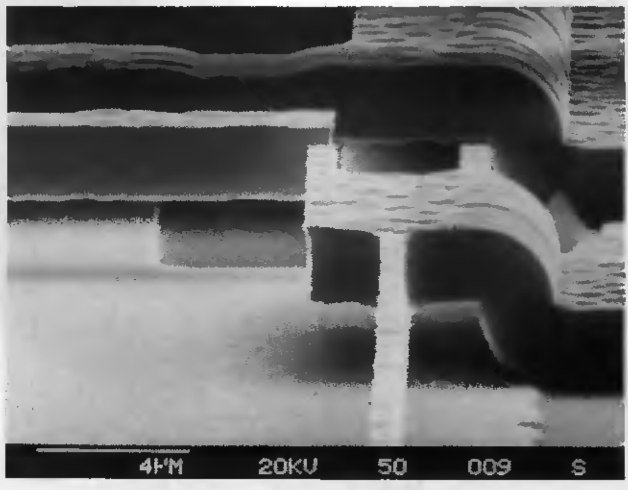

Fig. 2.15 SEM showing a close-up of one end of a high-aspect ratio polysilicon beam (0.6 μm wide and 2 μm thick) where it is anchored to the substrate. Note the reasonably vertical profile of the polysilicon patterns.

Table 2.2 Process parameters and results of deep dry etching of silicon.

Gases	Mask material	Mask thickness [μm]	Mode	Pressure [mbar]	Power [W]	Etch-depth [μm]	Etch-rate Silicon [μm/min]	Selectivity	Undercut vs Depth
SF_6/O_2	AZ 1518	1.8	PE	0.07	220	46	0.9	28	0.55
SF_6/O_2	AZ 4562	6.2	PE	0.07	220	110	0.9	20	0.55
SF_6/O_2	Therm. SiO_2	1.8	PE	0.05	300	150	1	85	0.65
SF_6/O_2	Aluminum	1.8	PE	0.07	300	>500	1.3	>300	0.8
C_2ClF_5/SF_6	AZ 4562	6.2	RIE	0.12	180	30	0.6	5.2	0
C_2ClF_5/SF_6	Therm. SiO_2	1.8	RIE	0.1	160	34	0.5	19	0.56

2.3.2 Further Device Examples Based on Dry Etching

Silicon dry etching by plasma processing can be applied to the fabrication sequence of several micromechanical structures. For instance, taking advantage of the isotropic etching behavior of silicon in SF_6/O_2-plasmas, silicon dioxide as well as aluminum microstructures on the silicon substrate can be completely undercut and thereby become free standing. Figures 2.16 and 2.17 show examples of dioxide beams realized by this technology. In particular, the doubly clamped buckled beams of Fig. 2.16 indicate clearly the compressive stress of the thermal dioxide on the silicon. Figure 2.18 illustrates examples of stress-free aluminum beams. Potential applications of these free-standing micromechanical structures are resonators and mechanical switches. A particular advantage is that only one mask and three fabrication steps are necessary: film deposition and patterning of the beam structures, and releasing of the beams from the substrate by plasma etching.

The same method of isotropic plasma etching has also been successfully applied by Zhang and MacDonald [112] for the fabrication of free-standing silicon cantilever beams. Furthermore, Hirano et al. [113] used this "dry releasing" for constructing electroplated rotational (micromotors) and overhanging structures (e.g. hot-wire micro flow-meters).

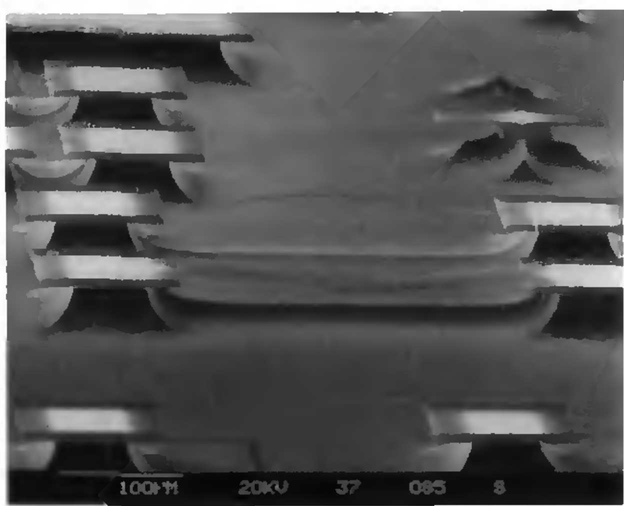

Fig. 2.16 SEM showing free-standing silicon dioxide bridges fabricated in a SF_6/O_2-plasma by selective underetching of the silicon substrate.

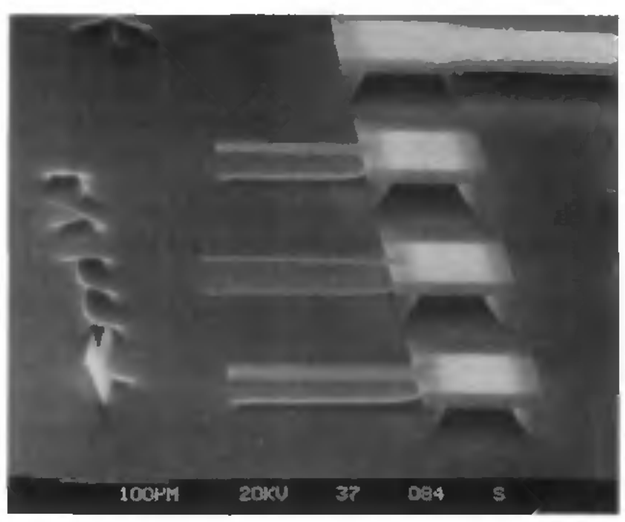

Fig. 2.17 SEM showing free-standing silicon dioxide cantilevers fabricated in a SF_6/O_2-plasma by selective underetching of the silicon substrate.

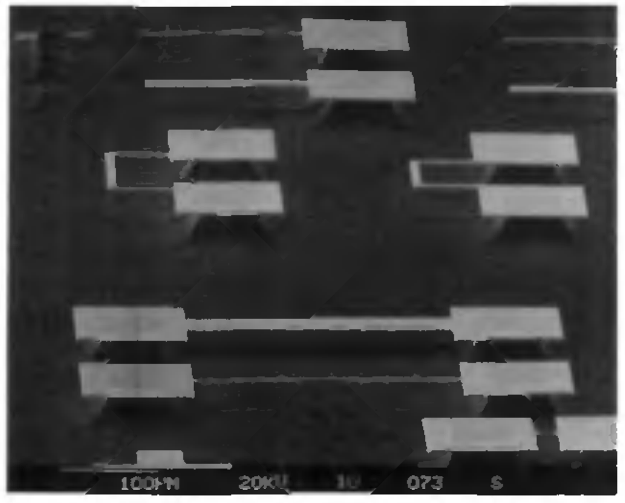

Fig. 2.18 SEM showing free-standing aluminum microstructures fabricated in a SF_6/O_2-plasma by selective underetching of the silicon substrate.

Since aluminum exhibits a remarkable resistance against SF_6/O_2-etching and the etch rate of silicon is highly controllable, it is possible to fabricate membranes out of silicon wafers by using dry etching techniques. The SEM of Fig. 2.19 shows a cross section of such a dry-etched prototype membrane where the aluminum mask has not been removed yet. As illustrated in the SEM, the roughness of the etched surface area measures between 15 µm and 20 µm, i.e. about 5 % of the etch depth, which is about 360 µm. Such plasma-etched silicon membranes could serve as thin substrates, for instance, for elements which have to be thermally isolated from the rest of the chip, and which do not allow processing in KOH or EDP.

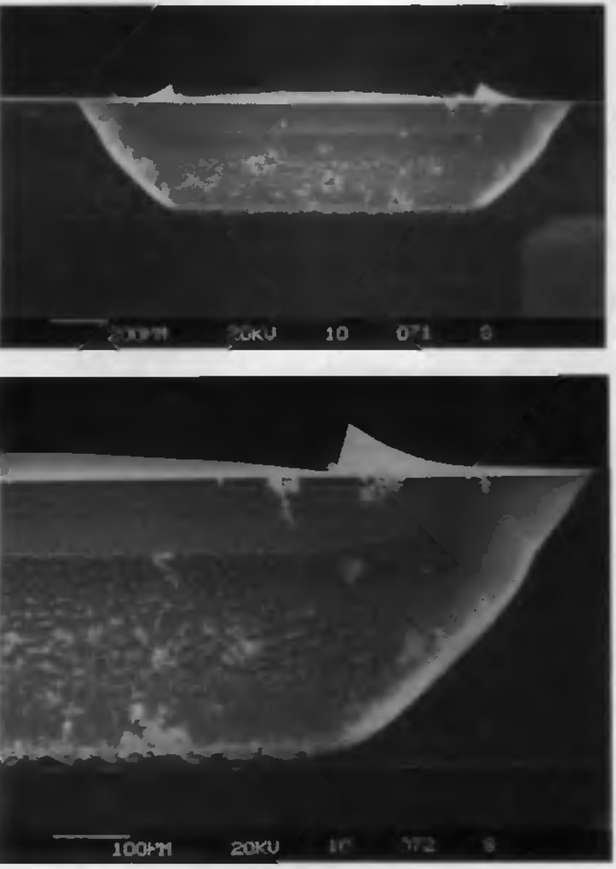

Fig. 2.19 SEMs showing cross sections (overview and close-up) of a silicon membrane (thickness: 15 ± 10 µm) fabricated by dry etching in a SF_6/O_2-plasma with an aluminum mask.

2.4 Combination of Bulk and Surface Processing

By exploiting the large variety of micromachining tools, increasingly complex devices can be realized. In particular, for a growing number of applications, surface and bulk processing are combined in the fabrication sequence [114-118], and it becomes often difficult to distinguish pure surface and bulk machining techniques. In agreement with Petersen [115], we can define surface-micromachined devices as threedimensional microstructures at the substrate surface with vertical dimensions ranging from 1 μm to about 30 μm. In the following, three examples are discussed whose fabrication is based on complex micromachining using special techniques developed at the IMT laboratory.

The structure of the first example has already been shown in Fig. 1.7: a free-standing polysilicon microbridge on a monocrystalline silicon membrane for application as highly-sensitive resonant pressure sensor (see also section 4.5). Anisotropic etching in KOH for the membrane formation is combined with the sacrificial layer technology. The key processing steps are given in Fig. 2.20; a double-sided polished silicon wafer is used. The sacrificial silicon dioxide structure on the topside of the wafer and the windows in the thermal oxide for KOH etching of the silicon on the wafer backside are defined by double-sided photolithography and BHF etching. LPCVD and doping of polysilicon is followed by patterning of the beams on the topside and by removal of the polysilicon on the backside of the wafer. The topside is then protected by mounting the wafer in a mechanical chuck leaving only the backside exposed. The whole chuck is immersed in KOH solution for etching the silicon down to a membrane thickness of about 10 μm (the thermal oxide on the wafer backside is used as a masking material). After the membrane formation, the sacrificial oxide is laterally etched for releasing the polysilicon beams.

A further extension of the fabrication process is indicated in the last cross section of Fig. 2.20: the on-wafer encapsulation of the free-standing polysilicon beams by means of anodic (electrostatic) bonding of a silicon cap wafer via a sputtered Pyrex glass film to the sensor wafer [e.g. 42,119]. Thus, the resonant structures are well protected against parasitic environmental effects (e.g. humidity). Bulk encapsulation by means of a cap wafer is preferred, since it leads to a more robust device than a surface-encapsulated structure. The anodic bonding between the 4 μm thick Pyrex layer on the cap wafer and a polysilicon film on the sensor wafer (the same polysilicon layer can be used which serves also for the free-standing structures) is performed at 200 – 400 °C by applying voltages between 50

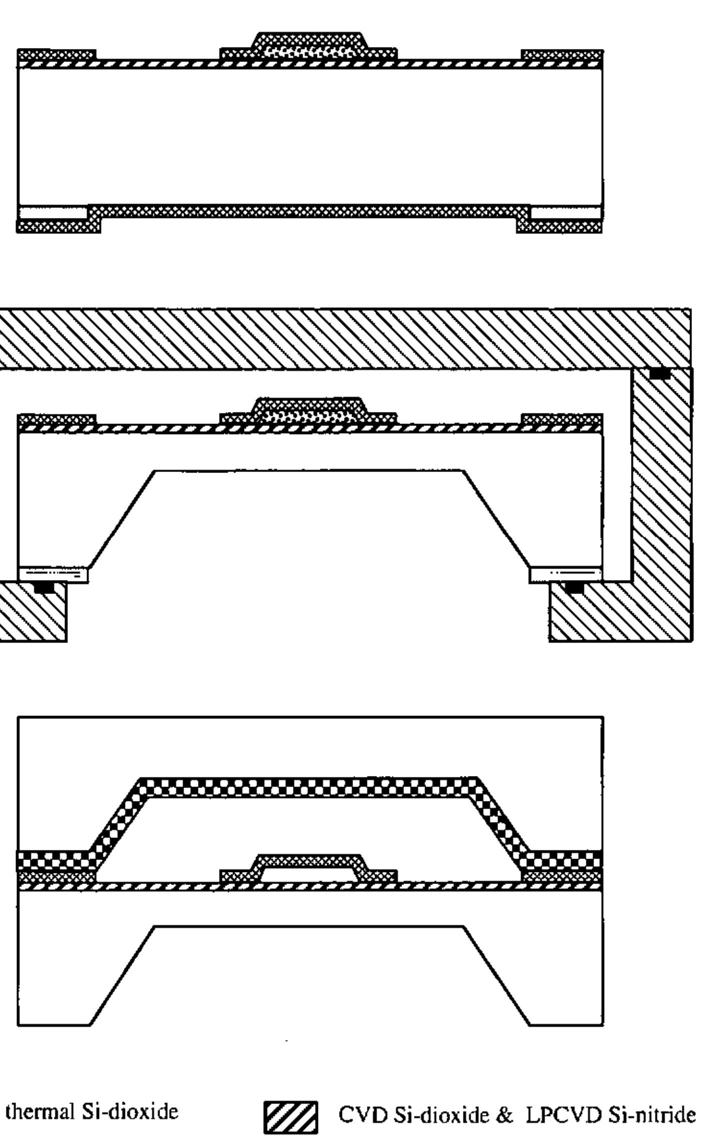

Fig. 2.20 Key processing steps of an encapsulated free-standing polysilicon beam on a silicon membrane; the sacrificial layer technology is combined with anisotropic etching in KOH and anodic bonding by means of a Pyrex film.

and 200 V. First tests of anodic bonding of two wafers using a Pyrex interface layer have been successfully carried out in collaboration with the Technical School NTB, Buchs (SG), Switzerland.

The second example illustrates another important two-step micromachining process, the combination of wet and dry etching, originally used in the fabrication process of a fully bipolar-compatible micromachined accelerometer [105,120]. A silicon cantilever with square cross section (15 μm by 15 μm) and integrated tip has been realized; the device is applied in bidirectional force microscopy, i.e. measurements of both interatomic forces (vertical to the surface) and friction forces (parallel to the surface) can be performed [121,122]. The main fabrication steps are shown in Fig. 2.21. After the formation of a 25 μm thick membrane in the silicon wafer by means of KOH etching, a double-layer mask consisting of a thermal oxide and a 6.5 μm thick photoresist is patterned on the topside of the wafer. Subsequent RIE in a C_2ClF_5/SF_6-plasma from the wafer topside down to a depth of 15 μm defines the enlarged cantilevers with nearly vertical sidewalls out of the membrane. Next, a short wet isotropic etching step in a $HNO_3/HF/CH_3COOH$ mixture undercuts the remaining part of the double-layer mask and thus forms a sharp integrated tip on the cantilever. Simultaneously, the rest of the membrane (10 μm) is pierced through and thereby the cantilevers are released; the latter are also narrowed by the isotropic etching step, however, the vertical profile of the former RIE is not much affected. The SEM of Fig. 2.22 shows such a meander-shaped silicon cantilever with integrated tip.

An extension of the above structures for atomic force microscopy has resulted in an overhanging *xy* translator (see also chapter 3.4) with integrated protruding tip [123,124]. This rather complex device includes several surface and bulk micromachining steps. Two thermally oxidized silicon wafers are sealed together by means of silicon fusion bonding at 1100 °C [e.g. 42,125]. The upper wafer which has been pre-structured by RIE in a C_2ClF_5/SF_6-plasma is thinned down to a membrane using KOH etching, and similarly as before, beams with integrated tips are sculptured out of that membrane. During KOH etching, via holes have also been opened in the lower support wafer. By final sacrificial layer etching of the thermal interface oxide between the two wafers, the beam structures with the integrated tips are released and leave suspended over the via holes of the support wafer.

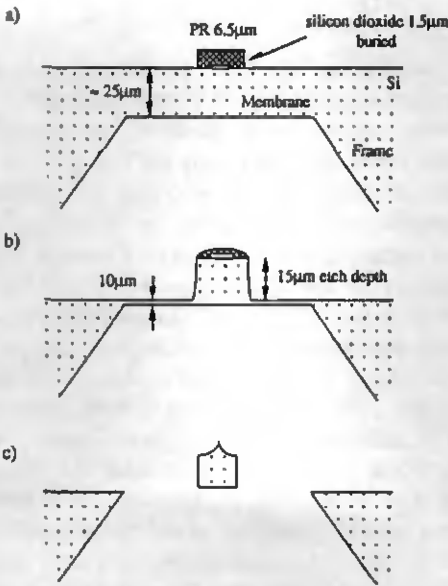

Fig. 2.21 Fabrication process of a silicon cantilever with integrated tip [121,122]: a) double-layer mask for tip on KOH-etched 25 µm-membrane; b) RIE in C_2ClF_5/SF_6-plasma producing enlarged cantilever; c) wet etching in $HNO_3/HF/CH_3COOH$ mixture for cantilever release and tip formation.

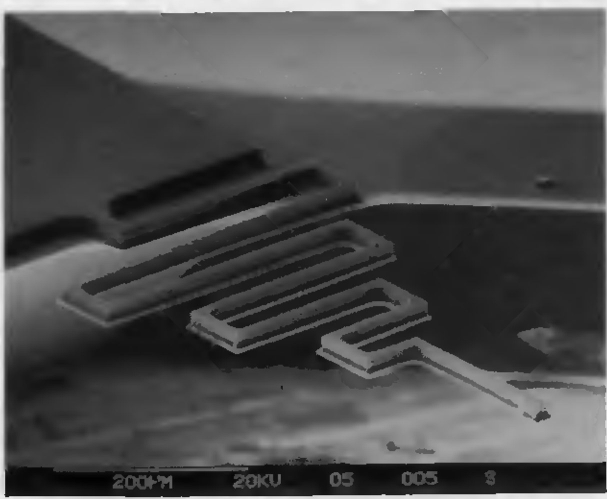

Fig. 2.22 Monocrystalline silicon cantilever with rectangular cross section and integrated tip fabricated by the process described in Fig. 2.21.

2.5 Conclusion

Surface micromachining has been demonstrated to be an attractive alternative to the well-established bulk micromachining of silicon. However, bulk and surface micromachining techniques are not only diverging or competing with each other, but they will also help to increase the wide variety of batch-fabricated high-reliable microsensors and microactuators in silicon and the integration of the latter with microelectronics. Bulk micromachining, for instance, will be preferably used in applications where the mechanical fragility or the small masses of surface-micromachined structures are major drawbacks. If an IC-compatible fabrication process is needed for a special application, surface-micromachined devices which consist of polysilicon, silicon dioxide and/or aluminum are advantageous.

Free-standing polysilicon structures have been fabricated by selective lateral etching of a sacrificial silicon dioxide layer, which has been sandwiched between the polysilicon film and the substrate. LPCVD, phosphorus-doping and annealing parameters have been adjusted for optimum (electro)mechanical properties of the polysilicon. Methods such as freeze-drying during fabrication or capacitive a.c. activation during operation have been described for avoiding sticking of the free-standing structures on the substrate. Furthermore, surface encapsulation has been shown: by applying two sacrificial-layer processing steps, free-standing polysilicon beams have been micro-packaged on the substrate surface by using polysilicon caps.

Novel highly reproducible dry etching techniques have been reported which are promising for application in silicon micromachining. For instance, by employing fluorine-based plasma etching, thin-film structures like aluminum beams have been released by undercutting the silicon substrate, and due to the excellent selectivity, entirely plasma-etched silicon membranes have been realized. Dry etching by plasma in fluorine/chlorine gas mixtures has been successfully applied for defining submicron-wide high-aspect ratio polysilicon beams.

For a growing number of applications, the combination of surface and bulk micromachining turns out to be an essential processing step; device examples are polysilicon resonators on silicon membranes for high precision pressure measurement, or overhanging silicon cantilevers with integrated tips for use in atomic force microscopy.

3 Electromechanical Polysilicon Actuators

3.1 Introduction

Micromachined actuators having dimensions ranging from micrometers to millimeters represent potential tools for microrobotics, e.g. for medical use or for assembly and manipulation of nanomachines [126,127]. Furthermore, such actuators can be incorporated in microsystems, for instance, in miniature chemical analysis systems [128] where silicon valves are integrated with ion sensitive field effect transistors. Another application is the scanning tunneling microscope as a micromachine [129].

A wide variety of driving principles exists including powering by laser or by bimetal (or bimorph) effect and piezoelectric or electrostatic actuation. For the evaluation of the driving methods and for the estimation of the characteristics of the microactuators, among other criteria like fabrication technology or efficiency, special attention has to be paid to the scaling of the forces, spring constants, weights etc. when entering the microscale world [130,131]. Furthermore, in order to be compatible with IC components in microsystems, an important issue of the actuators is a low driving voltage.

Optical excitation by laser [132-134] – most often applied for resonant structures – as well as the bimetal effect [135,136] are based on thermal powering, where thermal changes produced during operation alter the material properties and thereby can modify the overall characteristics of the actuators [137]. A particular advantage of these thermally driven actuators are the large amplitudes of several tens of microns, for example by applying IC voltages between 10 and 20 V (input power: 10-100 mW) to bimetal structures. Using laser excitation, the input power is typically in the mW range. Whereas the bimetal actuators can be fabricated by IC-compatible thin-film technology combined with bulk micromachining of silicon, the laser excitation needs a specific configuration to connect an optical fiber to the micromachined part of the actuator.

Piezoelectrically driven devices are suitable actuators for precise,

This chapter has been submitted for publication: [148]
Parts of this chapter are published in: [86], [149], [160].

high-speed displacement and positioning. The traditional piezo elements are miniature structures having dimensions in the range of millimeters to centimeters [138,139]. Their actuation voltages are relatively high, i.e. they lie between 100 and 200 V. Microfabricated actuators using piezoelectric thin films have been reported [140-143]. They require much smaller driving voltages, however, the technology for reproducible film deposition and their integration in microsystems are difficult tasks.

The electrostatic actuation is rather promising for surface-micromachined structures since electrostatic forces scale well into this micro domain. First, surface microactuators allow the distance between the drive electrodes to be reduced to one micron or less. Thus, even at low voltages ranging from 10 to 20 V, sufficiently large actuation forces can be generated. Second, extremely small values of the spring constant are obtained for such microstructures. Due to this high mechanical flexibility of the structures, large deflections are achieved at moderate driving forces. A further important advantage of the electrostatic drive is the very low power consumption.

Among electrostatically driven surface-micromachined actuators, free-standing polysilicon microstructures fabricated by sacrificial layer technology are favorable candidates [13,14,70,100,117,144-147]. Since polysilicon is a well-established material in IC technology (interconnection, gate-electrode), it can be directly used as a drive-electrode. Furthermore, polysilicon exhibits – similar to single crystal silicon – excellent mechanical properties, e.g. a high modulus of elasticity; in particular, no material fatigue has been observed so far (see also section 1.1.2).

In this chapter [148], two types of electrostatic polysilicon actuators are characterized with respect to low driving voltages and high reliability. The first actuator is a microbridge structure allowing deflection perpendicular to the substrate surface. The second actuator type consists of a rigid comb element which is supported by flexible suspension beams allowing thus horizontal displacement with respect to the substrate.

In the following section, an overview on the processing sequence is given and the device operation is described. Subsequently, the performance of both types of actuators is discussed in detail, i.e. simple analytical models are developed to examine, how the drive voltage can be lowered by controlled adjustment of the design parameters. In particular, the potential energy curve is calculated; thus, not only the displacement as a function of the drive voltage is obtained but also the stability conditions which lead to a better understanding of the functional behavior of the electromechanical microstructures. Furthermore, the validity of the modeling as well as the reliability of the structures are demonstrated by measurements carried out on prototype actuators.

Based on the analysis of the actuator structures, applications are presented using the two actuator types as drive elements: an electromechanical switch with separate driving and working circuit, an *xy* stage for fine-positioning e.g. of a micromachined atomic force microscope sensor head, and a microshutter for simple control of a laser beam in an optical system. Finally, the major results are summarized in the concluding section.

3.2 Fabrication and Operational Principles

The fabrication of the polysilicon microactuators is based on the sacrificial layer technology described in section 2.2. In addition, IC processing steps are employed, for instance doping of substrate regions and aluminum metallization for the bridge actuator [86]. The processing sequence of the latter structure is shown in Fig. 3.1.

As indicated in the final cross section of Fig. 3.1, one electrode of the capacitor-like actuator consists of the free-standing phosphorus-doped polysilicon beam, the counter-electrode is an underlying phosphorus-doped substrate region. By applying a voltage between the polysilicon and a substrate electrode, the resulting electrostatic force pulls the beam downwards. The displacement is given by the position where the drive force is balanced by the restoring spring force of the beam. Applying the switch voltage, the beam is deflected until touching the substrate. Due to the double passivation layer on the substrate surface (silicon dioxide and silicon nitride, see Fig. 3.1), the distance between the polysilicon and the substrate electrode does not become zero and the electrodes are not in electric contact when the beam is touching the substrate. Removing the applied voltage, the spring force returns the beam to its free-standing position. Thus, it is possible to distinguish two well-defined states: the undisturbed free-standing and the completely downward deflected (i.e. touching the substrate) microbridge. Hence this actuator type is suited for application as a switch device. The SEMs of Fig. 3.2 illustrate clearly the two electrostatically controlled states of a prototype beam switch.

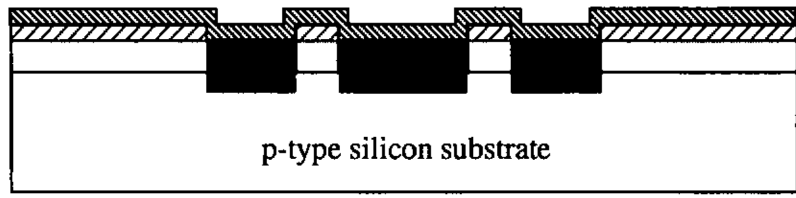

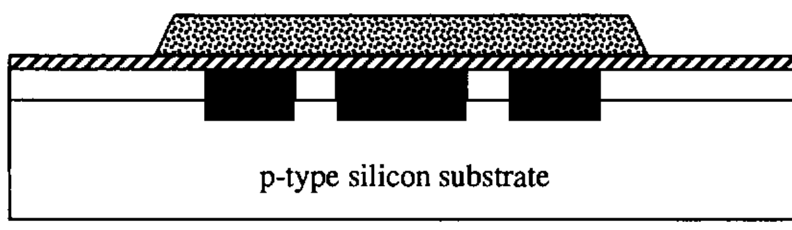

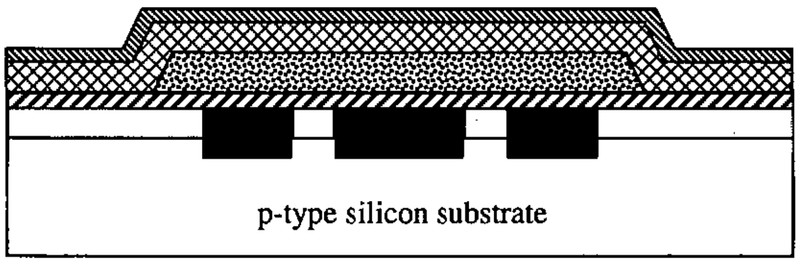

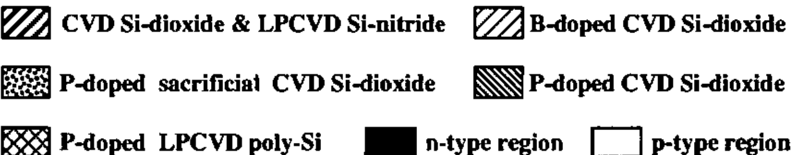

Fig. 3.1 Fabrication process of the polysilicon microbridge: definition of doped regions in the silicon substrate by diffusion from doped silicon dioxide films; passivation and protection of the substrate by a oxide/nitride double layer; deposition and patterning of the sacrificial oxide; deposition of polysilicon and of P-doped oxide; doping by diffusion and annealing of the polysilicon.

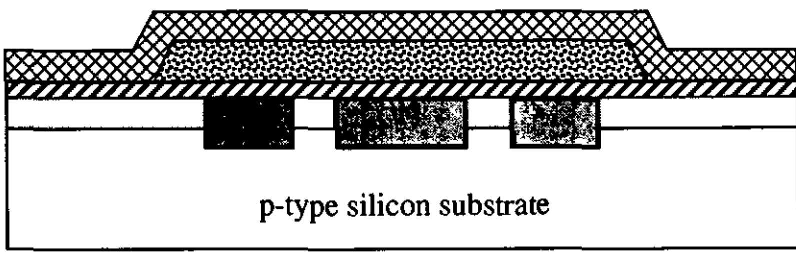

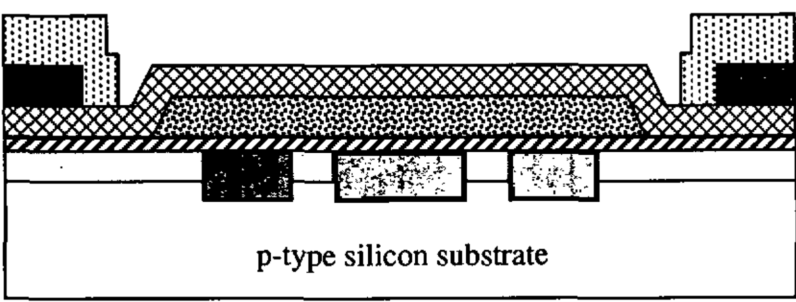

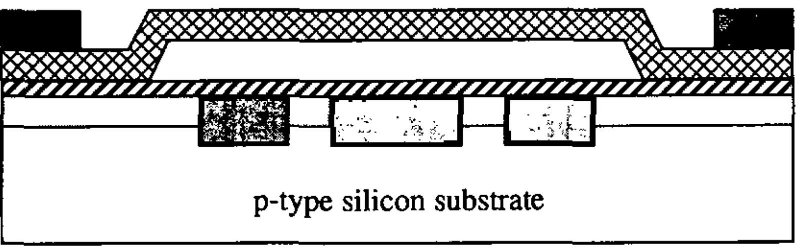

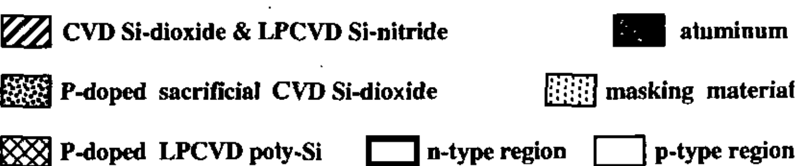

Fig. 3.1 *(continued)* Fabrication process of the polysilicon microbridge: removal of the P-doped oxide and patterning of the polysilicon; evaporation and patterning of aluminum; photoresist pattern for exposing the sacrificial oxide and protecting the remaining part of the surface (e.g. aluminum pads); lateral etching of the sacrificial oxide to obtain the free-standing polysilicon structures.

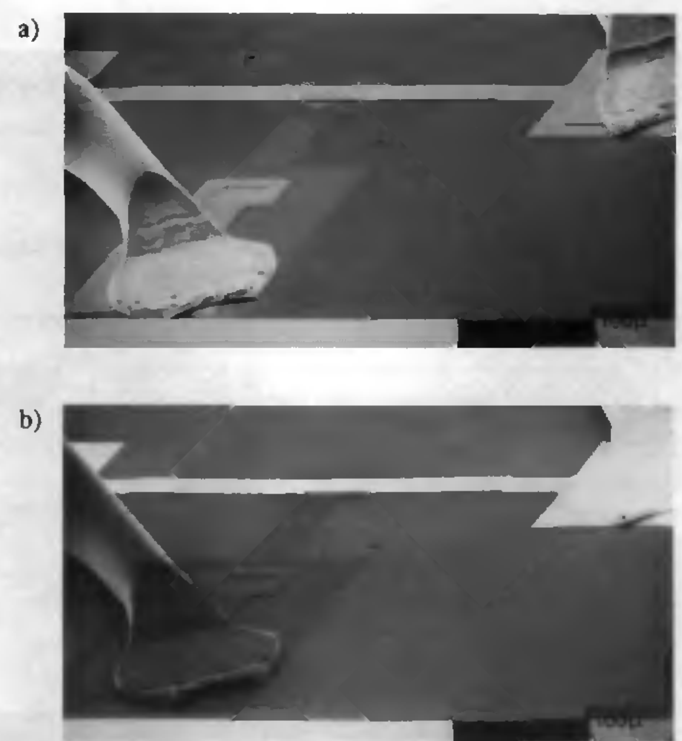

Fig. 3.2 SEM micrographs showing the two switch states of a wire-bonded standard polysilicon microbridge (300 µm long, 25 µm wide and 1 µm thick): (a) the free-standing beam and the substrate electrode are on the same electric potential; (b) 14 V are applied between the completely downward deflected beam and the substrate.

The SEM of Fig. 3.3 shows a polysilicon comb actuator [149] consisting of a pair of electrostatic interdigitated combs, namely the fixed and the movable finger beam electrodes. The latter are suspended by long folded cantilever beams which are anchored at their ends to the substrate. These suspension beams permit lateral motion (in finger direction), i.e. they provide high flexibility for lateral displacement and large stiffness perpendicular to the finger direction. The lateral driving forces are produced by applying a voltage between the fixed and the movable electrodes. The electrostatic force between just one fixed and one movable finger electrode (i.e. one finger capacitor) is relatively weak, since it is proportional to the electrode surface area which is given by the finger thickness times the overlapping finger length. A number of such finger

capacitors are connected in parallel in the interdigitated combs. Hence the total drive force equals the sum of the forces of all finger capacitors.

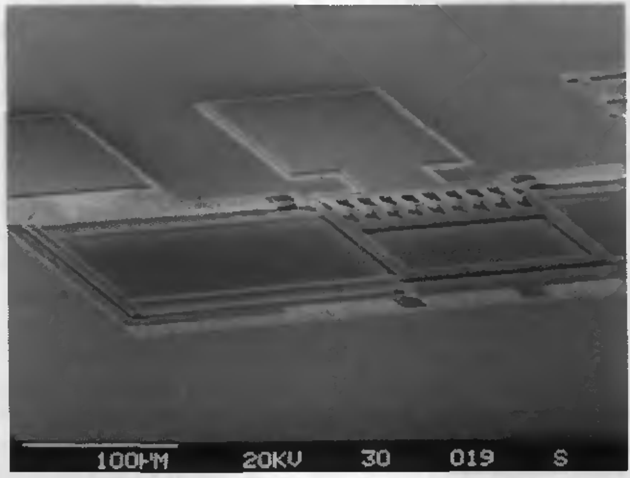

Fig. 3.3 SEM view of a standard polysilicon comb actuator; the interdigitated combs (18 finger capacitors) and one half of the suspension beam system (l = 200 µm, b = 0.6 µm and h = 2 µm) can be seen.

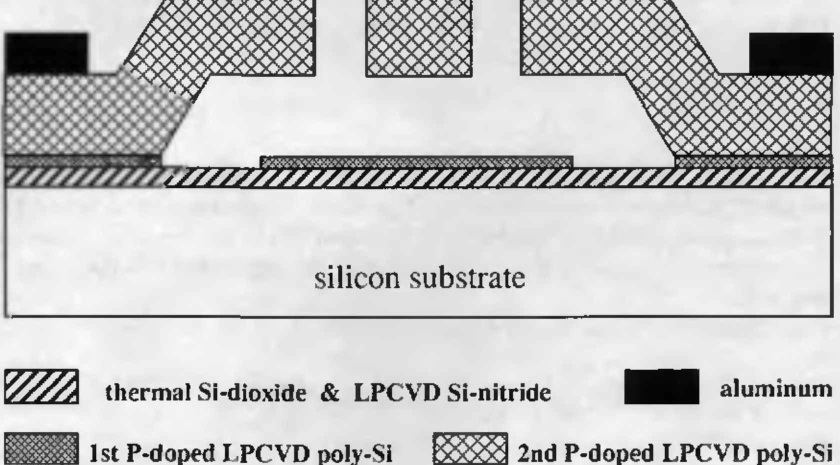

Fig. 3.4 Schematic cross section of the interdigitated combs.

Figure 3.4 shows a simplified cross section of the comb part of the actuator. The ground plate underneath the interdigitated combs is held at the same potential as the movable comb in order to avoid electrostatic attraction and sticking to the substrate. A thin polysilicon layer instead of a doped region in the substrate has been chosen as ground plate, thus allowing high operation voltages. Except for this difference, the fabrication process of the comb actuator is rather similar to that of the bridge actuator shown in Fig. 3.1; the detailed processing sequence is published elsewhere [150].

3.3 Theoretical and Experimental Device Performance

3.3.1 Bridge Actuator

First, analytical modeling of the actuator including the investigation of the potential energy is performed. For the one-dimensional motion of the center of the polysilicon microbridge, we take the z-axis perpendicular to the substrate surface, the positive direction of the z-axis to be downward and $z = 0$ as the free-standing (undeflected) position of the beam. Two conservative forces determine the potential energy curve $U(z)$ of the bridge. On the one hand, the electrostatic driving force F_{elstat} acts in the positive z direction. On the other hand, the restoring spring force F_{spring} exerted on the deflected beam is in the negative z direction, i.e. $F_{spring}(z) = -kz$, where k is the spring constant or stiffness of the microbridge.

For deflection of beams with different boundary conditions the following general expression is found for the stiffness [e.g. 131,151]:

$$k = \frac{nEI}{l^3} \tag{1}$$

where n is a constant determined by the boundary conditions, l is the length of the beam, E denotes the modulus of elasticity (see also section 1.1.2 & 2.2.2) assumed to be 170 GPa for polysilicon [86,152,], $I = bh^3/12$ denotes the moment of inertia of the cross section of the beam that has thickness h and width b.

Thus the potential energy due to the stiffness of the beam is:

$$U_{spring}(z) = -\int F_{spring}(z)\,dz = {}^1/_2\,\frac{nEbh^3}{12l^3}\,z^2\,. \tag{2}$$

Applying the model of the parallel-plate capacitor, the force $F_{elstat}(z)$ on the polysilicon beam electrode can be approximated as follows [e.g. 153]:

$$F_{elstat}(z) = {}^1/_2\, \varepsilon_0 \varepsilon \frac{A}{(d-z)^2} V^2 \tag{3}$$

where V and $(d-z)$ denote the drive voltage and the distance between the polysilicon and the substrate electrode, A the area of the electrode that equals the area of the diffusion region in the substrate, $\varepsilon_0 = 8.85 \times 10^{-12}$ As/Vm is the permittivity in vacuum and $\varepsilon = 1.3$ is a fitted dielectric constant that includes the air-gap and the double passivation layer [86].

The total potential energy of the beam actuator can finally be written as:

$$\begin{aligned} U_{tot}(z) &= U_{elstat}(z) + U_{spring}(z) \\ &= -{}^1/_2\, \varepsilon_0 \varepsilon \frac{A}{d-z} V^2 + {}^1/_2 \frac{nEbh^3}{12l^3} z^2. \end{aligned} \tag{4}$$

Calculation of the potential energy curve by means of the above modeling was carried out for the structure of Fig. 3.2, i.e. the standard polysilicon microbridge with $l = 300$ µm, $b = 25$ µm and $h = 1$ µm. The air-gap distance between the free-standing (i.e. undeflected) bridge and the substrate surface is 1.2 µm; thus, d from eq. (3) which includes also the double passivation layer thickness becomes 1.67 µm (see Fig. 3.1). When using for actuation only the middle one of the three substrate electrodes that are sketched in Fig. 3.1 (A equals then 25 µm x 80 µm), the driving force can be approximated as concentrated load at the center of the beam which has both ends fixed. Thus, n of eq. (1) equals 192 and the stiffness becomes 2.52 N/m. By employing finite-element modeling (using ANSYS) we compared the step-up boundary conditions of the real microbridge with the idealized doubly clamped beam (a detailed analysis of the mechanical behavior of step-up boundary conditions is given by Mullen et al. [154]). Applying a force of 1 µN to the standard polysilicon bridge, the simulation program results in a deflection of 0.385 µm corresponding to a spring constant of 2.6 N/m. Hence we found no significant difference between the analytical and the simulated value of the microbridge stiffness.

Fig. 3.5 shows the two components $U_{spring}(z)$ and $U_{elstat}(z)$ as well as the total potential energy $U_{tot}(z)$ that are obtained from eq. (4), when the driving voltage $V = 9$ V is applied to the standard bridge. As indicated in the graph, the two opposite forces which determine $U_{tot}(z)$ generate two positions of static equilibrium: a stable equilibrium with a minimum of the potential energy at $z = z_s$ and an unstable one with a maximum at $z = z_{us}$. Thus, if the microbridge is at rest at its free-standing position and the

voltage V is applied, it is deflected to the minimum of the potential energy at $z = z_S$.

In Fig. 3.6 the total potential energy of the standard microbridge as a function of the deflection is plotted for different drive voltages using eq. (4). It is indicated that with increasing actuation voltage the two equilibrium positions z_S and z_{us} approach each other, and at the same time the energy barrier of the unstable equilibrium decreases relatively to the potential energy minimum. At a certain threshold voltage $V = V_t$, the two equilibrium positions finally converge at $z = z_t$. For $V = V_t$ the potential energy is almost constant within a certain interval around the position z_t. This interval can be approximated as neutral equilibrium region where the resultant force exerted on the beam can be neglected. SEM-observations confirmed this assumption: the deflected beam "trembled" (probably due to small parasitic forces) over a small z-interval when V_t was applied. For drive voltages greater than V_t, no more equilibrium position is observed in Fig. 3.6, i.e. for increasing z the total potential energy constantly decreases. This means that the electrostatic force can not be balanced any more by the restoring spring force over the whole of the distance between the polysilicon and the substrate electrode. As a consequence the microbridge is deflected until touching the substrate. Hence switching occurs for voltages beyond V_t.

For a drive voltage $V = 14$ V, Fig. 3.6 shows that the beam will be switched downward, i.e. it will touch the substrate with $z = 1.2$ µm (equal to the air-gap distance of the undeflected bridge structure). If subsequently the voltage is reduced to 7.5 V, the corresponding position z_{us} of the potential energy maximum lies beyond that air-gap distance (see Fig. 3.6), since the overall interelectrode distance includes also the double passivation layer in addition to the air-gap. As a consequence, the beam will switch upward to the corresponding minimum position $z = z_S = 0.1$ µm (for 7.5 V) which is very close to the free-standing position. Thus, the net voltage difference for switching the standard microbridge can be reduced to 6.5 V.

The investigation of the potential energy curve provides information on the displacements (equilibrium positions) as well as on the stability and switching conditions of the electromechanical bridge actuator. If only the displacement as a function of the drive voltage is needed, it can be mathematically found by equating the derivative of the potential energy of eq. (4) to zero (force equation for static equilibrium):

$$0 = \frac{dU_{tot}(z)}{dz} = {}^1\!/_2\, \varepsilon_0 \varepsilon \frac{A}{(d-z)^2} V^2 - \frac{16Ebh^3}{l^3} z \ . \qquad (5)$$

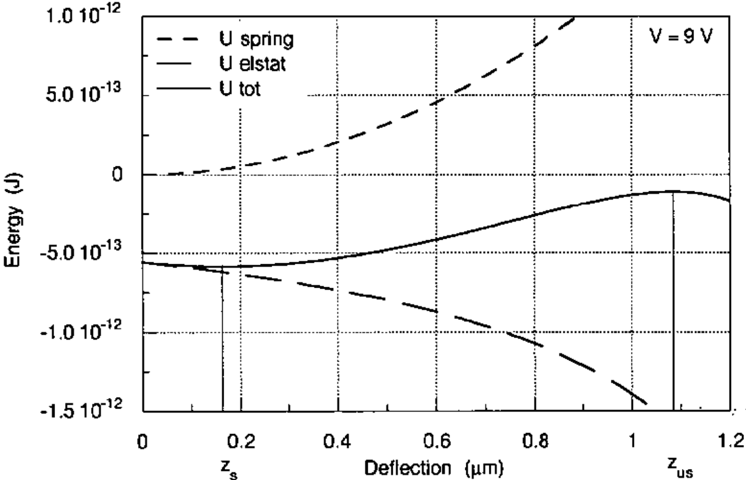

Fig. 3.5 The total potential energy and its two components versus the deflection of the standard bridge actuator for a drive voltage of 9 V. The curves are calculated using eq. (4). A stable and an unstable equilibrium exist corresponding to a minimum of the total potential energy at z_S and a maximum at z_{US}, respectively.

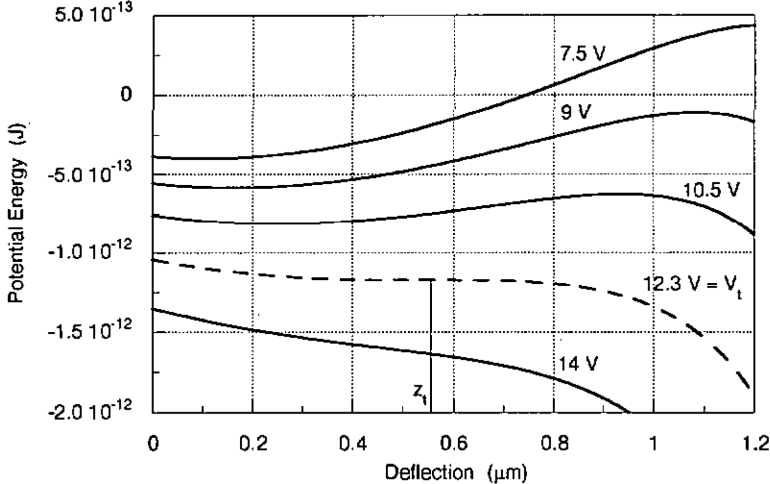

Fig. 3.6 The potential energy of the standard bridge actuator as a function of the deflection for various driving voltages, calculated using eq. (4). The stable and the unstable equilibrium converge for V_f; for voltages larger than V_f the microbridge deflects completely downwards until touching the substrate.

In view of the application as switch device, the threshold voltage V_t has to be known for the microbridge. As illustrated in the potential energy curves of Fig. 3.6, the position $z = z_t$ is given by setting the second derivative of the potential energy equal to zero:

$$0 = \frac{d^2U_{tot}(z)}{dz^2} = \varepsilon_0\varepsilon \frac{A}{(d-z)^3} V^2 - \frac{16Ebh^3}{l^3} . \tag{6}$$

Solving eq. (6) for V^2 and substituting the result in eq. (5) yields the following simple analytical expressions that have first been used by Nathanson et al. [81]:

$$z_t = {}^1/_3\, d \qquad \text{and} \qquad V_t = \sqrt{\frac{128}{27}\frac{Ebh^3}{l^3}\frac{d^3}{\varepsilon_0\varepsilon A}} . \tag{7}$$

The simple formulae of eqs. (7) are only obtained in the case of the microbridge; for (large) displacements of the comb structures such analytical solutions are not possible any more (see Section 3.3.2). In the following, parameter adjustment is discussed with regard to low driving voltages and high reliability, based on eqs. (7) and on measurements on prototype structures.

As indicated in the square root of V_t in eqs. (7), low switch voltages are obtained by adjusting the geometric dimensions for a low beam stiffness and a large electrostatic drive force, corresponding to the middle and the last term of the square root, respectively. For technological (e.g. sticking problem) as well as for functional reasons (e.g. two well-separated switch positions), the distance d between the electrodes has to be greater than 1.5 µm and the beam thickness h at least 1 µm. The remaining two parameters in the square root for V_t are the beam length l and the electrode area A (the beam width b is already contained in A). Table 3.1 lists measured and calculated switch voltages of polysilicon microbridges for different magnitudes of these two parameters. The measurements were performed in SEM and the V_t values were taken as the calculated switch voltages.

For the standard microbridge structure (l = 300 µm, A = 25 µm x 80 µm), V_t = 12.3 V has been calculated whereas the measurement gave 14 ± 0.5 V. The difference between theoretical and experimental data is mainly due to the simple modeling (e.g. parallel-plate capacitor). The error of the measured values is mainly caused by variations in geometric dimensions (e.g. film thicknesses) for identical structures on different chips or wafers (prototype level).

Comparison of the standard structure with a microbridge that has shorter beam length (240 µm) including also a slightly smaller electrode area

Table 3.1 Measured and calculated switch voltages of polysilicon microbridges for different design parameters.

Beam Length (μm)	Electrode Area (μm^2)	Switch Voltage (V) Measured	Switch Voltage (V) Calculated V_t
240	1500	22.5±1	19.8
300	2000	14±0.5	12.3
300	4750	12±0.5	11.3

resulted in a much higher switch voltage as expected from the model. If the beam length is increased to more than 400 μm, the microbridge sometimes stays sticking to the substrate also after removal of the switch voltage. Since the stiffness of the beam substantially decreases for increasing beam length, the restoring spring force might become too weak to overcome the strong electrostatic forces which are generated by hydrogen bonds and/or by opposite charges (dipole-like) between the polysilicon and the substrate electrode during downward switching (see also section 2.2.3).

To increase the electrode area of the 300 μm long bridge actuator, the two outer substrate electrodes were connected in parallel to the middle electrode (see Fig. 3.1). However, as shown in Table 3.1, the switching voltages could not be considerably reduced, since the additional forces were located towards the ends of the bridge structure where they had to overcome a much bigger beam stiffness than the force at the beam center. For calculation of the stiffness when using the three substrate electrodes, a uniformly distributed force on the entire beam was assumed (n in eq. (1) becomes then 384). A good agreement between theoretical and experimental data was found in that case.

3.3.2 Comb Actuator

For the horizontal motion of the comb actuator, we take the x-axis in direction of the finger beams. As in the case of the microbridge, the electrostatic drive force and the restoring spring force determine the displacement. If the displacement is small compared to the comb configuration, i.e. if the front ends of the fingers of one comb do not come very close to the "spine" of the opposite comb, the electrostatic force $F_{elstat}(x)$ can be approximated by taking only the lateral electrostatic forces produced in the finger capacitors into consideration and by neglecting fringing effects. The lateral driving forces, which provide motion parallel to the electrode surface of the capacitors, are constant and hence do not depend on the displacement [e.g. 153]. The total driving force created in the interdigitated combs becomes then:

$$F_{elstat}(x) = {}^1\!/_2\, p\, \varepsilon_0 \frac{h}{d} V^2 \qquad (8)$$

where p is the number of finger capacitors, V and d denote the drive voltage and the distance (perpendicular to the x-axis) between the movable and the fixed finger beams, h the beam thickness. Since the dieletric material consists mainly of air (plus very thin layers of native oxide), its permittivity is approximated by ε_0.

By applying eq. (1) to the suspension beam system with its boundary conditions, the stiffness k in x direction of the comb actuator shown in Fig. 3.3 can be approximated. This approximation assumes that the stiffness remains constant for the (large) horizontal deflections of the suspension beams; n of eq. (1) becomes then 24 [e.g. 14] and l denotes the length of a beam element two of which form a folded suspension cantilever beam. For horizontal deflection, the moment of inertia is defined as $I = hb^3/12$ where b is the suspension beam width. Thus, the stiffness of the suspension can be written as:

$$k = \frac{2Ehb^3}{l^3} \ . \qquad (9)$$

Since the driving force of eq. (8) does not depend on x, the force equation can be used to obtain a simple expression for (small) displacements, i.e. the static equilibrium positions of the comb actuator as a function of the applied voltage. In contrast to the force equation (5) of the microbridge which is a third-degree polynomial in the displacement, a linear equation in x is found for the comb actuator:

$$x = {}^1\!/_4\, p\, \varepsilon_0 \frac{1}{E} \frac{l^3}{b^3} \frac{1}{d} V^2 \ . \qquad (10)$$

Eq. (10) predicts that several design parameters allow a reduction of the drive voltage of the comb actuator for a given displacement. Changes in l and b correspond to variations in the flexibility of the suspension, changes in d and p modify the electrostatic drive force. The influence of these parameters was also tested experimentically. As standard comb actuator for the measurements, the structure of Fig. 3.3 was used. The dimensions of its suspensions are: l = 200 µm, b = 0.6 µm and h = 2 µm. The number of finger capacitors is p = 18. The interelectrode distance measures d = 3.4 µm. Compared to the bridge structure with h = 1 µm, the polysilicon beam thickness is increased to h = 2 µm for the comb actuators (as indicated in eq. (10), h does not influence the displacement/voltage characteristics). Hence a

high stiffness perpendicular to the substrate surface is achieved which reduces sticking effects of the movable comb part to the substrate and thus improves the device reliability.

A particular feature of the standard comb structure is that the suspension beam width b is less than one micron (see also section 2.3, Fig. 2.15). This results in an extremly small suspension stiffness (eq. (9) yields k = 18 mN/m) and hence in rather low driving voltages. The graph of Fig. 3.7 shows the measured displacement as a function of the drive voltage for the standard comb actuator as well as for another comb structure with the same dimensions except for a larger suspension beam width b = 2.6 μm. For the latter structure the displacement was limited to about 2.5 μm by voltage breakdown that occurred between 200 V and 250 V. To achieve the same displacements with the standard actuator having b = 0.6 μm, a significant reduction of the drive voltage of almost one order of magnitude was measured which fits well to the modeling of eq. (10). Errors of ±0.4 μm were assumed for the visual measurements.

As further indicated in eq. (10), a large reduction of the drive voltage is achieved by decreasing the distance d. Hirano et al. [13] have realized comb actuators with interelectrode distances in the submicron range. Applying only 11.1 V, they measured a displacement of 3.6 μm. As in the case of small suspension beam widths, special fabrication techniques are necessary to obtain such small values of d. For our standard comb structure the interelectrode distance is relatively great (3.4 μm), and a reduction to about 2 μm is possible without special technological means.

The graph of Fig. 3.8 illustrates the measured displacement as a function of the applied voltage for three different comb structures. The standard comb actuator is compared to a second structure with the same dimensions except for a bigger suspension beam length l and a third actuator with p increased from 18 to 34. As predicted by eq. (10), Fig. 3.8 shows that, e.g. by applying 20 V, the displacement is increased from 1.25 μm to 2.9 μm when the number of finger capacitors is raised, and, in particular, to 5.85 μm when l is increased from 200 μm to 300 μm. For a suspension length l larger than 300 μm, the free-standing comb structure often fails by sticking to the substrate (the overall length of the movable part of the actuator is more than twice the magnitude of l).

The maximum displacements in the measurements were always limited by front sticking, i.e. for increasing displacement the front ends of the fingers of one comb approached the "spine" of the opposite comb until at a certain threshold voltage $V = V_t$ the interdigitated combs abruptly snapped together in actuation direction. On the other hand, mainly for two reasons the comb actuators used here did not show side sticking where the movable fingers stick to the fixed fingers by moving perpendicular to the finger direction (a detailed analysis of side-sticking is given elsewhere [13,150]):

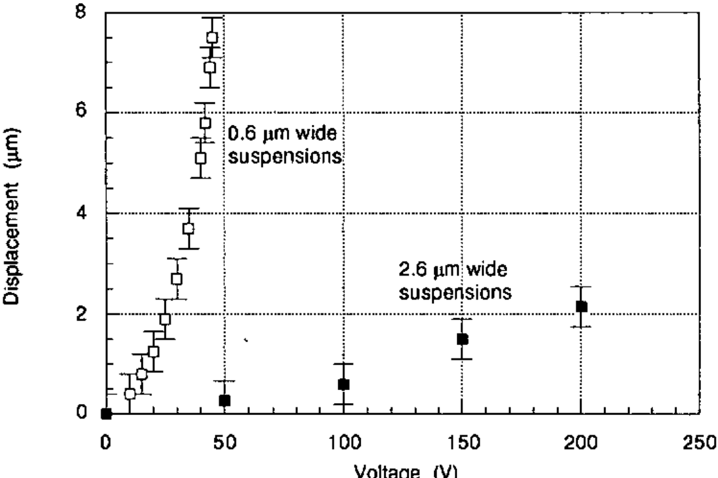

Fig. 3.7 The measured displacement versus applied voltage characteristics shows that the standard comb actuator needs a much lower driving voltage than the other actuator with the same dimensions except for a greater suspension beam width $b = 2.6$ µm.

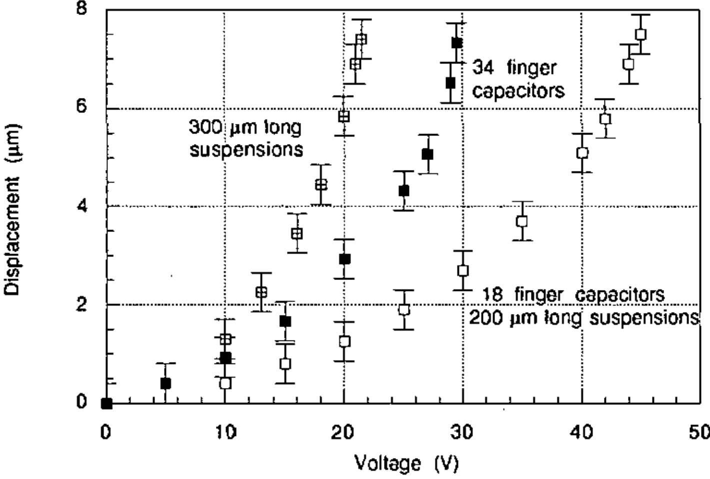

Fig. 3.8 Measured displacement versus applied voltage; the standard comb actuator is compared to a second actuator having more finger capacitors and a third one with longer suspension beams. The reduction of the driving voltage by controlled adjusting of the design parameters agrees well with the simple modeling of eq. (10).

first, the large stiffness of the suspensions perpendicular to the finger direction [149] and second, the relatively big interelectrode distance which impedes large electrostatic forces in that direction.

The model of eq. (10) gives no information on the onset of front sticking, i.e. the maximum possible displacement which is an essential parameter in view of applying the comb actuator for positioning. In addition, a growing difference between measurement and calculation based on eq. (10) is observed when x approaches this maximum displacement. Therefore, a refined model is used which takes also into account the capacitances between the front ends of the finger beams and the "spine" of the opposite comb by adding a second term to the electrostatic drive force of eq. (8). This second term is again approximated by applying the parallel-plate capacitor model and has the same form as the force of eq. (3). Thus, taking $x = 0$ as the undisplaced position of the front ends of the finger beams, the total electrostatic drive force of the comb actuator is given by:

$$F_{elstat}(x) = {}^1/_2\, p\, \varepsilon_0 \frac{h}{d} V^2 + {}^1/_2\, q\, \varepsilon_0 \frac{Bh}{(D-x)^2} V^2 \qquad (11)$$

where q is the number of finger front capacitors, B is the finger beam width and D denotes the initial distance between the front end of the fingers and the "spine" of the opposite comb.

As in the case of the microbridge, it is useful to look at the potential energy of the comb actuator which can be derived from eqs. (9) and (11):

$$\begin{aligned} U_{tot}(x) &= U_{elstat}(x) + U_{spring}(x) \qquad (12) \\ &= -{}^1/_2 p\varepsilon_0 \frac{(L+x)h}{d} V^2 - {}^1/_2 q\varepsilon_0 \frac{Bh}{D-x} V^2 + {}^1/_2 \frac{2Ehb^3}{l^3} x^2 \end{aligned}$$

where L denotes the initial overlap length of the movable and the fixed fingers in x direction. For the standard comb structure $L = 10$ µm, $D = 15$ µm, $B = 5$ µm and $q = 17$.

By applying eq. (12), the graphs of Figs. 3.9 and 3.10 illustrate the potential energy of the standard comb actuator as a function of the displacement; Fig. 3.9 shows the total potential energy and its components for a drive voltage of 30 V, Fig. 3.10 shows the total energy for various drive voltages. In spite of the additional term due to the lateral drive force, the behavior of the energy curves of the comb actuator is similar to that of the microbridge actuator: for small voltages a stable and an unstable equilibrium exist. Beyond the threshold voltage V_t, the movable fingers are abruptly displaced until touching the fixed comb, i.e. front sticking occurs.

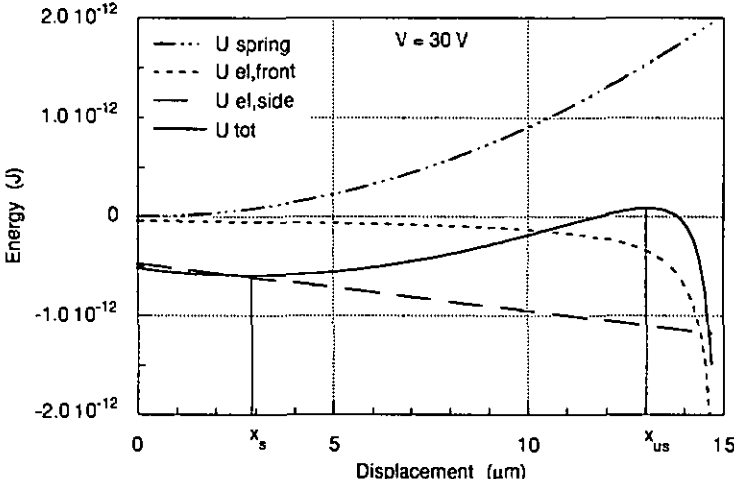

Fig. 3.9 The total potential energy and its three components versus the displacement of the standard comb actuator for a drive voltage of 30 V. The curves are calculated using eq. (12). As in the case of the bridge actuator, a stable (minimum of the total potential energy at x_S) and an unstable (maximum at x_{US}) equilibrium exist.

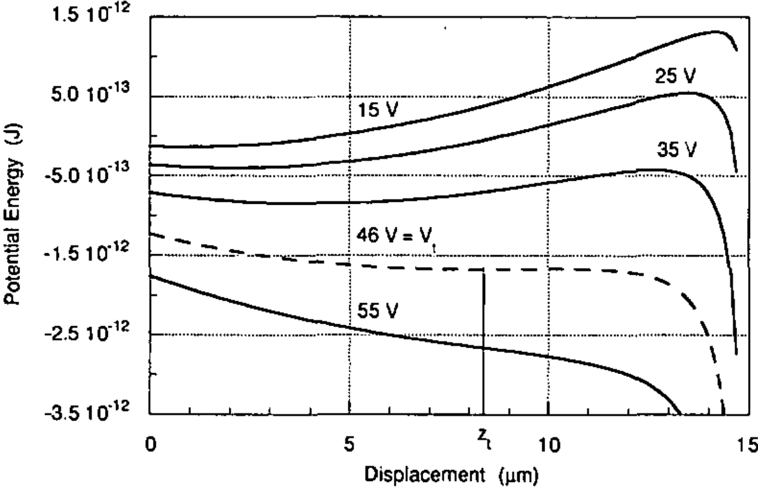

Fig. 3.10 The potential energy of the standard comb actuator as a function of the displacement for various driving voltages, calculated using eq. (12). The curves are similar to those of the bridge actuator; for voltages larger than V_t front sticking of the interdigitated combs occurs.

A comparison of theoretical data based on eq. (12) with measurements is given in Fig. 3.11. The graph shows the displacement as a function of the drive voltage for the standard comb structure and for a second actuator with the same dimensions except for a greater l = 300 μm. Modeling and measurement of the latter structure agree well, if a suspension beam width b = 0.55 μm instead of 0.6 μm is taken, resulting in a stiffness k = 4.2 mN/m from eq. (9) instead of k = 5.5 mN/m. Such differences in b lie within the undercut uniformity of the RIE step for the high aspect ratio polysilicon structures (see also section 2.3.1).

As illustrated in Fig. 3.11, the analytical modeling predicts rather well the measured displacements. The small differences in V_t can be explained by additional inhomogenous electric fields, e.g. at the corners of the front ends of the fingers. By using the parallel-plate capacitor model, only homogenous fields have been considered, and hence the calculated electrostatic driving forces are too small. On the other hand, if inhomogenous fields are taken into account, no simple analytical solution can be found.

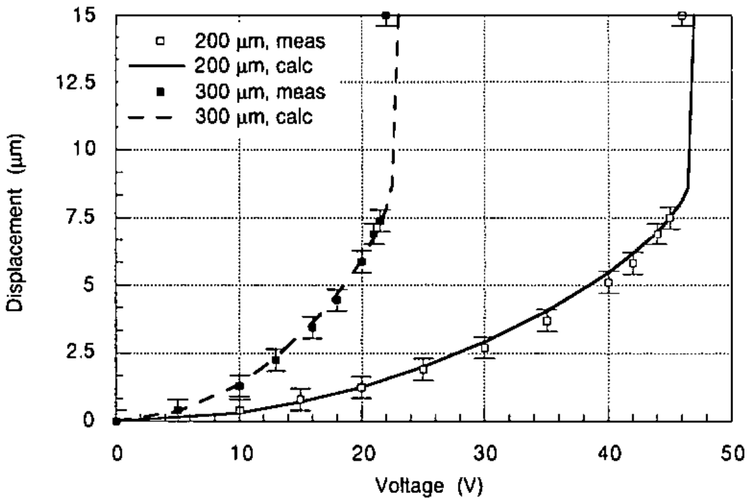

Fig. 3.11 Measured and calculated displacement versus drive voltage of two comb actuators having suspension beam lengths of 200 μm (standard structure) and 300 μm, respectively. The simple analytical modeling based on eq. (12) agrees well with the experiments.

As in the case of the microbridge, a pure mathematical description is also possible for the determination of V_t and the corresponding maximum displacement x_t of the comb actuator by setting the first and the second derivative of $U_{tot}(x)$ of eq. (12) equal to zero:

$$0 = x_t^3 + 3Dx_t^2 - (3D^2+3\frac{q}{p}Bd)x_t + D^3+D\frac{q}{p}Bd \qquad \text{and}$$

$$V_t = \sqrt{\frac{2Ehb^3}{l^3}\frac{(D-x_t)^3}{q\varepsilon_0 Bh}} \tag{13}$$

The third-degree polynomial in x_t of eqs. (13) has coefficients which depend only on the geometric dimensions of the capacitors. Thus, as for z_t of the microbridge, the maximum displacement of the comb actuator is a function of the design of the drive capacitors only and does not depend on the suspension stiffness k. This is also confirmed by the measurements of Fig. 3.11, where the two comb actuators which vary only in k (different suspension beam length) show the same maximum displacement of about 7.5 μm before the onset of front sticking. The analytical solutions for x_t and V_t of eqs. (13) are rather complex; on the other hand, the investigation of the potential energy curve for various drive voltages provides an illustrative graphic approximation for V_t and x_t which can be directly used to optimize the design of the actuator.

3.4 Applications

3.4.1 Electromechanical Microswitch

Switch devices fabricated by micromachining techniques are of great interest since they may fill the gap between the well-established transistor-based switches and the traditional electromagnetic relays [155-157]. By extending the processing sequence of the capacitive polysilicon microbridge shown in Fig. 3.1, an IC-compatible electromechanical switch can be realized.

Figure 3.12 shows a cross section of such an electrostatically-driven mechanical relay. For insulation of the driving and the working circuit, the microbridge consists of three layers, similar to beam structures that have been used elsewhere [158]. The upper polysilicon layer of the beam of Fig. 3.12 serves for driving, while the lower polysilicon is used as one contact electrode in the working circuit. Both polysilicon layers are phosphorus-doped and insulated by a sandwiched silicon nitride film. An additional polysilicon lane on the substrate which leads underneath the free-standing

beam structure is taken as second contact electrode of the working circuit, while the counter-electrode of the drive circuit consists of a large substrate diffusion region.

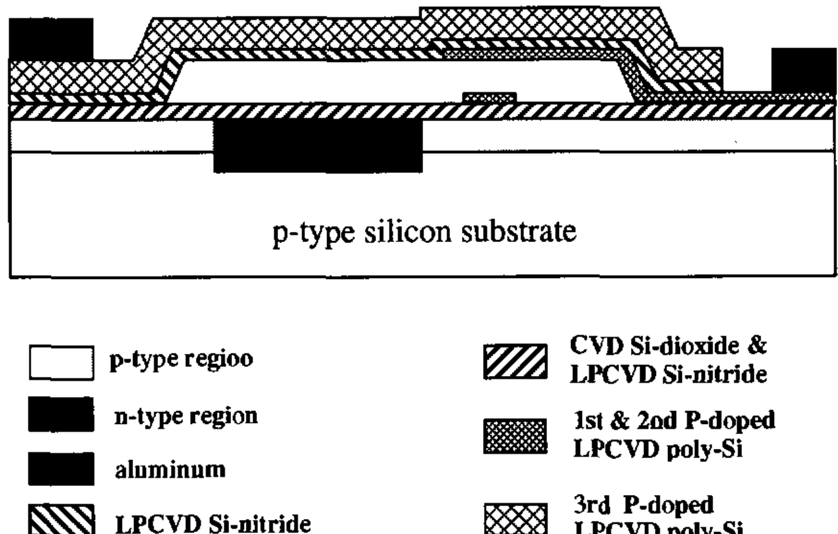

Fig. 3.12 Schematic cross section of an electromechanical microbridge-based polysilicon relay.

A special feature of this electromechanical microrelay is the air-gap between the two contacts of the working circuit which provides a very high off-state impedance and no leakage currents in the off-condition. Special attention has to be paid to the contact resistance in order to avoid soldering in the closed state – low-current application is preferable. A further advantage of the relay is the low switching voltage obtained by an optimum design of the drive-capacitor as discussed in section 3.3.1. Such low driving voltages of about 10 V are promising for applications where the microswitch is combined with IC elements that work in the same voltage range.

3.4.2 XY Microstage

Comb actuators enable relatively large and precise horizontal displacements and thus are well suited for driving an *xy* microstage [149]. The SEM of Fig. 3.13 shows such a fabricated polysilicon *xy* translator which is actuated by four standard comb elements. The small center table suspended by four beams (270 μm long, 0.6 μm wide and 2 μm thick) can be positioned in any direction in the *xy* plane (parallel to the substrate surface)

using two of the actuator elements. For voltages of about 50 V the center table could be moved up to 5 μm in the direction of each of the actuators.

Finite-element modeling using ANSYS demonstrates that the coupling between the displacements in x and in y direction is negligible. For the xy stage of Fig. 3.13, the simulation shows that a displacement of up to 5 μm in x direction results in a relative change in the y position of the order of 1 %. Thus, over the scan area of 10 μm x 10 μm, the coupling causes a maximum change of about (50 nm, 50 nm) in the (x,y) position.

Possible applications of these xy translators lie in the field of scanning and positioning units for micromachines. The microstages can be utilized for fine-positioning, while coarse-positioning is performed by traditional elements (e.g. piezostacks). In particular, the combination of surface and bulk micromachining (see section 2.4) has led to the fabrication of a silicon comb-drive xy micromanipulator with integrated sharp protuding tip on the center table for use in an atomic force microscope [123,124]. Miniaturization of such surface profiling systems is advantageous since the latter become then less influenced by thermal noise and external vibrations and thus achieve higher resolution.

3.4.3 Optical Microshutter

For torsional mirrors used as light modulators [e.g. 159], the on and off condition are determined by the reflection angle of the laser beam. This requires a setup for precise angular alignment of the signal readout. In order to avoid such additional optical tools, comb-driven shutters have been realized which allow a simple control of the laser beam in one direction and thus are promising for integration in optical systems.

The SEM of Fig. 3.14 shows a fabricated polysilicon microshutter [160]. The shutter plate is attached to the movable comb that is suspended by a meander-shaped double beam. The latter provides a substantial size reduction of the suspension element compared to traditional comb actuators (see Fig. 3.3), favouring thus the application in light modulator arrays. The flexibility of the meander suspension in actuation direction is only slightly smaller than that of the standard suspension, whereas the transverse stiffness is somewhat reduced lowering thereby the threshold voltage for side sticking. By applying 50 V to the structure of Fig. 3.14, an 8 μm displacement is observed; hence it is possible to modulate a laser beam having a diameter of up to 6 μm.

The optical microshutter can be operated in two different modes. In the reflection mode, the laser beam is either reflected by a highly reflective aluminum film on top of the shutter plate (on condition) or, for the displaced shutter, the beam is mainly absorbed by the underlying substrate surface which exhibits only poor reflection (off condition). In the transmission mode

[e.g. 161], the closed state is given by the interruption of the laser beam - the latter is stopped by the shutter plate. In the open state, i.e. for the displaced shutter, the beam can pass a via hole that has been KOH-etched from the backside of the silicon substrate.

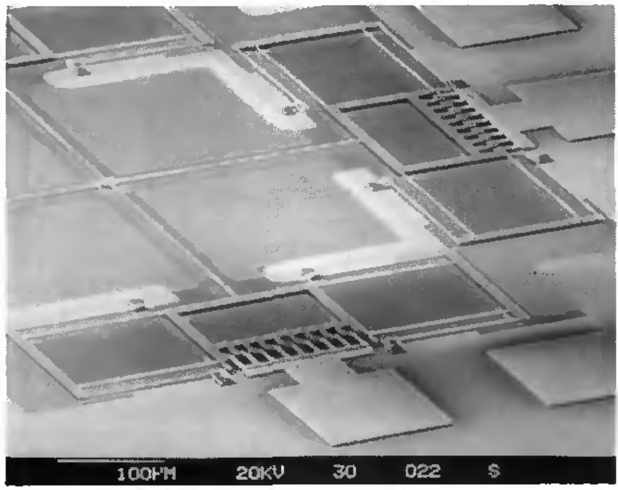

Fig. 3.13 SEM of one part of a polysilicon *xy* microstage driven by four standard comb actuators. The small center table is suspended by four 270 μm long beams.

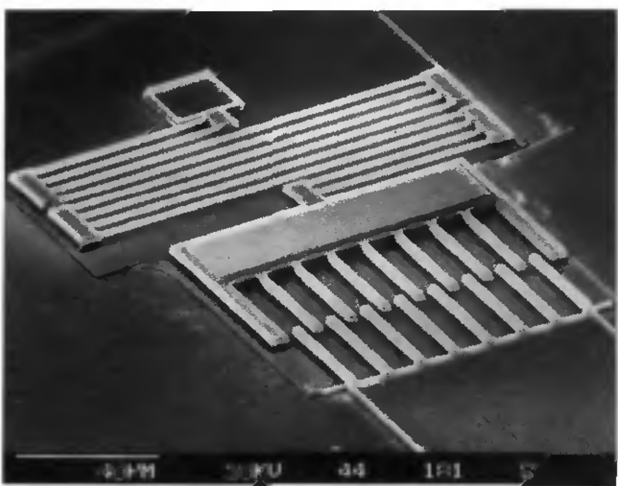

Fig. 3.14 SEM micrograph showing an polysilicon microshutter. The shutter plate is connected to the movable comb. The length of a beam element of the meander-shaped suspension system measures only 120 μm.

3.5 Conclusion

Electrostatically driven micromechanical polysilicon actuators have been characterized. Special attention has been paid to low driving voltages and high reliability. By analytical modeling the influence of the design parameters on the characteristics of the actuators has been examined. Measurements on prototype structures have demonstrated that the simple electromechanical models predict rather well the behavior of the actuators. For instance, a high flexibility and thus low drive voltages are achieved for a 1 μm thick and 300 μm long microbridge structure with vertical deflection (switch voltage 11 V), or for a comb actuator with four 0.6 μm wide and 600 μm long folded suspension beams. By applying only 20 V, a 5.9 μm displacement has been measured for that comb structure. Further possibilities for achieving low actuation voltages are large electrode surfaces and/or small interelectrode distances which, however, are limited by the sticking behavior of the devices.

The potential energy curves have been investigated in order to obtain more information on the functional behavior of the electromechanical actuators. In particular, a stable and an unstable equilibrium for small drive voltages are found for both, the microbridge and the comb actuator. By increasing the drive voltage, a threshold is reached beyond which the electrostatic force can not be balanced any more by the restoring spring force, and as a consequence the movable electrode sticks to the fixed electrode of the actuator. Thus, the potential energy model also indicates the switch voltage of the microbridge structure and the maximum displacement of the comb actuator.

Fabrication and operation of prototype actuators provided experimental design rules (e.g. maximum length and minimum thickness of beams which do not stick) increasing thereby the reliability of the microactuators. Since even small variations of the suspension beam width of the comb actuators change considerably the drive voltage for a given displacement, the undercut uniformity for the RIE of the submicrometer-wide and 2 μm thick polysilicon beams has to be optimized.

Analytical modeling and experimental tests have led to the fabrication of optimum actuators which do not fail and still show reproducible characteristics even after extensive operation cycles; they thus meet the requirements for use in microsystems. Three applications have been described: an IC-compatible electromechanical relay, a comb-driven simple microshutter as light modulator for optical systems and a *xy* translator with integrated tip for application in atomic force microscopy.

4 Polysilicon Resonators with Integrated Excitation and Detection

4.1 Introduction

The previous two chapters have demonstrated the excellent characteristics of surface-micromachined polysilicon structures for application as IC compatible transducers. In this chapter, micromechanical structures for use as resonators are presented. A special feature of these polysilicon resonators is the integration of components for excitation and detection.

Resonant devices constitute an important sensor class by which accurate measurements can be achieved [61,162]. For instance, the mechanical frequency of resonators is highly sensitive to a variety of parameters including temperature, pressure, force, gas density and viscosity. Moreover, the frequency output of resonant sensors can be transmitted directly to digital systems and decoded by pulse counting. Because of these advantages, large efforts have been invested to realize resonators by silicon micromachining [12,62-65,75,88,91,144,158,163-177].

Several possibilities exist to drive and sense the oscillation. Thermal [88,158,169,171,172,176], piezoelectric [62,168,173], electromagnetic [63,170] and electrostatic [64,88,144,158,172,175,177] excitation is possible. As already pointed out in chapter 3, the electrostatic drive is rather promising for (surface) microstructures. Detection of the oscillation can be performed optically [62,170,176], by means of piezoresistors [64,88,158,171,172,177] or capacitively [144,158,175]. Optical detection is exhibits high accuracy, but an additional set-up (e.g. for connecting a fiber) is required. Piezoresistive sensing is a well-known principle used in membrane-deflection-based pressure sensors (see also section 1.1.3). The advantages of the capacitive detection principle are no additional processing steps and no temperature dependence, however, capacitive resonator signals are rather weak and need amplification circuitry.

In the following the theory of the transverse vibration of beams is

Parts of this chapter are published in: [175], [158] and [88].

briefly reviewed in order to obtain a simple estimation of the resonance frequency and to note the effect of axial forces on the frequencies; an exhaustive discussion of the theory of resonators can be found in standard textbooks [e.g. 178,179] as well as in earlier publications [e.g. 65,75]. Electrostatically excited and detected polysilicon beam resonators are presented; the device operation and a possible detection circuit are described, the measured frequency response of prototype devices is given. A further section deals with other types of polysilicon resonant structures having integrated elements for excitation and detection. Finally, the application of polysilicon resonators on silicon membranes for the measurement of flow velocities is discussed.

4.2 Short Theory on Vibrations of Beams

4.2.1 Resonance Frequency

The resonance frequencies of polysilicon microbridges can be approximated by applying the general equation of transverse free mechanical vibrations of prismatic beams [e.g. 178]:

$$EI \frac{\partial^4 y}{\partial x^4} = -\rho hb \frac{\partial^2 y}{\partial t^2} \tag{1}$$

where $I = bh^3/12$ the moment of inertia of the rectangular beam cross section with respect to the neutral axis, ρ the mass density of the beam, E its modulus of elasticity, y denotes the transverse displacement of a beam segment located at x (the beam ends are $x = 0$ and $x = l$), h the thickness of the beam and b its width.

When the beam vibrates transversely in one of its natural modes, the deflection at any location varies harmonically with time, as follows:

$$y(x,t) = X(x)\{A \cos pt + B \sin pt\} \ . \tag{2}$$

Substitution of eq. (2) into eq. (1) results in:

$$\frac{d^4X}{dx^4} - k^4X = 0 \qquad \text{where: } k^4 = p^2 \frac{\rho hb}{EI} \tag{3}$$

The general form of the solution for eq. (3) becomes:

$$X = C_1 \sin kx + C_2 \cos kx + C_3 \sinh kx + C_4 \cosh kx \tag{4}$$

The constants C_1, C_2, C_3 and C_4 must be determined from the boundary conditions. For a beam with fixed ends these are:

$$(X)_{x=0} = 0, \quad \left(\frac{\mathrm{d}X}{\mathrm{d}x}\right)_{x=0} = 0, \quad (X)_{x=l} = 0, \quad \left(\frac{\mathrm{d}X}{\mathrm{d}x}\right)_{x=l} = 0 \tag{5}$$

Substitution of (5) into (4) finally yields:

$$\cos kl \cosh kl = 1 \tag{6}$$

A few of the lowest consecutive roots of eq. (6) are:

k_0l	k_1l	k_2l	k_3l
0	4.730	7.853	10.996

Using (3), the frequencies as a function of the k-values are:

$$f = \frac{1}{2\pi} p = \frac{1}{2\pi} k^2 \frac{EI}{\rho hb} \; . \tag{7}$$

Thus, applying the above value for k_1, the first resonance frequency f_1 of a beam with both ends fixed can be written as:

$$f_1 = \frac{1}{2\pi} \frac{4.730^2}{l^2} \sqrt{\frac{Eh^2}{12\rho}} \tag{8}$$

As an example we can calculate the first frequencies f_1 of vibration of 1 µm thick polysilicon beams. Assuming the following material parameters for polysilicon: $\rho = 2300$ kg m^{-3} and $E = 170$ GPa [86,152, see also section 3.3.1], we obtain for 300 µm and 240 µm long beams resonance frequencies f_1 of 98 kHz and 153 kHz, respectively.

4.2.2 Effect of Axial Force on Frequency

If an oscillating (prismatic) beam is subjected to a tensile axial force F, the differential equation for transverse free vibration becomes [e.g. 178]:

$$EI \frac{\partial^4 y}{\partial x^4} - F \frac{\partial^2 y}{\partial x^2} = -\rho hb \frac{\partial^2 y}{\partial t^2} \tag{9}$$

Solving eq. (9) for a beam with both ends fixed results in the following formula for the first resonance frequency f_{1F} (under tensile force) which can be expressed as a function of f_1 of (8):

$$f_{1F} = f_1 \sqrt{1 + \frac{l^2}{4.730^2} \frac{F}{EI}} \qquad (10)$$

By substituting $F = \sigma bh$ in (10) where σ denotes the tensile stress, we obtain:

$$f_{1S} = f_1 \sqrt{1 + \frac{12}{4.730^2} \left(\frac{l^2}{h^2}\right) \frac{\sigma}{E}} \qquad (11)$$

Note that the effect of the tensile stress on the resonance frequency increases with the square of the ratio of the length and the thickness of the beam.

4.3 Performance of Electrostatically Excited and Detected Beam Resonators

4.3.1 Resonator Structure and Detection Circuit

Figure 4.1 shows the cross section of the capacitive polysilicon resonator. The structure is the identical with that of the bridge actuator prototype of Fig. 3.1 (see section 3.3.1). By applying an a.c. voltage between the upper polysilicon and the lower substrate electrode, the time-varying electrostatic forces between the two electrodes bring the free-standing beam into oscillation. This oscillation is detected by the corresponding capacitance changes of the microbridge capacitor. As indicated in Fig. 4.1, drive and detection can be performed by separate electrodes (middle and outer n-diffusions in the substrate). Thus, it is possible to utilize the polysilicon microbridge as a resonant sensor which is electrostatically driven and sensed.

In order to evaluate the output signals of these resonant microbridge sensors, their capacitance and capacitance changes are estimated. The total capacitance C_0 between the lower substrate electrode and the upper polysilicon electrode of the prototype structure of Fig. 4.1 consists of the following three capacitances in series: the air-gap capacitance C_1 with dielectric constant $\varepsilon_1 = 1$ and thickness $d_1 = 1.2$ µm, the silicon nitride capacitance C_2 with dielectric constant $\varepsilon_2 = 7$ and thickness $d_2 = 0.27$ µm and the silicon dioxide capacitance C_3 with dielectric constant $\varepsilon_3 = 3.9$ and thickness $d_3 = 0.2$ µm. The capacitances C_i (i = 1,2,3) can be approximated by applying the formula of the parallel-plate capacitor: $C_i = \varepsilon_0 \varepsilon_i A/d_i$, where $\varepsilon_0 = 8.854 \cdot 10^{-12}$ As/Vm is the permittivity in vacuum and A denotes the area of the electrodes. By choosing $A = 25$ µm x 80 µm, the electrode dimensions for a 300 µm long and 25 µm wide beam, we obtain:
$C_1 = 14.8 \cdot 10^{-15}$ F, $C_2 = 459 \cdot 10^{-15}$ F, $C_3 = 345 \cdot 10^{-15}$ F

and $C_0 = 13.8 \cdot 10^{-15}$ F.

It is obvious that C_0 is mainly determined by the air-gap capacitance C_1, and that the values of the capacitances are rather small because of the relatively small electrode areas.

Next, the capacitance change ΔC due to a downward deflection of 0.5 µm of the polysilicon beam is calculated – 0.5 µm means about one third of the total interelectrode distance between polysilicon and the substrate, i.e. the maximum deflection before sticking in the static case (see section 3.3.1). By taking $d_{1defl} = 0.7$ µm, the total capacitance C_{0defl} under deflection and the capacitance change become:

$$C_{0defl} = 22.4 \cdot 10^{-15}\,\text{F}, \qquad \Delta C = C_{0defl} - C_0 = 8.6 \cdot 10^{-15}\,\text{F}.$$

Such rather small output values require careful signal amplification; therefore, a simple detection circuit has been developed for the microbridge resonator. The circuit diagram of the resonator device is illustrated in Fig. 4.2. A similar circuit has also been used for a capacitive accelerometer [180]. Fig. 4.2 shows the separate capacitors C_e and C_b of the polysilicon microbridge used for excitation and detection. The capacitor C_b is employed in a capacitive voltage divider network from which small capacitance variations of the oscillating microbridge produce an input voltage for a simple NMOS inverter with an active load. The fixed capacitance C_a is another on-chip polysilicon capacitor, whose beam has shorter length but larger width; thus, the sacrificial layer underneath this beam has been only partly removed. Applying the same model as for C_0 in the previous paragraph, the following values for the capacitances are estimated: $C_a = 23$ fF and $C_b = 19$ fF (static case).

The SPICE simulation program was used to analyse the detection circuit of Fig. 4.2 [175]. Measurements of the NMOS transistors were carried out to derive their main input parameters for SPICE (threshold voltage, transconductance parameter, bulk threshold parameter, etc.). The simulation was performed for several values of the microbridge capacitance C_b with the other capacitance C_a fixed. For $V_{DD} = 3$ V, the SPICE simulation of the output signal V_{det} as a function of C_b results in a rather high sensitivity of about 2 mV/fF.

How Figs. 4.1 and 4.2 look like in reality, is illustrated in Figs. 4.3 and 4.4 which show a fabricated polysilicon microbeam and the test chip with the polysilicon structures mounted together with the MOS field effect transistors on a printed circuit board.

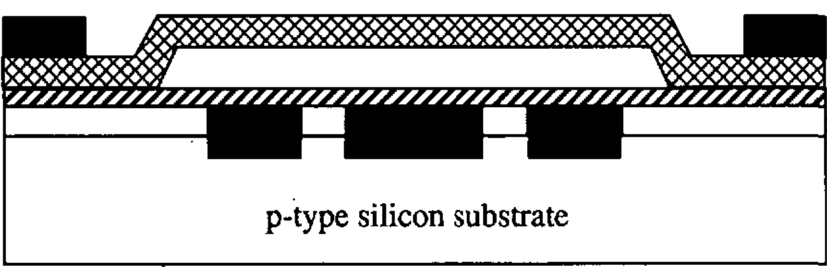

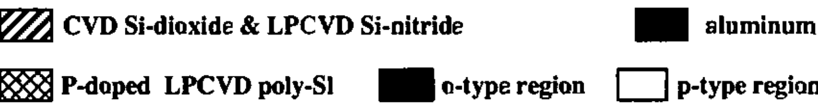

Fig. 4.1 Schematic cross section of the resonant polysilicon microbridge which is electrostatically (capacitively) excited and sensed.

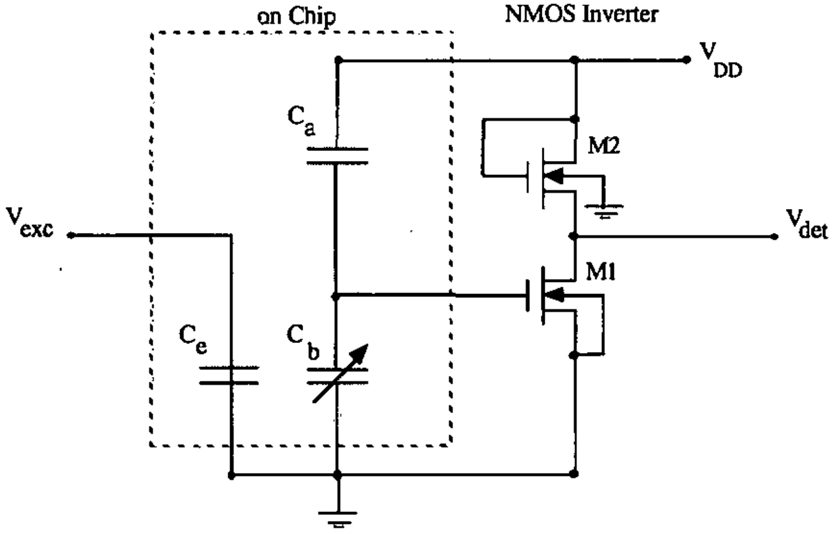

Fig. 4.2 Circuit diagram of the capacitive polysilicon resonator which is combined with another fixed polysilicon capacitor and a simple NMOS inverter.

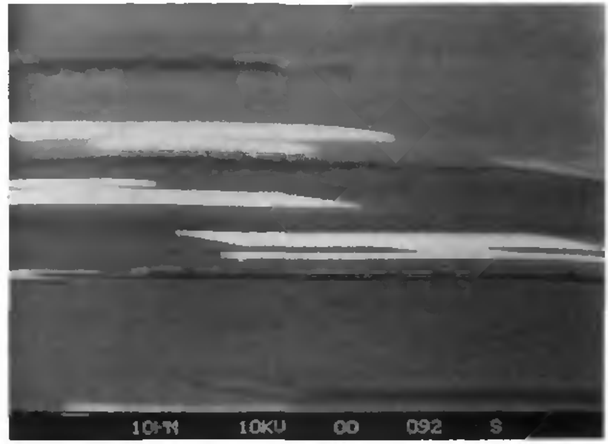

Fig. 4.3 SEM showing side view of one half of a free-standing capacitive polysilicon microbridge (300 μm long, 25 μm wide and 1 μm thick) for use as resonator; the white structures are aluminum patterns.

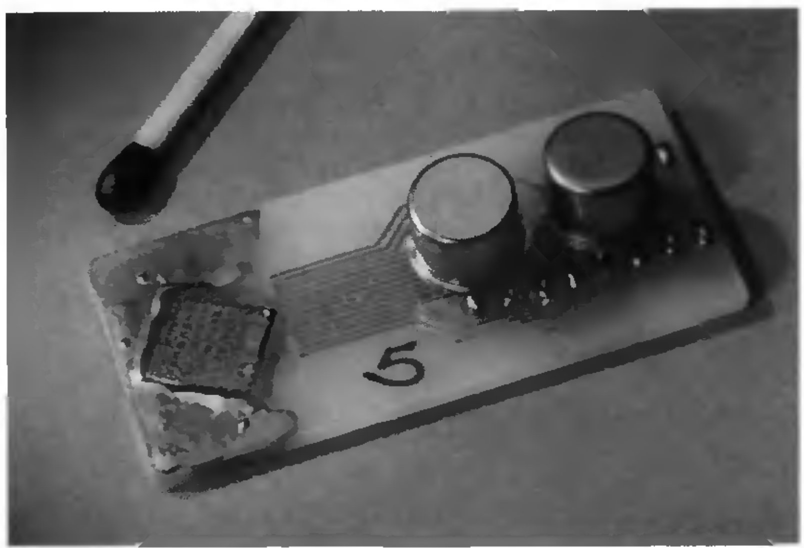

Fig. 4.4 Photograph showing a test chip with the wire-bonded capacitive polysilicon resonator (and the fixed polysilicon capacitor) mounted together with two n-channel MOSFETs (connected as a NMOS inverter) on a printed circuit board.

4.3.2 Experimental Frequency Response

Measurements were performed with the resonator device consisting of a 300 μm long, 25 μm wide and 1 μm thick polysilicon microbridge and the detection circuitry indicated in Fig. 4.2. The excitation voltage (supplied by a Function Generator) was applied at separate substrate electrodes of the microbridge. For these first experiments the two on-chip capacitances C_a and C_b were mounted together with separate NMOS transistors on a printed circuit board as indicated in Fig. 4.4.

Figure 4.6 shows the a.c. part of the directly measured output signal V_{det} for the following four frequencies: 90 kHz, 110 kHz, 120 kHz and 140 kHz. As indicated, the a.c. output voltages are in the mV range for a.c. excitation voltages of about 2 V (peak to peak). These results agree well with the SPICE simulations that predicted output voltages in the order of magnitude of mV for microbridge capacitance changes in the fF range. In addition, the four measurements illustrate that a maximum output voltage is found near 120 kHz which is 20 % higher than the first resonance frequency of free transverse vibration of the doubly clamped polysilicon beam with the same geometrical dimensions that has been calculated to be about 100 kHz (see section 4.2.1). There are several reasons for the difference between the measured and the theoretical resonance frequency. For instance, as indicated in eq. (8), only minor differences in the geometrical dimensions of the beams (e.g. in their lenghts or thicknesses) strongly affect the frequency. In addition, material parameters of the polysilicon (e.g. its modulus of elasticity), which are needed for the calculation, are not exactly known. Furthermore, it is necessary to add a d.c. bias to the a.c. part in the excitation voltage. This d.c. bias produces an electrostatic force that deflects the microbridge slightly. Thus, tensile axial stress is created in the beam which shifts the resonance frequency upwards.

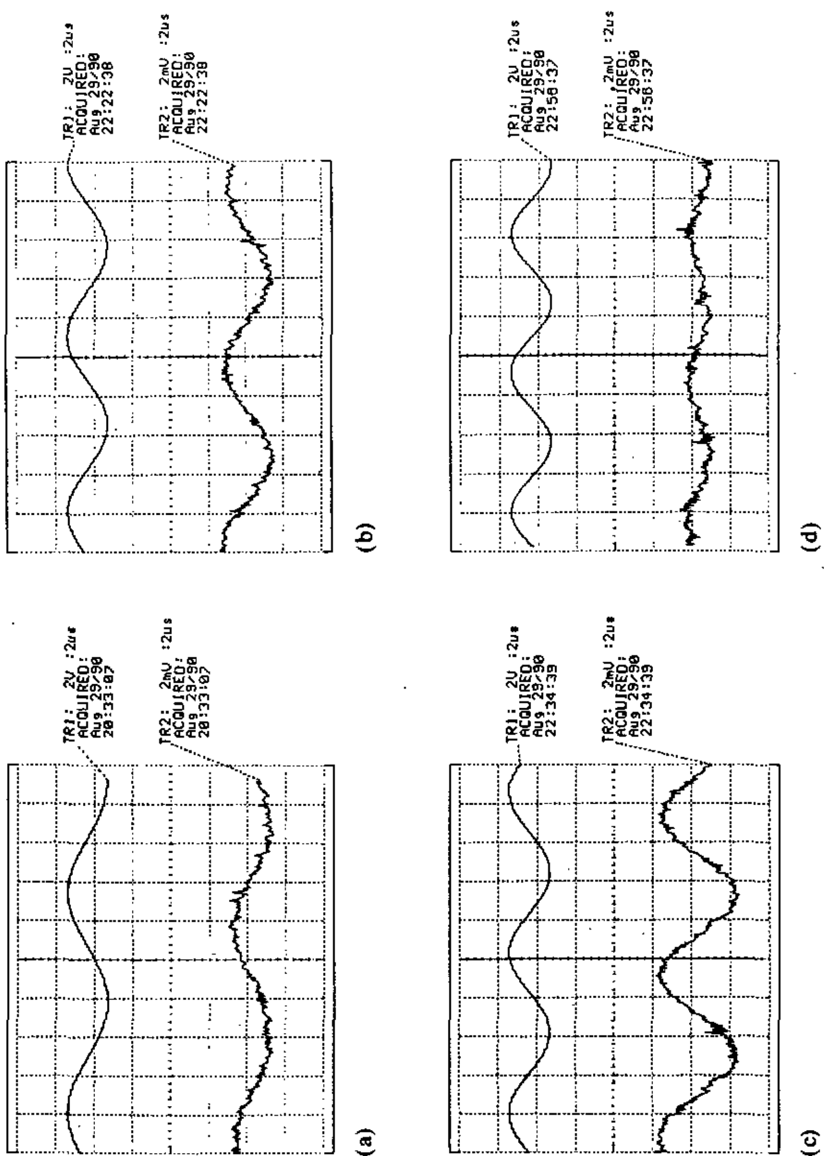

Fig. 4.6 Excitation a.c. signal (trace 1) and measured a.c. output signal (trace 2) of the resonator device (polysilicon microbridge: 300 μm long, 25 μm wide and 1 μm thick) for different frequencies: (a) 90 kHz, (b) 110 kHz, (c) 120kHz, (d) 140 kHz.

Gain/phase measurements were carried out with a HP 4194 A Analyzer. The complete experimental set-up is depicted in Fig. 4.7. Figure 4.8 shows the measured transfer function of two capacitive resonant beams having lengths 300 µm and 240 µm, respectively. A resonance peak in the gain together with a phase shift is measured at 117 kHz and 186 kHz, respectively, while the simple theory of section 4.2.1 yields 98 kHz and 153 kHz – for the difference between theoretical and experimental values, see also the previous paragraph. As expected, the output signal of these first prototype resonators are still rather weak, mainly because of parasitic effects. These have to be systematically reduced in further device generations. However, there is a good correspondence between the gain /phase and the direct measurements discussed in the previous paragraph.

The gain/phase characteristics of Fig. 4.8 are similar to curves published by Howe et al. [144] who originally proposed and investigated polysilicon resonators with electrostatic excitation and detection. Howe used circuitry different from the one shown in Fig. 4.2. Thus, it can be concluded from the similar curves that the output signal is mainly due to the mechanical resonance and not predominantly affected by the electrical operation.

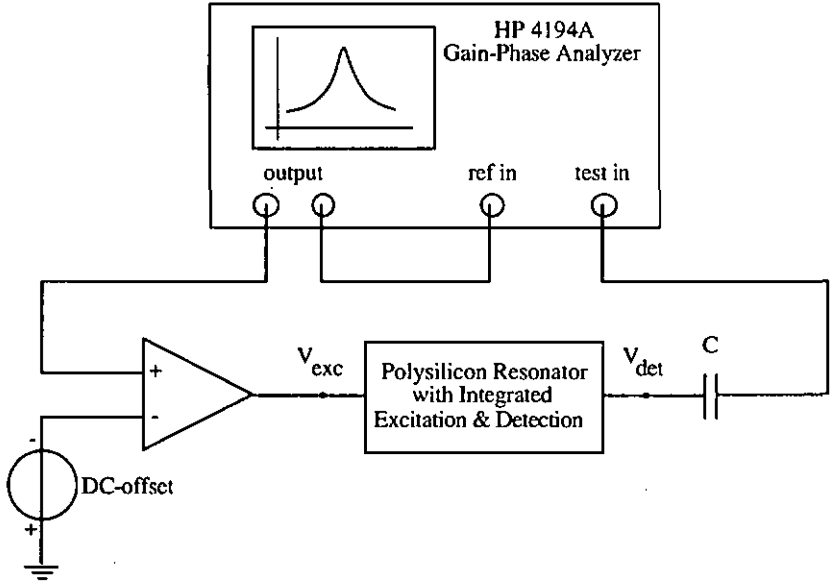

Fig. 4.7 Experimental set-up for measuring the transfer function of the polysilicon resonator device.

(a)

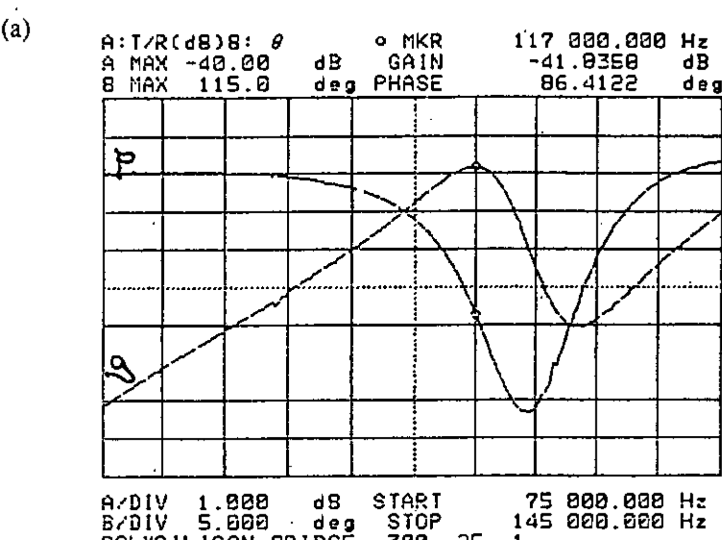

(b)

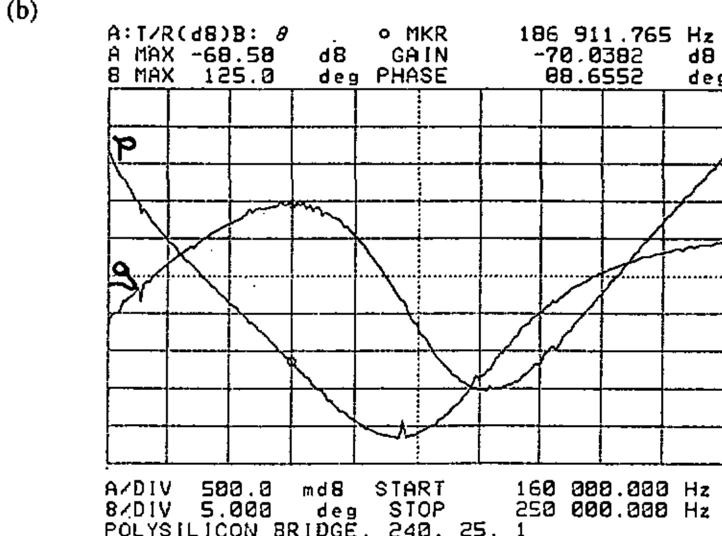

Fig. 4.8 Measured transfer function of resonator devices with polysilicon microbridge dimensions as follows:
(a) 300 μm long, 25 μm wide and 1 μm thick, resonance frequency: 117 kHz;
(b) 240 μm long, 25 μm wide and 1 μm thick, resonance frequency: 186 kHz.

4.4 Other Resonator Types

In order to compare different methods of activation and detection, other types of polysilicon resonators have been realized. For instance, the resonators shown in Figs. 4.9 and 4.10 are thermally driven by applying an a.c. voltage to a boron-doped polysilicon resistor which is placed on top of the beam. For detection, two other separate boron-doped resistors on the beam are used as piezoresistors which are connected in a Wheatstone bridge together with two fixed resistors beside the beam [171,181]. The basic beam consists of a phosphorous-doped polysilicon film that is covered by a thin insulating silicon nitride layer. On top of this double layer an additional boron-doped polysilicon film is deposited and patterned to form the lanes for drive and detection. In particular, the beam resonators of Fig. 4.10 also contain ground lanes for shielding. Thus, electrical cross-talk, a major problem in two-port devices [182], can be substantially reduced [88].

Using LOCOS polysilicon beams for these multilayer resonators is advantageous because no high steps are created when depositing additional resistor films on the planar beams. However, special attention has to be paid to mechanical stress in these multilayer structures.

As the capacitive drive, the thermal activation could be successfully applied to bring the polysilicon beams into oscillation (SEM observations). First measurements of the frequency response using the resonator of Fig. 4.9 produced an a.c. output signal whose amplitude was constant over the whole frequency range, i.e. no resonance could be detected. A possible explanation is that the temperature changes generated by the thermal excitation also create parasitic signals in the sensing piezoresistors which might be greater than the signal of the beam's oscillation and thus cover the latter. In addition, cross-talk might also have affected the output signal.

4.5 Resonant Flow Velocity Sensor – Design Considerations

As mentioned in chapter 1, differential pressure flow sensors are the most widely used in the field of traditional flow sensors and have the advantages of high reliability and repeatability [58]. The flow velocity v is proportional to the square root of the pressure drop (differential pressure) across an orifice in the flow channel [e.g. 183]:

$$v = \alpha m \sqrt{2 \frac{p1-p2}{\rho}} \tag{12}$$

Fig. 4.9 SEM showing cross section of a multilayer polysilicon beam resonator (230 μm long, 56 μm wide and 1.2 μm thick) with boron-doped resistors on top.

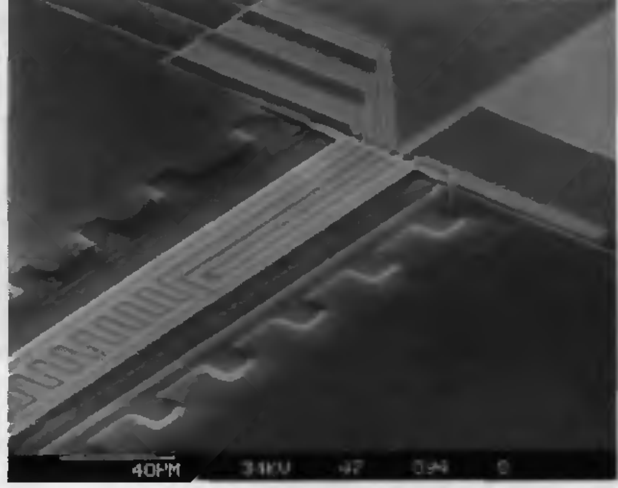

Fig. 4.10 SEM of a thermally excited and piezoresistively sensed polysilicon/nitride/polysilicon resonator (400 μm long, 39 μm wide); the activation is performed by the meander lane in the middle of the beam, the detection by piezoresistors at both ends. Note the shielding lanes between excitation and detection lines.

where p_1-p_2 is the differential pressure, ρ is the density of the fluid and αm are geometrical factors depending on the shape of the lfow channel and the orifice.

By using resonators on membranes, high-resolution pressure-based flowmeters can be realized [63-65] which, in addition, cover a large flow range. Figure 4.11 shows a schematic view of such a device where a polysilicon microbridge is placed on top of a silicon membrane. A special feature of the device is the use of two resonant pressure sensors for the measurement of the differential pressure. In addition, the polysilicon resonators are located in a sealed microcavity and hence protected against environmental parasitic effects. The fabrication consisting of the combination of membrane formation and sacrificial layer etching as well as the sealing process have been described in section 2.4.

For polysilicon beams which are placed in the middle of the sides of a square membrane, the maximum surface stress σ_{max} as a function of the applied (differential) pressure p is given by [39]:

$$\sigma_{max} = 0.31\, p\, \frac{a^2}{t^2} \tag{13}$$

where a and t are the membrane side and thickness. Thus, by substituting eq. (13) in eq. (11) from section 4.2.2, the frequency change as a function of the differential pressure and, via eq. (12), of the flow velocity can be written as:

$$f_{1s} = f_1 \sqrt{1 + \frac{1.86}{4.730^2}\, \frac{1}{E} \left(\frac{l^2}{h^2}\right) \left(\frac{a^2}{t^2}\right) \frac{\rho}{\alpha^2 m^2}\, v^2} \quad . \tag{14}$$

Using eq. (14), Table 4.1 shows calculated values of the relative frequency change for different flow velocities. A 240 μm long and 1 μm thick polysilicon microbridge resonator is assumed to be placed in the middle of the side of a 720 μm x 720 μm membrane with a thickness of 10 μm; $\alpha = 0.66$ and $m = 0.4$ are typical values taken from the tables of DIN 1952 [e.g. 183]. For velocities larger than 0.3 m/s, significant frequency changes of 10 % and more are indicated in Table 4.1. In particular, a "standard membrane" can be used to obtain this high sensitivity of the resonant sensor. Such a standard membrane is more robust than for instance the one which have been used in the flowmeter of Cho et al. [59] for direct capacitive detection of the pressure. The membrane side and thickness of the latter are about three times larger and thinner, respectively, than those of a standard membrane.

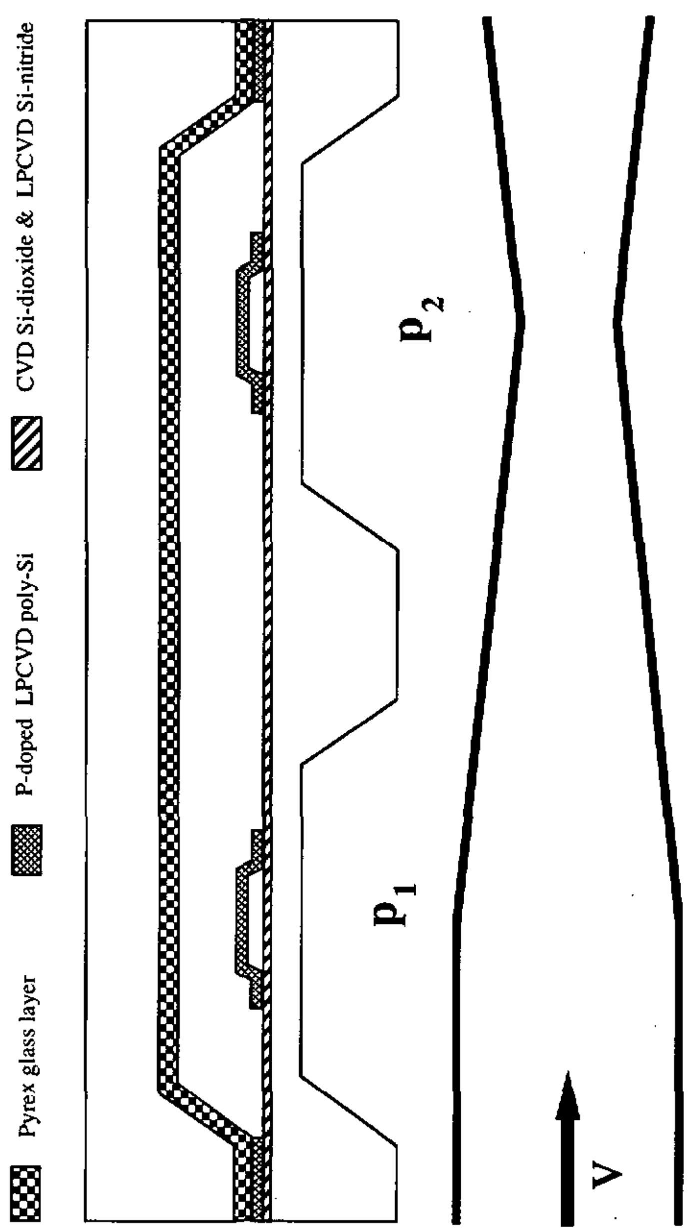

Fig. 4.11 Scheme of a flow velocity sensor based on the differential pressure principle using a resonant polysilicon microbridge on a silicon membrane.

Table 4.1 Calculated relative frequency change of a polysilicon bridge resonator (240 μm long, 1 μm thick) on a 720 μm x 720 μm silicon membrane (thickness: 10 μm) for pressure-based detection of different flow velocities.

v [m/s]	0.1	0.2	0.3	0.5	1
$(f_{1S} - f_1) / f_1$	0.01	0.04	0.09	0.23	0.76

4.6 Conclusion

Different microresonators with integrated drive and sensing components have been fabricated and compared. The oscillating elements consist of IC compatible free-standing polysilicon beams fabricated by the sacrificial layer technology.

Both thermal and electrostatic excitation have been successfully performed; in order to avoid thermal parasitic effects, electrostatic drive is preferred. By applying a simple adequate detection circuit consisting of a capacitive voltage divider and a NMOS inverter, detection of the resonator signal has been accomplished by measuring the capacitance changes between the polysilicon and a substrate electrode; the frequency response has been examined by gain/phase measurements. As an alternative method the well-established piezoresistive detection has been demonstrated; the polysilicon piezoresistors as well as separate lanes for driving and shielding are integrated on top of a polysilicon/nitride multilayer beam.

By placing an oscillating polysilicon beam on a silicon membrane, the high sensitivity of resonant sensors is exploited for the measurement of (differential) pressure.

5 Conclusion

Highly sophisticated IC components for microprocessors are available today, and a major issue for further improvement of instrumentation systems is to lower the cost and to maintain or increase the perfomance of the input and output transducers (sensors and actuators). Furthermore, the enormous research activities invested by the electronics industry to control the electronic performance of silicon have simultaneously revealed the excellent mechanical properties of silicon. Thus, based on thin-film and IC technology, silicon micromachining has been developed as a powerful tool for the fabrication of micromechanical devices and, in general, miniature transducers.

Surface micromachining techniques such as sacrificial layer etching or special dry etching processes have been demonstrated to be an attractive alternative to the well-established bulk micromachining of silicon. However, bulk and surface micromachining techniques are not only diverging or competing with each other, but they will also help to increase the wide variety of batch-fabricated microsensors and microactuators in silicon and the integration of the latter with microelectronics. Bulk micromachining, for instance, will be preferably used in applications where the mechanical fragility or the small masses of surface-micromachined structures are major drawbacks. If an IC compatible fabrication process is needed in a special application, surface-micromachined devices which consist of polysilicon, silicon dioxide and/or aluminum are advantageous. In particular, the combination of bulk and surface micromachining will be an oncoming field of research and development; examples have been described.

Prototypes of polysilicon transducers fabricated by selective lateral etching of an underlying sacrificial silicon dioxide layer have been investigated: free-standing microbeam actuators for applications as electromechanical switches, optical shutters and nano-positioners; microbridge resonators with integrated elements for excitation (electrostatic, thermal) and detection (capacitive, piezoresistive) for application as accurate flow sensors. Based on the well-experienced high-reliable polysilicon technology, the prototype structures show reproducible characteristics and are promising for further development and industrial application.

References

[1] S. Middelhoek and D. J. W. Noorlag, " Three-dimensional representation of input and output transducers", *Sensors and Actuators*, vol. 2, pp. 29-41, 1981/82.

[2] K. D. Wise and N. Najafi, "The coming opportunities in microsensor systems", *Tech. Dig. Int. Conf. Solid-State Sensors and Actuators* (Transducers '91), San Francisco, CA, June 1991, pp. 2-7.

[3] R. A. Colclaser, *Microelectronics: Processing and Decive Design*, Wiley, New York, 1980.

[4] S. M. Sze, Ed., *VLSI Technology*, McGraw-Hill, New York, 1983.

[5] C. S. Smith, "Piezoresistance effect in germanium and silicium", *Phys. Rev.*, vol. 94, pp. 42-49, 1954.

[6] S. Middelhoek and A. C. Hoogerwerf, "Smart sensors: when and where", *Tech. Dig. Int. Conf. Solid-State Sensors and Actuators* (Transducers '85), Philadelphia, PA, June 1985, pp. 2-7.

[7] *Journal of Microelectromechanical Systems*, IEEE and ASME.

[8] T. P. Ma, "Sresses in SiO2-on-Si structures", in *Properies of Silicon*, EMIS Datareviews Series No. 4, INSPEC, London, 1988, p. 654.

[9] P. J. French and A. G. R. Evans, "Piezoresistance in single crystal and polycrystalline Si", in *Properies of Silicon*, EMIS Datareviews Series No. 4, INSPEC, London, 1988, p. 99.

[10] H. Guckel, D. W. Burns, H.A.C. Tilmans, D. W. DeRoo and C. R. Rutigliano, "Mechanical properties of fine grained polysilicon the repeatability issue, *Tech. Dig. IEEE Solid-State Sensor and Actuator Workshop*, Hilton Head Island, SC, June 1988, pp. 96 - 99.

[11] L. S. Fan and R. S. Muller, "As-deposited low srain LPCVD polysilicon", *Tech. Dig. IEEE Solid-State Sensor and Actuator Workshop*, Hilton Head Island, SC, June 1988, pp. 55-58.

[12] M. W. Putty, S. C. Chang, R. T. Howe, A. L. Robinson and K. D. Wise, "One-port active polysilicon resonant microstructures", *Proc. IEEE Micro Electro Mech. Syst. Workshop*, Salt Lake City, UT, February 1989, pp. 60-65.

[13] T. Hirano, T. Furuhata, K. J. Gabriel and H. Fujita, "Design, fabrication and operation of submicrometer gap comb-drive microactuators", *J. Microelectromech. Syst.*, vol. 1, pp. 52-59, March 1992.

[14] W. C. Tang, T. H. Nguyen and R. T. Howe, "Laterally driven polysilicon resonant microstructures", *Proc. IEEE Micro Electro Mech. Syst. Workshop*, Salt Lake City, UT, February 1989, pp. 53-59.

[15] R. I. Pratt, G. C. Johnson, R. T. Howe and J. C. Chang, "Micromechanical structures for thin-film characterization", *Tech. Dig. Int. Conf. Solid-Stote Sensors and Actuotors* (Transducers '91), San Francisco, CA, June 1991, pp. 205-208.

[16] J. A. Walker, K. J. Gabriel and M. Mehregany, "Mechanical integrity of polysilicon films exposed to hydrofluoric acid solutions", *Proc. IEEE Micro Electro Mech. Syst. Workshop*, Nappa Valley, CA, February 1990, pp. 56-60.

[17] Y. C. Tai and R. S. Muller, "Fracture strain of LPCVD polysilicon", *Tech. Dig. IEEE Solid-Stote Sensor ond Actuotor Workshop*, Hilton Head Island, SC, June 1988, pp. 88-91.

[18] V. P. Jaecklin, C. Linder, J. Brugger, J.-M. Moret, R. Vuilleumier and N. F. de Rooij, "Mechanical and optical properties of surface micromachined torsional mirrors in silicon, polysilicon and aluminum", *Tech. Dig. Int. Conf. Solid-State Sensors and Actuators* (Transducers '93), Yokohama, Japan, June 1993.

[19] S. M. Sze, *Physics of Semiconductor Devices*, 2nd ed., Wiley, New York, 1981, Appendix H.

[20] C. H. Mastrangelo and R. S. Muller, "Thermal diffusivity of heavily doped low pressure chemical vapor deposited polycrystalline silicon films", *Sensors ond Moteriols*, vol. 1, pp. 133-142, 1988.

[21] T. I. Kamins, "Hall mobility in chemically deposited polycrystalline silicon", *J. Appl. Phys.*, vol. 42, pp. 4357-4365, 1971.

[22] J. Y. W. Seto, "The electrical properties of polycrystalline silicon films", *J. Appl. Phys.*, vol. 46, pp. 5247-5254, 1975.

[23] E. Obermeier, P. Kopystynski and R. Niessl, "Characteristics of polysilicon layers and their application in sensors", *Tech. Dig. IEEE Solid-State Sensors Workshop*, Hilton Head Island, SC, June 1986, pp. 1-4.

[24] Y. Kanda, "A graphical representation of the piezoresistance coefficients in silicon", *IEEE Trans. Electron Devices*, vol. 29, pp. 64-70, 1982.

[25] T. Tschan, "Simulation, Design and Characterization of a Piezoresistive Accelerometer, fabricated by a bipolar-compatible industrial process", Ph. D. dissertation, Institute of Microtechnology, University of Neuchâtel, 1992.

[26] J. Y. W. Seto, "Piezoresistive properties of polycrystalline silicon", *J. Appl. Phys.*, vol. 47, pp. 4780-4783, 1976.

[27] D. Schubert, W. Jenschke, T. Uhlig and F. M. Schmidt, "Piezoresistive properties of polycrystalline and crystalline silicon films", *Sensors and Actuators*, vol. 11, pp. 145-155, 1987.

[28] P. J. French and A. G. R. Evans, "Piezoresistance in polysilicon and its apllications to strain gauges", *Solid-State Electronics*, vol. 32, pp. 1-10, 1989.

[29] J. Suski, V. Mosser and J. Goss, "Polysilicon SOI pressure sensor", *Sensors and Actuators*, vol. 17, pp. 405-414, 1989.

[30] T. J. Quinn, *Temperature*, Academic Press, London, 1983.

[31] L. Crovini, P. Marcarino, A. Actis and R. Dematteis, "Report on the comparative measurements of the resistance of IPRT's with three bridges (DC: 28.5 Hz; 318 Hz)", *IMGC internal report S/240*, IMGC, Turin, Italy, 1985.

[32] W. Diehl, "Platin-Dünnschicht-Widerstände als genaue und stabile Temperatur-Sensoren", *Sensor '82 - Transducer Technology and Temperature Measurement*, vol. 2, Network GmbH, Wunstorf, pp. 89-101, 1982.

[33] P. Kopystynski and E. Obermeier, "The wide-ranging applications of polysilicon layers in solid-state sensors", *Sensors and Actuators*, vol. 17, pp. 69-73, 1989.

[34] M. P. Timko, "A two-terminal IC temperature transducer", *IEEE J. Solid-State Circuits*, vol. 11, pp. 784-788, 1976.

[35] A. Othe, "A precision silicon transistor thermometer", *IEEE Trans. Instrum. and Measurement*, vol. 26, pp. 335-341, 1977.

[36] O. N. Tufte, P. W. Chapman and D. Long," Silicon diffused-element piezoresistive diaphragms", *J. Appl. Phys.*, vol. 33, pp. 3322-3327, 1962.

[37] Samaun, K. D. Wise and J. B. Angell, "An IC piezoresistive pressure sensor for biomedical instrumentation", *IEEE Trans. Biomed. Eng.*, vol. 20, pp. 101-109, 1973.

[38] S. K. Clark and K. D. Wise, "Pressure sensitivity in anisotropically etched thin-diaphragm pressure sensors", *IEEE Trans. Electron Devices*, vol. 26, pp. 1887-1896, 1979.

[39] B. Kloeck, "Design, fabrication and characterization of piezoresistive pressure sensors, including the study of electrochemical etch-stop", Ph. D. dissertation, Institute of Microtechnology, University of Neuchâtel, 1989.

[40] H. Seidel, "The mechanism of anisotropic, electro-chemical silicon etching in alkaline solutions", *Tech. Dig. IEEE Solid-State Sensor and Actuator Workshop*, Hilton Head Island, SC, June 1990, pp. 86-91.

[41] B. Kloeck, S. D. Collins, N. F. de Rooij and R. L. Smith, "Study of electromechanical etch-stop for high-precision thickness control of silicon membranes", *IEEE Trans. Electron Devices*, vol. 36, pp. 663-669, 1989.

[42] W. H. Ko, J. T. Suminto and G. J. Yeh, "Bonding techniques for microsensors", in C. D. Fung, P. W. Cheung, W. H. Ko and D. G. Fleming (eds.), *Micromachining and Micropackaging of Transducers*, Elsevier, Amsterdam, 1985, pp. 41-62.

[43] C. S. Sander, J. W. Knutti and J. D. Meindl, "A monolithic capacitive pressure sensor with pulse-period output", *IEEE Trans. Electron Devices*, vol. 17, pp. 927-930, 1980.

[44] Y. S. Lee and K. D. Wise, "A batch-fabricated silicon capacitive pressure transducer with low temperature sensitivity", *IEEE Trans. Electron Devices*, vol. 29, pp. 42-48, 1982.

[45] W. H. Ko, M. H. Bao, Y. D. Hong, "A high-sensitivity integrated-circuit capacitive pressure transducer", *IEEE Trans. Electron Devices*, vol. 29, pp. 48-56, 1982.

[46] J. T. Kung and H. S. Lee, "An integrated air-gap-capacitor pressure sensor and digital readout with sub-100 attofarad resolution", *J. Microelectromech. Syst.*, vol. 1, pp. 121-129, 1992.

[47] C. Linder, "Evaluation von Sensoren für Klimaanlagen, insbeondere von Fluss-Sensoren", *Internal Report No 208 EC 01/87*, IMT, University of Neuchâtel, 1987.

[48] J. I. Huijsing, J. P. Schuddemat and W. Verhoef, "Monolithic integrated direction-sensitive flow sensor", *IEEE Trans. Electron Devices*, vol. 29, pp. 133-136, 1982.

[49] A. F. T. van Putten, "An integrated silicon double-bridge anemometer", *Sensors and Actuators*, vol. 4, pp. 387-396, 1983.

[50] K. E. Petersen, J. Brown and W. Renken, "High-precision high-performance mass-flow sensor with integrated laminar flow micro-channels, *Tech. Dig. Int. Conf. Solid-State Sensors and Actuators* (Transducers '85), Philadelphia, PA, June 1985, pp. 361-363.

[51] G. B. Hocker, R. G. Johnson, R. E. Higashi and P. J. Bohrer, "A microtransducer for air flow and differential pressure sensing applications", in C. D. Fung, P. W. Cheung, W. H. Ko and D. G. Fleming (eds.), *Micromachining and Micropackaging of Transducers*, Elsevier, Amsterdam, 1985, pp. 207-214.

[52] O. Tabata, "Fast-response silicon flow sensor with an on-chip fluid temperature sensing element", *IEEE Trans. Electron Devices*, vol. 33, pp. 361-365, 1986.

[53] G. N. Stemme, "A monolithic gas flow sensorwith polyimide as thermal insulator", *IEEE Trans. Electron Devices*, vol. 33, pp. 1470-1474, 1986.

[54] Y. C. Tai and R. S. Muller, "Lightly-doped polysilicon bridge as anemometer", *Tech. Dig. Int. Conf. Solid-State Sensors and Actuators* (Transducers '87), Tokyo, Japan, June 1987, pp. 360-363.

[55] B. W. van Oudheusden and A. W. van Herwaarden, "High-sensitivity 2-D flow sensor with an etched thermal isolation structure", *Sensors and Actuators*, A22, pp. 420-425, 1990.

[56] E. Yoon and K. D. Wise, "An integrated mass flow sensor with on-chip CMOS interface circuitry", *IEEE Trans. Electron Devices*, vol. 39, pp. 1376-1386, 1992.

[57] A. J. van der Wiel, C. Linder, N. F. de Rooij and A. Bezinge, "A liquid velocity sensor based on the hot-wire principle", accepted for *Sensors and Actuators A*, 1992.

[58] *Low Cost Sensors Technology and Applications*, Mackintosh State of the Art Series, Benn Electronics Publications Ltd, 1983.

[59] S. T. Cho, K. Najafi, C. E. Lowman and K. D. Wise, "An ultrasensitive silicon pressure-based microflow sensor", *IEEE Trans. Electron Devices*, vol. 39, pp. 825-835, 1992.

[60] V. Gass, B. H. van der Schoot and N. F. de Rooij, "Nanofluid handling by micro-flow-sensor based on drag force measurements", *Proc. IEEE Micro Electro Mech. Syst. Workshop*, Fort Lauderdale, FL, February 1993, pp. 167-172.

[61] R. M. Langdon, "Resonator sensors - a review", *J. Phys. E: Sci. Instrum.*, vol. 18, pp. 103-115, 1985.

[62] R. A. Buser and N. F. de Rooij, "Very high Q-factor resonators in monocrystalline silicon", *Sensors and Actuators*, A21-23, pp. 323-327, 1990.

[63] K. Ikeda, H. Kuwayama, T. Kobayashi, T. Watanabe, T. Nishikawa, T. Yoshida and K. Harada, "Silicon pressure sensor integrates resonant strain gauge on diaphragm", *Sensors and Actuators*, A21-23, pp. 146-150, 1990.

[64] J. D. Zook, D. W. Burns, H. Guckel, J. J. Sniegowski, R. L. Engelstad and Z. Feng, "Characteristics of polysilicon resonant microbeams", *Sensors and Actuators A*, vol. 35, pp. 51-59, 1992.

[65] H. A. C. Tilmans, "Micro-mechanical sensors using encapsulated built-in resonant strain gauges", Ph. D. dissertation, MESA Research Institute, University of Twente, 1993.

[66] R. T. Howe, "Surface micromachining for microsensors and microactuators", *J. Vac. Sci. Technol. B*, vol. 6, pp. 1809-1813, 1988.

[67] H. Guckel, "Surface micromachined pressure transducers", *Sensors and Actuators A*, vol. 28, pp. 133-146, 1991.

[68] M. Mehregany, K. J. Gabriel, and W. S. N. Trimmer, "Integrated fabrication of polysilicon mechanisms", *IEEE Trans. Electron Devices*, vol. 35, pp. 719-723, 1988.

[69] L.-S. Fan, Y.-C- Tai, and R. S. Muller, "Integrated movable micromechanical structures for sensors and actuators", *IEEE Trans. Electron Devices*, vol. 35, pp. 724-730, 1988.

[70] C. Linder, L. Paratte, M.-A. Grétillat, V. P. Jaecklin and N. F. de Rooij, "Surface micromachining", *J. Micromech. Microeng.*, vol. 2, pp. 122-132, 1992.

[71] K. Petersen, "Silicon as a mechanical material", *Proc. IEEE*, vol. 70, pp. 420-457, 1982.

[72] S. J. Sherman, W. K. Tsang, T. A. Core, R. S. Payne, D. E. Quinn, K. H.-L. Chau, J. A. Farash and S. K. Baum, "A low cost monolithic accelerometer; product/technology update", *Tech. Dig. IEEE IEDM*, San Francisco, CA, 1992 pp. 501-504.

[73] W. C. Dunn, "Accelerometer design considerations", in H. Reichl (ed.), *Micro System Technologies 90*, Springer, Berlin, 1990, pp. 131-136.

[74] "Capacitance-based acceleration sensor combines bulk and surface micromachining", *Electronic Design*, Dec. 3, 1992, pp. 35-37.

[75] R. A. Buser, "Theoretical and experimental investigations on silicon single crystal resonant structures", Ph. D. dissertation, Institute of Microtechnology, University of Neuchâtel, 1989.

[76] R. T. Howe and R. S. Muller, "Polycrystalline silicon micromechanical beams", *J. Electrochem. Soc.*, vol. 130, pp. 1420-1423, 1983.

[77] R. T. Howe, "Polycrystalline silicon microstructures", in C. D. Fung, P. W. Cheung, W. H. Ko and D. G. Fleming (eds.), *Micromachining and Micropackaging of Transducers*, Elsevier, Amsterdam, 1985, pp. 169-187.

[78] H. Guckel and D. W. Burns, "Planar processed polysilicon sealed cavities for micromechanical sensors", *ITech. Dig. IEEE IEDM*, San Francisco, CA, 1984, pp. 223-225.

[79] H. Guckel, D. W. Burns, "Fabrication techniques for integrated sensor microstructures", *Tech. Dig. IEEE IEDM*, Los Angeles, CA, 1986, pp. 176-179.

[80.1] M. Parameswaran, H. P. Baltes, Lj. Ristic, A. C. Dhaded and A. M. Robinson, "A new approach for the fabrication of micromechanical structures", *Sensors and Actuators*, vol. 19, pp. 289-307, 1989.

[80.2] M. Kandler, Y. Manoli, W. Mokwa, E. Spiegel, H. Vogt, "A miniature single-chip pressure and temperature sensor", *J. Micromech. Microeng.*, vol. 2, pp. 199-201, 1992.

[81] H. C. Nathanson, W. E. Newell, R. A. Wickstrom, and J. R. Davis Jr., "The resonant gate transistor", *IEEE Trans. Electron Devices*, vol. 14, pp. 117-133, 1967.

[82] B. Hälg, "On a micro-mechanical nonvolatile memory cell", *IEEE Trans. Electron Devices*, vol. 37, pp. 2230-2236, 1990.

[83] S. Sugiyama, K. Shimaoka, and O. Tabata, "Surface micromachined micro-diapragm pressure sensors", *Tech. Dig. Int. Conf. Solid-State Sensors and Actuators* (Transducers '91), San Francisco, CA, June 1991, pp. 188-191.

[84] P. R. Scheeper, W. Olthuis, and P. Bergveld, "Fabrication of a subminiature silicon condenser microphone using the sacrificial technology", *Tech. Dig. Int. Conf. Solid-State Sensors and Actuators* (Transducers '91), San Francisco, CA, June 1991, pp. 408-411.

[85] C. Linder and N.F. de Rooij, "Investigations on free-standing polysilicon beams in view of their application as resonators", *Abstr. Dig. Transducers '89*, Montreux, Switzerland, 1989, COMST, Lausanne, pp. 289-290.

[86] C. Linder and N.F. de Rooij, "Investigations on free-standing polysilicon beams in view of their application as transducers", *Sensors and Actuators*, A21-23, pp. 1053-1059, 1990.

[87] K. Y. Chiu, J. L. Moll, and J. Manoliu, "A bird's beak free local oxidation technology feasible for VLSI circuits fabrication," *IEEE Trans. Electron Devices*, vol. 29, pp. 536-540, 1982.

[88] M.-A. Grétillat, C. Linder and N. F. de Rooij, "Multilayer polysilicon resonators including shielding for excitation and detection", *Tech. Dig. Int. Conf. Solid-State Sensors and Actuators* (Transducers '93), Yokohama, Japan, June 1993.

[89] T. I. Kamins, "Structure and stability of low pressure chemically vapor-deposited silicon films", *J. Electrochem. Soc.*, vol. 125, pp. 927-932, 1978.

[90] H. Guckel, D. W. Burns, C. R. Rutigliano, D. K. Showers and J. Uglow, "Fine grained polysilicon and its application to planar pressure transducers", *Tech. Dig. Int. Conf. Solid-State Sensors and Actuators* (Transducers '87), Tokyo, Japan, June 1987, pp. 277-282.

[91] H. Guckel, J. J. Sniegowski, T. R. Christenson, and F. Raissi, "The application of fine-grained, tensile polysilicon to mechanically resonant transducers", *Sensors and Actuators*, A21-23, pp 346-351, 1990.

[92] T. I. Kamins, "Structure and properties of LPCVD silicon films", *J. Electrochem. Soc.*, vol. 127, pp. 686-690, 1980.

[93] G. Harbeke, L. Krausbauer, E. F. Steigmeier, A. E. Widmer, H. F. Happert and G. Neugebauer, "Growth and physical properties of LPCVD polycrystalline silicon films", *J. Electrochem. Soc.*, vol. 131, pp. 675-682, 1984.

[94] T. I. Kamins, "Design properties of polycrystalline silicon", *Sensors and Actuators*, A21-23, pp. 817-824, 1990.

[95] T. A. Lober, R. T. Howe, "Surface-micromachining processes for electrostatic microactuator fabrication, *Tech. Dig. IEEE Solid-State Sensor and Actuator Workshop*, Hilton Head Island, SC, June 1988, pp. 59-62.

[96] H. Guckel, J. J. Sniegowski and T. R. Christenson, Advances in processing techniques for silicon micromechanical devices with smooth surfaces, *Proc. IEEE Micro Electro Mech. Syst. Workshop*, Salt Lake City, UT, February 1989, pp. 71-75.

[97] P. R. Scheeper, J. A. Voorthuyzen, W. Olthuis and P. Bergveld, "Investigation of attractive forces between PECVD silicon nitride microstructures and an oxidized silicon substrate", *Sensors and Actuators A*, vol. 30, pp. 231-239, 1992.

[98] M. Mehregany, P. Nagarkar, S. D. Senturia and J. H. Lang, "Operation of microfabricated harmonic and ordinary side-drive motors", *Proc. IEEE Micro Electro Mech. Syst. Workshop*, Napa Valley, CA, February 1990, pp. 1-8.

[99] C. Kittel, *Introduction to Solid State Physics*, 5th ed., Wiley, New York, 1976, ch. 3.

[100] N. Takeshima, K. J. Gabriel, M. Ozaki, J. Takahashi, H. Horiguchi and H. Fujita, "Electrostatic parallelogram actuators", *Tech. Dig. Int. Conf. Solid-State Sensors and Actuators* (Transducers '91), San Francisco, CA, June 1991, pp. 63-66.

[101] A. Kovacs and A. Stoffel, "Process optimization of free-standing polysilicon microstructures", *J. Micromech. Microeng.*, vol. 2, pp. 190-192, 1992.

[102] W. Kern and C. A. Deckert, "Chemical Etching", in J. L. Vossen and W. Kern, Eds., *Thin Film Processes*, Academic Press, New York, 1978, ch. V-1.

[103] C. J. Mogab, "Dry etching", in S. M. Sze, Ed., *VLSI Technology*, McGraw-Hill, New York, 1983, ch. 8.

[104] C. Linder, T. Tschan and N.F. de Rooij, "Deep dry etching techniques as a new IC-compatible tool for silicon micromachining, *Tech. Dig. Int. Conf. Solid-State Sensors and Actuators* (Transducers '91), San Francisco, CA, June 1991, pp. 524-527.

[105] C. Linder, T. Tschan and N.F. de Rooij, "Deep dry etching of silicon - a novel micromachining tool", *Sensors and Materials*, vol. 3, pp.311-324, 1992.

[106] M. Mehregany, K. J. Gabriel and W. S. N. Trimmer, "Micro gears and turbines etched from silicon", *Sensors and Actuators*, vol. 12, pp. 341-348, 1987.

[107] R. Pinto, K.V. Ramanathan and R.S. Babu, "Reactive ion etching in SF6 gas mixtures", *J. Electrochem. Soc.*, vol. 134, pp.165-175, 1987.

[108] T. Tschan, C. Linder and N.F. de Rooij, "Dry etching techniques for silicon micromachining", *Proceedings of Micromechanics Europe*, Berlin, 1990, pp. 253-260.

[109] J.P. McVittie and C. Gonzalez, "Anisotropic etching of Si using SF6:C2ClF5", *Extended Abstracts, Fall Meeting, Electrochem. Soc.*, vol. 84-2, pp. 584-585.

[110] Y. B. Gianchandani and K. Najafi, "A bulk silicon dissolved wafer process for microelectromechanical devices", *J. Microelectromech. Syst.*, vol. 1, pp. 77-85, 1992.

[111] M. Seel and P. Bagus, "*Ab initio* cluster study of the interaction of fluorine and chlorine with the Si(111) surface", *Phys. Rev. B*, vol. 28, pp. 2023-2038, 1983.

[112] Z. Lisa Zhang and Noel C. MacDonald, "An RIE process for submicron, silicon electromechanical structures", *Tech. Dig. Int. Conf. Solid-State Sensors and Actuators* (Transducers '91), San Francisco, CA, June 1991, pp. 520-523.

[113] T. Hirano, T. Furuhata and H. Fujita, "Dry releasing of electroplated rotational and overhanging structures", *Proc. IEEE Micro Electro Mech. Syst. Workshop*, Ft. Lauderdale, FL, February 1993, pp. 278-283.

[114] R. S. Hijab and R. S. Muller, "Micromechanical thin-film cavity structures for low-pressure and accoustic transducer applications", *Tech. Dig. Int. Conf. Solid-State Sensors and Actuators* (Transducers '85), Philadelphia, PA, June 1985, pp. 178-181.

[115] K. Petersen, D. Gee, F. Pourahmadi, R. Craddock, J. Brown and L. Christel, "Surface micromachined structures fabricated with silicon fusion bonding", *Tech. Dig. Int. Conf. Solid-State Sensors and Actuators* (Transducers '91), San Francisco, CA, June 1991, pp. 397-399.

[116] J. T. Kung and H.-S. Lee, "An integrated air-gap-capacitor process for sensor applications", *Tech. Dig. Int. Conf. Solid-State Sensors and Actuators* (Transducers '91), San Francisco, CA, June 1991, pp. 1010-1013.

[117] C. J. Kim, A. P. Pisano and R. S. Muller, "Silicon-processed overhanging microgripper", *J. Microelectromech. Syst.*, vol. 1, pp. 31-36, 1992.

[118] P. R. Scheeper, A. G. H. van der Donk, W. Olthuis and P. Bergveld, "Fabrication of silicon condenser microphones using single wafer technology", *J. Microelectromech. Syst.*, vol. 1, pp. 147-154, 1992.

[119] A. Hanneborg, M. Nese, H. Jacobson and R. Holm, "Silicon-to-thin film anodic bonding", *J. Micromech. Microeng.*, vol. 2, pp. 117-121, 1992.

[120] T. Tschan, N. F. de Rooij, A. Bezinge, S. Ansermet and J. Berthoud, "Characterization and modeling of silicon piezoresistive accelerometers fabricated by a bipolar-compatible process", *Sensors and Actuators A*, vol. 25-27, pp. 605-609, 1991.

[121] R. Buser, J. Brugger, C. Linder and N.F. de Rooij, "Micromachined silicon cantilevers and tips for bidirectional force microscopy", *Tech. Dig. Int. Conf. Solid-State Sensors and Actuators* (Transducers '91), San Francisco, CA, June 1991, pp. 249-252.

[122] R. Buser, J. Brugger, C. Linder (Appls. & Invs.), British Technology Group Ltd. (Appl.), *Microprobe for Surface-Sconning Microscopes*, Patent, PCT/GB92/01060, 12 June 1992.

[123] V. P. Jaecklin, J. Brugger, C. Linder, P.-F. Indermühle and N. F. de Rooij, "Micromachined overhanging xy-actuator with protruding tip for scanned probe devices", accepted for presentation at *EUROSENSORS VII*, Budapest, Hungary, September 1993.

[124] J. Brugger, V. P. Jaecklin, P.-F. Indermühle, C. Linder and N. F. de Rooij, "Fabrication of an overhanging xy-microactuator with integrated tip for scanned surface profiling", accepted as *Late News at Transducers '93*, Yokohama, Japan, June 1993.

[125] C. Harendt, H.-G. Graf, B. Höfflinger and E. Penteker, "Silicon fusion bonding and its characterization", *J. Micromech. Microeng.*, vol. 2, pp. 113-116, 1992.

[126] T. Hayashi, "Micro mechanisms", *J. of Robotics and Mechatronics*, vol. 3, pp. 2-7, 1991.

[127] P. Dario and R. Valleggi, "Microrobotics: shifting robotics technology towards a different scale world", *The Robotics Review 2*, MIT Press, 1992.

[128] B. H. van der Schoot, S. Jeanneret, A. van den Berg and N. F. de Rooij, "A silicon integrated miniature chemical analysis system", *Sensors and Actuators*, B6, pp. 57-60, 1992.

[129] K. Kajimura, "STM as a micromachine", *J. of Robotics and Mechatronics*, vol. 3, pp. 12-17, 1991.

[130] W. Trimmer, "Micromechanical systems", in *Integrated micro-motion systems*, F. Harashima, Ed., Elsevier, Amsterdam, 1990, pp. 1-15.

[131] A. P. Pisano, "Resonant-structure micromotors: historical perspective and analysis", *Sensors ond Actuators*, A20, pp. 83-89, 1989.

[132] E. Dieulesaint, D. Royer and C. Bonnefoy, "Mechanical excitation of a membrane by an optical beam", *Proc. IEEE Ultrasonics Symp.*, New York, 1981, p. 802.

[133] S. Venkatesh and B Culshaw, "Optically excited vibrations in a micromachined silica structure", *Electron. Lett.*, vol. 21, pp. 315-317, 1985.

[134] H. Mizoguchi, M. Ando, T. Mizuno, T. Takagi and N. Nakajima, "Design and fabrication of light driven micropump", *Proc. IEEE Micro Electro Mech. Syst. Workshop*, Travemünde, Germany, February 1992, pp. 31-36.

[135] W. Riethmüller and W. Benecke, "Thermally excited silicon microactuators", *IEEE Trans. Electron Devices*, vol.35, pp.758-763, 1988.

[136] R. A. Buser, N. F. de Rooij, H. Tischhauser, A. Dommann and G. Staufert, "Biaxial scanning mirror activated by bimorph structures for medical applications, *Sensors and Actuators A*, vol. 31, pp. 29-34, 1992.

[137] L. M. Zhang, D. Walsh, D. Uttamchandani and B. Culshaw, "Effect of optical power on the resonance frequency of optically powered silicon microresonators", *Sensors and Actuators A*, vol. 29, pp. 73-78, 1991.

[138] H. T. G. van Lintel, F. C. M. van de Pol and S. Bouwstra, "A piezoelectric micropump based on micromachining of silicon", *Sensors and Actuators*, vol. 15, pp. 153-167, 1988.

[139] Tomio Ono, "Optical beam deflector using a piezoelectric bimorph actuator", *Sensors and Actuators*, A21-A23, pp. 726-728, 1990.

[140] S. Akamine, T. R. Albrecht, M. J. Zdeblick and C. F. Quate, "A planar process for microfabrication of a scanning tunneling microscope", *Sensors and Actuators*, A21-A23, pp. 964-970, 1990.

[141] W. Tjhen, T. Tamagawa, C. P. Ye, C. C. Hsueh, P. Shiller and D. L. Polla, "Properties of piezoelectric thin films for micromechanical devices and systems", *Proc. IEEE Micro Electro Mech. Syst. Workshop*, Nara, Japan, January/February 1991, pp. 114-119.

[142] A. M. Flynn, L. S. Tavrow, S. F. Bart, R. A. Brooks, D. J. Ehrlich, K. R. Udayakumar and L. E. Cross, "Piezoelectric micromotors for microrobots", *J. Microelectromech. Syst.*, vol. 1, pp. 44-51, March 1992.

[143] G.-A. Racine, R. Luthier and N. F. de Rooij, "Hybrid ultrasonic micromachined motors", *Proc. IEEE Micro Electro Mech. Syst. Workshop*, Ft. Lauderdale, FL, February 1993, pp. 128-132.

[144] R. T. Howe and R. S. Muller, "Resonant-microbridge vapor sensor", *IEEE Trans. Electron Devices*, vol. 33, pp. 499-506, 1986.

[145] Y.-C. Tai, L.-S. Fan, and R.S. Muller, "IC- processed micromotors: design, technology and testing", in *Proc. IEEE Micro Electro Mech.Syst. Workshop*, Salt Lake City, UT, February 1989, pp. 1-6.

[146] M. Mehregany, S. F. Bart, L. S. Tavrow, J. H. Lang, S. D. Senturia and M. F. Schlecht, "A study of three microfabricated variable-capacitance motors", *Sensors and Actuators*, A21-A23, pp. 173-179, 1990.

[147] A. P. Lee and A. P. Pisano, "Polysilicon angular microvibromotors", *J. Microelectromech. Syst.*, vol. 1, pp. 70-77, 1992.

[148] C. Linder, V. P. Jaecklin and N. F. de Rooij, "Modeling and Performance of Electromechanical Polysilicon Actuators", submitted for publication.

[149] V. P. Jaecklin, C. Linder, N. F. de Rooij, J. M. Moret, R. Bischof, and F. Rudolf, "Novel polysilicon comb-actuators for xy-stages", *Proc. IEEE Micro Electro Mech. Syst. Workshop*, Travemünde, Germany, February 1992, pp. 147-149.

[150] V. P. Jaecklin, C. Linder, N. F. de Rooij and J. M. Moret, "Micromechanical comb actuators with low driving voltage", *J. Micromech. Microeng.*, vol. 2, pp. 250-255, 1992.

[151] R. J. Roark and W. C. Young, *Formulas for stress and strain*, 5th ed., McGraw-Hill International Editions, Singapore, 1976, ch. 7.

[152] H. Guckel, D. W. Burns, H.A.C. Tilmans, D. W. DeRoo and C. R. Rutigliano, "Mechanical properties of fine grained polysilicon the repeatability issue, *Tech. Dig. IEEE Solid-Stote Sensor ond Actuotor Workshop*, Hilton Head Island, SC, June 1988, pp. 96 - 99.

[153] W. S. N. Trimmer and K. J. Gabriel, "Design considerations for a practical electrostatic micro-moter, *Sensors and Actuators*, vol. 11, pp. 189-206, 1987.

[154] R. L. Mullen, M. Mehregany, M. P. Omar and W. H. Ko, "Theoretical modeling of boundary conditions in microfabricated beams", *Proc. IEEE Micro Electro Mech. Syst. Workshop*, Nara, Japan, January/February 1991, pp. 154-159.

[155] K. E. Petersen, "Micromechanical membrane switches on silicon", *IBM J. Res. Develop.*, vol. 23, pp. 376-385, 1979.

[156] H. V. Allen, "Silicon-based micromechanical switches for industrial applications", in *IEEE Proc. Micro Robots Teleop. Workshop*, Hyannis, MA, November 1987.

[157] M. Sakata, "An electrostatic microactuator for electro-mechanical relay", *Proc. IEEE Micro Electro Mech. Syst. Workshop*, Salt Lake City, UT, February 1989, pp. 149-151.

[158] C. Linder, M.-A. Grétillat and N.F. de Rooij, "Realization of different polysilicon resonators with integrated excitation and detection elements", *Microelectronic Engineering*, vol. 15, pp. 411-414, 1991.

[159] R. Vuilleumier, A.-E. Perret, F. Porret and P. Weiss, "Novel electromechanical microshutter display device", *Proc. SID Eurodisploy '84*, Paris, France, 1984, pp. 41-44.

[160] V. P. Jaecklin, C. Linder, N. F. de Rooij, J.-M. Moret and R. Vuilleumier, "Optical microshutters and torsional micromirrors for light modulator arrays", *Proc. IEEE Micro Electro Mech. Syst. Workshop*, Ft. Lauderdale, FL, February 1993, pp. 124-127.

[161] W. Benecke and W. Riethmüller, "Applications of silicon-microactuators based on bimorph structures", *Proc. IEEE Micro Electro Mech. Syst. Workshop*, Salt Lake City, UT, February 1989, pp. 116-120.

[162] T. Gast, "Sensors with oscillating elements", *J. Phys. E: Sci. Instrum.*, vol. 18, pp. 783-789, 1985.

[163] R. T. Howe, "Resonant microsensors", *Tech. Dig. Int. Conf. Solid-State Sensors and Actuators* (Transducers '87), Tokyo, Japan, June 1987, pp.843-848.

[164] G. Stemme, "Resonant silicon sensors", *J. Micromech. Microeng.*, vol. 1, pp. 113-125, 1991.

[165] E. Stemme and G. Stemme, "A balanced resonant pressure sensor, *Sensors and Actuators*, A21-23, pp. 336-341, 1990.

[166] J. C. Greenwood, "Etched silicon vibrating sensor", *J. Phys. E: Sci Instrum.*, vol. 17, pp. 650-652, 1984.

[167] J. C. Greenwood and D. W. Satchell, "Miniature silicon resonant pressure sensor", *IEE Proceedings*, vol. 135, pp. 369-372, 1988.

[168] J. G. Smits, H. A. C. Tilmans and T. S. J. Lammerink, "Pressure dependence of resonant diaphragm pressure sensors", *Tech. Dig. Int. Conf. Solid-State Sensors and Actuators* (Transducers '85), Philadelphia, PA, June 1985, pp. 93-96.

[169] T. S. J. Lammerink and W. Wlodarski, "Integrated thermally excited resonant diaphragm pressure sensor", *Tech. Dig. Int. Conf. Solid-State Sensors and Actuators* (Transducers '85), Philadelphia, PA, June 1985, pp. 97-100.

[170] R. A. Buser and N. F. de Rooij, "Tuning forks in silicon", *Proc. IEEE Micro Electro Mech. Syst. Workshop*, Salt Lake City, UT, February 1989, pp. 94-95.

[171] S. Bouwstra, R. Legtenberg, H. A. C. Tilmans and M. Elwenspoek, "Resonating microbridge mass flow sensor", *Sensors and Actuators*, A21-23, pp. 332-335, 1990.

[172] J. J. Sniegowski, H. Guckel, T. R. Christenson, "Performance characteristics of second generation polysilicon resonating beam force transducers, *Tech. Dig. IEEE Solid-State Sensor and Actuator Workshop*, Hilton Head Island, SC, June 1990, pp. 9-12.

[173] C. J. van Mullem, F. R. Blom, J. H. J. Fluitman and M. Elwenspoek, "Piezoelectrically driven silicon beam force sensor", *Sensors and Actuators A*, vol. 25-27, pp. 379-383, 1991.

[174] H. A. C. Tilmans, S. Bouwstra, J. H. J. Fluitman and S. L. Spence, "Design considerations for micromechanical sensors using encapsulated built-in resonant strain gauges", *Sensors and Actuators A*, vol. 25-27, pp. 79-86, 1991.

[175] C. Linder, E. Zimmermann and N. F. de Rooij, "Capacitive polysilicon resonator with MOS detection circuit", *Sensors and Actuators A*, vol. 25-27, pp. 591-595, 1991.

[176] D. Moser, O. Brand and H. Baltes, "A CMOS compatible thermally excited silicon oxide beam resonator with aluminium mirror", *Tech. Dig. Int. Conf. Solid-State Sensors and Actuators* (Transducers '91), San Francisco, CA, June 1991, pp. 547-550.

[177] K. Petersen, F. Pourahmadi, J. Brown and P. Parsons, M. Skinner, J. Tudor, "Resonant beam pressure sensor fabricated with silicon fusion bonding", *Tech. Dig. Int. Conf. Solid-State Sensors and Actuators* (Transducers '91), San Francisco, CA, June 1991, pp.664-667.

[178] S. Timoshenko, D. H. Young and W. Weaver, *Vibration Problems in Engineering*, 4th ed., Wiley, New York, 1974, ch. 5.

[179] C. M. Harris and C. E. Crede, *Shock and Vibration Handbook*, 2nd ed., McGraw-Hill, New York, 1976.

[180] K. E. Petersen, A. Shartel and N. F. Raley, "Micromechanical accelerometer integrated with MOS detection circuitry, *IEEE Trons. Electron Devices*, ED-29, pp. 23-27, 1982.

[181] M.-A. Grétillat, "Réalisation de structures résonnantes - Méthodes d'excitation et de détection", Diploma Work, IMT, University of Neuchâtel, Spring 1991.

[182] C. J. van Mullem, H. A. C. Tilmans, A. J. Mounthaan and J. H. J. Fluitman, "Electrical cross-talk in two-port resonators - the resonant silicon beam force sensor", *Sensors and Actuators A*, vol. 31, pp. 168-173, 1992.

[183] W. Kalide, *Einführung in die technische Strömungslehre*, Carl Hanser Verlag, München, 1980.

Acknowledgements

The cooperation, knowledge and experience of a number of persons has been a great help to me during the work on my thesis. I want to express my sincere gratitude to all the persons who contributed to this work. Special thanks, I owe to:

Prof. N. F. de Rooij, for offering me the chance to write the thesis and for his continuous interest in this work;

Dr. R. Popovic, Dr. J.-L. Berchier and Dr. B. Hälg from Landis & Gyr Zug Corp., for the excellent collaboration in the first phase of this project;

Dr. J.-M. Moret and Dr. R. Vuilleumier from the Swiss Center for Electronics and Microtechnology (CSEM), for the successful cooperation in the FSRM project;

All my collegues of the "group de Rooij" of the Institute of Microtechnology, in particular:

M.-A. Grétillat, V. P. Jaecklin, S. Jeanneret, L. Paratte and E. Zimmermann, for the collaboration on polysilicon technology and applications;

P.-A. Clerc and Dr. T. Tschan, for the collaboration on plasma etching technology and applications; in addition, Dr. T. Tschan for his help in finite-element modeling;

J. Brugger for the cooperation in the fabrication of silicon cantilevers with integrated tips, and A. J. van der Wiel for the collaboration on bipolar-compatible thermal flow sensors;

Dr. D. J. Strike who corrected many parts of the manuscript with great devotion;

S. Pochon for valuable assistance in encapsulation and wire-bonding;

G. Mondin from Microsens SA for the deposition of metal films;

The technical staff of CSEM for the efficient cooperation,
in particular: C. Ketterer for the good-quality SEM micrographs.

Further I thank Dr. W. Trimmer, Prof. H. Baltes, and Prof. A. Shah for having kindly aggreed to be co-examiners.

Parts of this work were funded by Landis & Gyr Zug Corp., Switzerland; The Committee for the Promotion of Applied Scientific Research, Switzerland; The Swiss Foundation for Microtechnolgoy Research.

Biography

Christian Linder was born on May 18, 1960, in Vaduz, Liechtenstein. He received the diploma in physics from the Swiss Federal Institute of Technology, Zurich, Switzerland, in April 1986. His master's thesis dealt with metal-semiconductor field-effect transistors in gallium arsenide.
In August 1986, he joined the Institute of Microtechnology (IMT) at the University of Neuchâtel, Switzerland, where his first project was an evaluation study on silicon multisensors for industry, directed by Prof. N.F. de Rooij (IMT) and Dr. R. Popovic from Landis & Gyr Zug Corp.. In 1987, he was employed by Prof. A. Shah (IMT) on a 6-month project for the development of amorphous silicon field-effect transistors. Since then he has been working in the group of Prof. de Rooij as a research and teaching assistant. In the winter courses 91/92 and 92/93, he was co-lecturer on "Integrated Microsystems" at the Technical School NTB, Buchs (SG), Switzerland. His research interests include novel silicon micromachining techniques and IC compatible physical transducers for application in microsystems.

Publications

Refereed Articles

C. Linder and N.F. de Rooij, "Investigations on free-standing polysilicon beams in view of their application as transducers", *Sensors and Actuators*, A21-23, pp. 1053-1059, 1990.

C. Linder, E. Zimmermann and N. F. de Rooij, "Capacitive polysilicon resonator with MOS detection circuit", *Sensors and Actuators A*, vol. 25-27, pp. 591-595, 1991.

C. Linder, T. Tschan and N.F. de Rooij, "Deep dry etching of silicon – a novel micromachining tool", *Sensors and Materials*, vol. 3, pp.311-324, 1992.

A. J. van der Wiel, C. Linder, N. F. de Rooij and A. Bezinge, "A liquid velocity sensor based on the hot-wire principle", accepted for *Sensors and Actuators A*, 1992.

C. Linder, V. P. Jaccklin and N. F. de Rooij, "Modeling and Performance of Electromechanical Polysilicon Actuators", submitted for publication, 1993.

Review Article

C. Linder, L. Paratte, M.-A. Grétillat, V. P. Jaecklin and N. F. de Rooij, "Surface micromachining", *J. Micromech. Microeng.*, vol. 2, pp. 122-132, 1992.

Conference & Workshop Papers

C. Linder and N.F. de Rooij, "Investigations on free-standing polysilicon beams in view of their application as resonators", *Abstr. Dig. Transducers '89*, Montreux, Switzerland, 1989, COMST, Lausanne, pp. 289-290.

T. Tschan, C. Linder and N.F. de Rooij, "Dry etching techniques for silicon micromachining", *Tech. Dig. Micromechanics Europe 1990*, Berlin, Germany, 1990, pp. 253-260.

C. Linder, T. Tschan and N.F. de Rooij, "Deep dry etching techniques as a new IC-compatible tool for silicon micromachining, *Tech. Dig. Int. Conf. Solid-State Sensors and Actuators* (Transducers '91), San Francisco, CA, June 1991, pp. 524-527.

R. Buser, J. Brugger, C. Linder and N.F. de Rooij, "Micromachined silicon cantilevers and tips for bidirectional force microscopy", *Tech. Dig. Int. Conf. Solid-State Sensors and Actuators* (Transducers '91), San Francisco, CA, June 1991, pp. 249-252.

C. Linder, M.-A. Grétillat and N. F. de Rooij, "Realization of different polysilicon resonators with integrated excitation and detection elements", *Microelectronic Engineering*, vol. 15, pp. 411-414, 1991.

V. P. Jaecklin, C. Linder, N. F. de Rooij, J. M. Moret, R. Bischof, and F. Rudolf, "Novel polysilicon comb-actuators for xy-stages", *Proc. IEEE Micro Electro Mech. Syst. Workshop*, Travemünde, Germany, February 1992, pp. 147-149.

C. Linder, L. Paratte, M.-A. Grétillat, V.P. Jaecklin and N.F. de Rooij, Surface Micromachining, *Tech. Dig. Micromechanics Europe 1992*, Leuven, Belgium, 1992, pp.43-55.

V. P. Jaecklin, C. Linder, N. F. de Rooij and J. M. Moret, "Micromechanical comb actuators with low driving voltage", *J. Micromech. Microeng.*, vol. 2, pp. 250-255, 1992.

V. P. Jaecklin, C. Linder, J. Brugger, J.-M. Moret, R. Vuilleumier and N. F. de Rooij, "Mechanical and optical properties of surface micromachined torsional mirrors in silicon, polysilicon and aluminum", *Tech. Dig. Int. Conf. Solid-State Sensors and Actuators* (Transducers '93), Yokohama, Japan, June 1993.

M.-A. Grétillat, C. Linder and N. F. de Rooij, "Multilayer polysilicon resonators including shielding for excitation and detection", *Tech. Dig. Int. Conf. Solid-State Sensors and Actuators* (Transducers '93), Yokohama, Japan, June 1993.

V. P. Jaecklin, J. Brugger, C. Linder, P.-F. Indermühle and N. F. de Rooij, "Micromachined overhanging xy-actuator with protruding tip for scanned probe devices", accepted for oral presentation at *EUROSENSORS VII*, Budapest, Hungary, September 1993.

J. Brugger, V. P. Jaecklin, P.-F. Indermühle, C. Linder and N. F. de Rooij, "Fabrication of an overhanging xy-microactuator with integrated tip for scanned surface profiling", accepted as *Late News at Transducers '93*, Yokohama, Japan, June 1993.

Invited Seminar Presentations and Papers

C. Linder and N. F. de Rooij, "Fabrication of Free-standing Polysilicon Structures in View of their Application as Resonators", *AMA/SVS Seminar Mikromechanik*, Heidelberg, Germany, 1989, pp. 225-236.

C. Linder, "Polysilicon beams realized by surface micromachining and their applications as transducers", *Vortragsreihe: Integrierte Mikrosysteme und ihre Anwendungen*, Technical School NTB, Buchs (SG), Switzerland, December 1990.

C. Linder, "Deep plasma etching for silicon micromachining", *Formation Continue: Utilization of plasmas in modern fabrication techniques*, University of Neuchâtel, Switzerland, May 1992.

Research Reports

C. Linder and D. Kerschbaumer, "Evaluation von Sensoren für Klimaanlagen, insbeondere von Fluss-Sensoren (Evalution of sensors for air-conditioning systems, in particular, of flow sensors)", *Internal Report No 208 EC 01/87*, IMT, University of Neuchâtel, January 1987.

C. Linder and B. Leutz, "Vorstudie zur Entwicklung eines Dünnfilm-Transistors auf der Basis von amorphem Silizium (Study on a thin-film transistor based on amorphous silicon)", *Internal Report No 246 EC 06/88*, IMT, University of Neuchâtel, June 1988.

Patent

R. Buser, J. Brugger, C. Linder (Appls. & Invs.), British Technology Group Ltd. (Appl.), *Microprobe for Surface-Scanning Microscopes*, Patent, PCT/GB92/01060, 12 June 1992.